STRUCTURAL AND MECHANISTIC OBSERVATIONS OF THE FOSX CLASS OF FOSFOMYCIN RESISTANCE PROTEINS

By

Jessica Louise Grandillo

Thesis

Submitted to the Faculty of the

Graduate School of Vanderbilt University

in partial fulfillment of the requirements for

the degree of

MASTER OF SCIENCE

in

Biochemistry

December, 2006

Nashville, Tennessee

Approved:

Professor Richard N. Armstrong

Professor Daniel C. Liebler

ACKNOWLEDGEMENTS

This work would not have been possible without the generous financial support of the National Institute of Health and the Vanderbilt University Molecular Biophysics Training Grant. I would like to thank my mentor, Dr. Richard Armstrong, for his guidance throughout this project, as well as Dr. Laura Busenlehner and the rest of the Armstrong lab for teaching me how to be a good scientist. I am grateful to Dr. David Hachey, Lisa Manier, and Dawn Overstreet in the Mass Spectrometry Research Core for their technical expertise in several aspects of my project. I thank the members of my committee, Drs. Dan Liebler, Mike Waterman, and Al Beth, for their wisdom and suggestions. I also wish to thank Dr. James Patton and Dr. Roger Chalkley for their personal support over the years.

Dr. Moses Lee has been instrumental throughout my academic career, acting as a mentor and friend during my undergraduate years and beyond. I would like to thank Dr. David Wilson for the pleasure of working with him during my internship.

I especially wish to thank my parents for their unending support, advice, and faith in my decisions. Through them, I have discovered my strength.

TABLE OF CONTENTS

LIST OF TABLES

LIST OF FIGURES

LIST OF ABBREVIATIONS

DNA	Deoxyribonucleic acid
RNA	Ribonucleic acid
UDP-Glc*N*Ac	Uridine-5'-diphospho-*N*-acetyl-D-glucosamine
PEP	Phosphoenolpyruvate
MurA	Uridine-5'-diphospho-*N*-acetyl-D-glucosamine-3enolpyruvyltransferase
FDA	Food and Drug Administration
E. Coli	*Escherichia coli*
VOC	Vicinal Oxygen Chelate
MW	Molecular weight
HXMS	Hydrogen/deuterium exchange mass spectrometry
k_{ex}	Observed rate of exchange
k_o	Rate of structural opening
k_c	Rate of structural closing
k_i	Intrinsic rate of exchange
MS/MS	Tandem mass spectrometry
HPLC	High performance liquid chromatography
LB	Luria-Bertani media
MOPS	3-(N-morpholino)propanesulfonic acid
IPTG	Isopropyl-β-D-thiogalactopyranoside
MES	2-(N-morpholino)ethanesulfonic acid
DTT	Dithiothreitol
HEPES	N-(2-hydroxyethyl)piperazine N'-(2-ethanesulfonic acid)
TRIS	Tris(hydroxymethyl)aminomethane
EDTA	Ethylenediamine tetraacetic acid

CHES	2-(cyclohexylamino)ethanesulfonic acid
TMA	Tetramethylammonium
OD_{600}	Optical density at 600 nm
ESI	Electrospray ionization
PCR	Polymerase chain reaction
SDS-PAGE	Sodium dodecyl sulfate-polyacrylamide gel electrophoresis
MIC	Minimum inhibitory concentration
NMR	Nuclear magnetic resonance
GSH	Glutathione
TnC	Troponin C
TnI	Troponin I
EGTA	Ethylene glycol bis(β-aminoethyl ether)- *N*,*N*,*N'*,*N'*-tetraacetic acid
MALDI	Matrix-assisted laser desorption ionization
PF	Phosphonoformate
AcP	Acetylphosphonate
PA	Phosphonoacetate
2PP	2-Phosphonopropionate
ORF	Open reading frame
AEP	2-Aminoethylphosphonic acid
MPA	Methylphosphonic acid

CHAPTER I

INTRODUCTION

Antibiotics

The emergence of antibiotics as treatment for bacterial infections has been vital to continued human health. The term 'antibiotic' designates a chemical compound, either natural or synthetic, that disrupts the structure or function of a bacterium without simultaneously damaging its eukaryotic host (1). Antibiotic use of sulfonamides and penicillin began in the 1930's, dramatically decreasing the number of deaths that resulted from infectious diseases--previously the foremost cause of worldwide mortality and morbidity.

To date, 17 different antibiotic classes have been identified, the majority of which interfere with microbial biosynthesis of cell walls, proteins, DNA, or RNA. The cell walls of both Gram-positive and Gram-negative bacteria possess a peptidoglycan layer that withstands the microbes' strong intracellular pressure. Several classes of antibiotics target enzymes that form the peptidoglycan, rendering the bacterium vulnerable to osmolysis. Other antibiotics perturb protein synthesis, a common target due to the dissimilarity of ribosomal machinery between the bacterium and its multicellular host. A third antibiotic class interferes with DNA or RNA replication by targeting various proteins involved in transcription or the unwinding of supercoiled DNA. Still other antibiotics disrupt folic acid metabolism or cell membrane integrity (Table 1) (1,2).

Table 1. Antibiotic classes and their mechanisms of action. [Adapted from (2)].

Mechanism of action	Antibiotic families
Inhibition of cell wall synthesis	Beta-lactams (penicillins, cephalosporins, carbapenems, monobactams); glycopeptides; cyclic lipopeptides (daptomycin)
Inhibition of protein synthesis	Tetracyclines; aminoglycosides; oxazolidonones (linezolid); streptogramins (quinupristin-dalfopristin); ketolides; macrolides; lincosamides
Inhibition of DNA synthesis	Fluoroquinolones
Inhibition of RNA synthesis	Rifampin
Competitive inhibition of folic acid synthesis	Sulfonamides; trimethoprim
Membrane disorganizing agents	Polymixins (Polymixin-B, Colistin)
Other mechanisms	Metronidazole

Antibiotic Resistance

Unfortunately, despite the tremendous progress that has been made in the discovery and administration of antibiotics, microbes have developed resistance toward every drug on the market. The rampant drug resistance problem significantly contributes to infectious diseases being the second highest cause of death today (2). A consequence of the "survival of the fittest" rule of biology, microorganisms have acquired ways to adapt to drugs that were once lethal to them. Bacteria occasionally develop this resistance by spontaneous gene mutation but more commonly by transmission of a resistance gene from another bacterium. Resistance genes are usually transmitted through mobile genetic elements called transposons or more complex fragments called integrons, which contain multiple resistance genes and can thereby confer resistance to several antibiotics at once (1). Resistance can occur by three main mechanisms: A) development of a transport system that shuttles the antibiotic outside the cell or reduces influx, B) modification of the bacterial target so that the antibiotic can no longer bind to it, or C) evolution of enzymes that modify and inactivate the antibiotic (Figure 1) (1,2). This third mechanism is responsible for continued resistance to the once potent antibiotic fosfomycin.

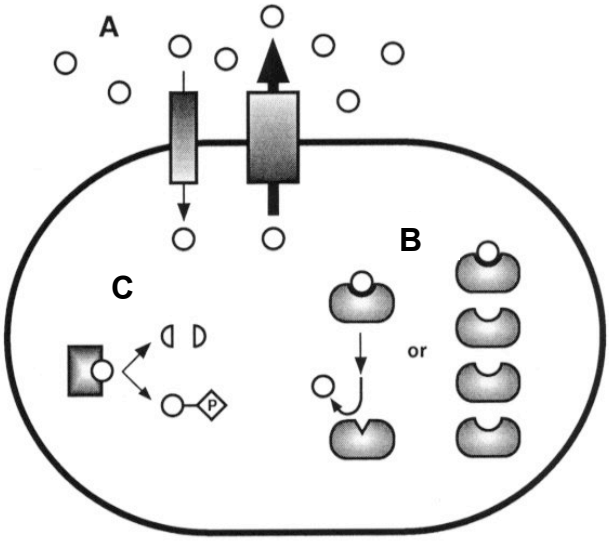

Figure 1. Three main routes to antibiotic resistance. A) increasing efflux or decreasing efflux, B) modification of antibiotic target, C) chemical inactivation of antibiotic. [Adapted from (1)].

Fosfomycin

Fosfomycin, (1*R*-2*S*)-epoxypropylphosphonic acid, was first isolated from *Streptomyces* cultures in 1969 as a broad-spectrum antibiotic against both Gram-positive and Gram-negative bacteria (Figure 2) (3,4). The compound was found to disrupt the first step of cell wall biosynthesis by inhibiting the reaction between UDP-Glc*N*Ac) and PEP, which is catalyzed by the enzyme UDP-*N*-acetylglucosamine enolpyruvyl transferase (MurA). In the uninhibited reaction, PEP attacks the 3'-OH of UDP-Glc*N*Ac to form enolpyruvyl UDP-Glc*N*Ac and organic phosphate (Figure 3a). Fosfomycin acts as a substrate analog of PEP and forms a covalent thioether bond to MurA's active site residue Cys115, thereby inactivating the enzyme (Figure 3b). Without proper functioning of MurA, cell wall biosynthesis halts and the cell dies (5-7). The exquisite specificity of fosfomycin for its enzyme target can be attributed to the phosphonate's position in MurA's anionic binding pocket, as well as the lack of fosfomycin homologues due to the unusual steric properties of oxirane rings (7).

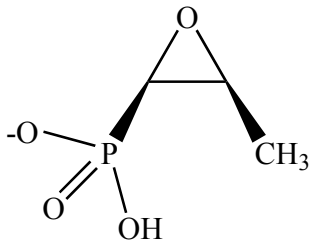

Figure 2. Structure of fosfomycin.

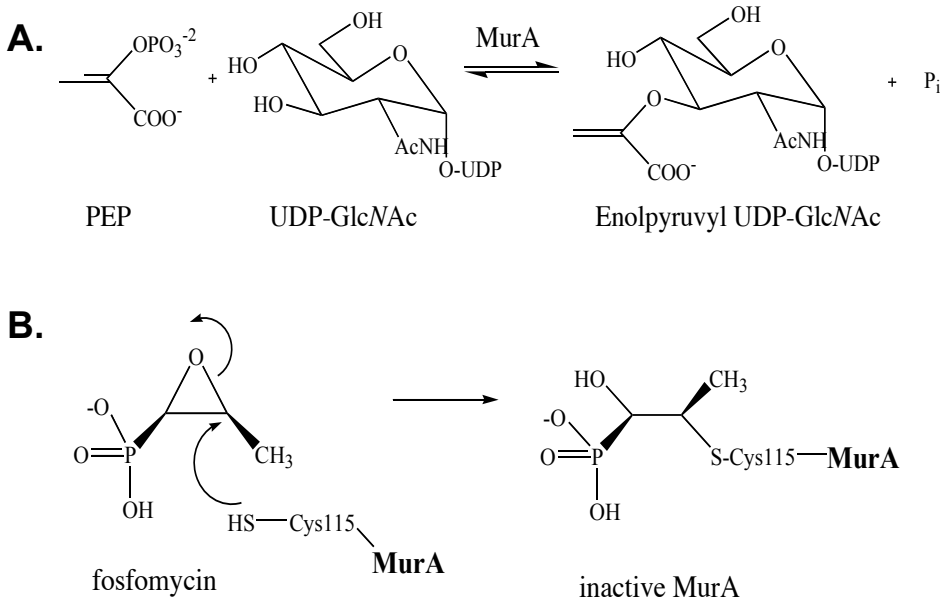

Figure 3. (a) First step of cell wall biosynthesis, catalyzed by MurA. (b) MurA reaction is inhibited by fosfomycin.

Fosfomycin is predominantly used to orally treat bacterial urinary tract infections in a single dose and is a clinically desirable compound because of its low toxicity and few side effects in humans. The FDA has even designated fosfomycin a safe drug to use during pregnancy (8, 9). Fosfomycin has been proven effective against bacterial infections resistant to other antibiotics as well; it has been used to combat vancomycin-resistant enterococci (10) and quinolone-resistant *E. coli* (11).

Fosfomycin Resistance and the Discovery of FosA

Soon after fosfomycin's introduction to the clinic, however, resistance to the drug was observed in several patients. Although early instances of resistance were due to chromosomal mutants that lost the ability to import fosfomycin (12, 13), eventually bacterial plasmids were found to encode resistance elements of an enzymatic nature (14, 15). Subsequent analysis of this first enzyme shown to inactivate fosfomycin revealed that the resistance was caused by adduct formation between fosfomycin and the sulfhydryl of glutathione, a reaction catalyzed by glutathione S-transferase (16, 17). This reaction opens the epoxide ring to render fosfomycin inactive against its target protein. The 16 kDa enzyme conferring resistance was named FosA and has since been designated a member of the Vicinal Oxygen Chelate (VOC) superfamily. Proteins in this group are characterized neither by the types of reactions they catalyze nor by transition state structure, but by the common presence of an electrophilic metal ion that participates in catalysis via two or more accessible coordination sites (18). Members of the VOC group are composed of paired βαβββ motifs arranged in different orientations to form the metal ion binding site (Table 2) (19). In the case of dimeric FosA, the metal sites adopt a domain-swapped arrangement to bind one metal ion per subunit (20). FosA's preferred metal is Mn^{2+}, but it will use other divalent metal cations with lower affinity (21). In addition, K^{+} is required for maximal activity of the enzyme and is presumed to aid in charge neutralization at the metal center to allow approach of a glutathione anion to the binding site (Figure 4) (22).

Table 2. Members of the VOC superfamily.

βαβββ motif

Member	Reaction Catalyzed
Fosfomycin Resistance Protein	Nucleophilic opening of epoxide
Bleomycin Resistance Protein	None (sequestration)
Extradiol Dioxygenase	Oxidative cleavage of C-C bond
Glyoxalase I	Isomerization
Methylmalonyl-CoA Epimerase	Epimerization

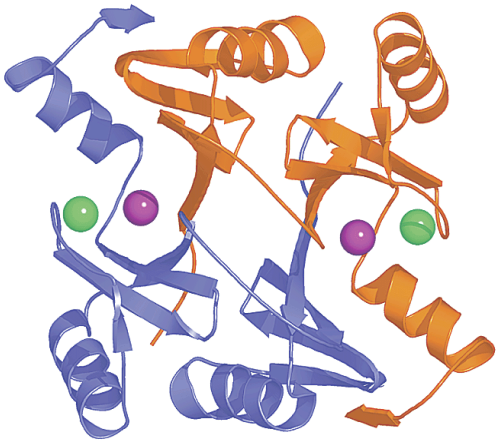

Figure 4. Crystal structure of *Pseudomonas aeruginosa* FosA with monomers depicted in orange and blue. Mn^{2+} and K^{+} ions are purple and green spheres, respectively. [Adapted from (49)].

Continued Emergence of Fosfomycin Resistance Proteins

Through sequence database searches, several FosA homologues have been identified, and the mechanistic differences among them have led to their separation into three distinct categories: FosA, FosB, and FosX. Although each of the classes confers resistance to fosfomycin, they do so with different substrates and metal ion dependencies (Figure 5). Unlike FosA, FosB enzymes use *L*-cysteine as the thiol donor rather than glutathione and prefer Mg^{2+} to Mn^{2+}. Their activities are unaltered by monovalent cations. The evolution of an enzyme using *L*-cysteine as an alternative thiol likely stems from the fact that organisms encoding FosB do not make glutathione. However, FosB shows only modest catalytic activity and resistance capability compared to the robust FosA (23).

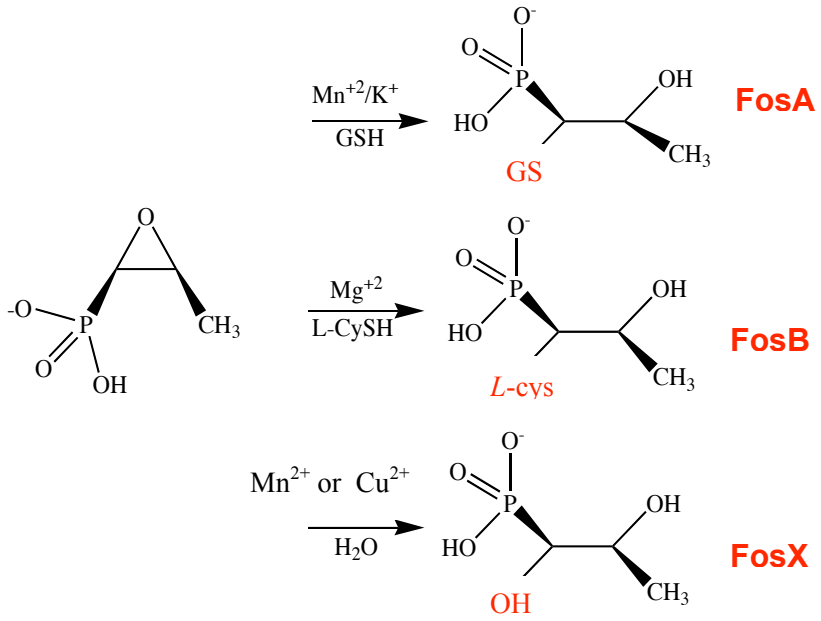

Figure 5. Reactions catalyzed by the three classes of fosfomycin resistance proteins.

The FosX enzymes differ from the previous two classes in that they act as epoxide hydrolases, catalyzing the addition of water to fosfomycin to yield the diol product 1,2-dihydroxypropylphosphonic acid. FosX structures have proven complementary to FosA in several regions including the active site. An overlay of the FosA and FosX active sites reveals some similarities in metal binding and substrate recognition sites, but an important difference is residue E44 in FosX (corresponding to G37 in FosA), which acts as a general base for the conjugation of water to fosfomycin (Figure 6). FosX activity does not require a monovalent cation, and residues corresponding to the FosA K^+ binding loop show no electron density in FosX crystal structures (24). While most FosX enzymes use Mn^{+2} as their preferred metal, recent data reveals that some enzymes exhibit optimum catalytic activity with Cu^{+2} instead (unpublished observations). Kinetic and biological properties of several characterized fosfomycin resistance proteins are displayed in Table 3.

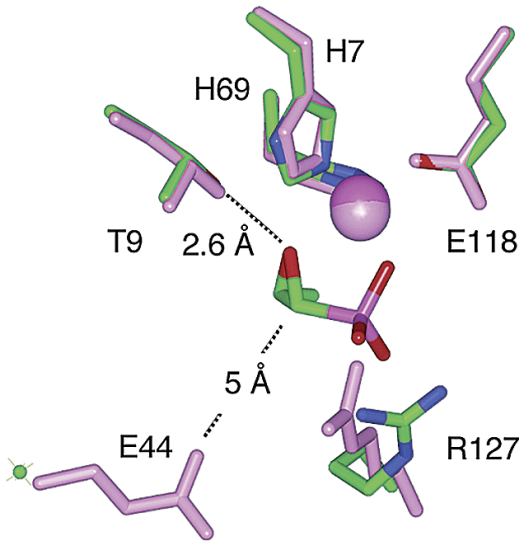

Figure 6. Overlay of FosA active site (green) and FosX active site (pink). Residues are numbered according to FosX sequence. Equivalent positions in FosA, listed clockwise from lower left, are G37 (green dot), T9, H64, H7, E110, and R118. [Adapted from (24)].

Table 3. Catalytic and resistance properties of several fosfomycin resistance proteins. TN=transposon, PA=*Pseudomonas aeruginosa*, BS=*Bacillus subtilis*, SA=*Staphylococcus aureus*, ML=*Mesorhizobium loti*, LM=*Listeria monocytogenes.* [Adapted from (32)].

Protein	k_{cat} (s^{-1})	k_{cat}/K_M^{fos} (M^{-1} s^{-1})	MIC mg/mL	MW
$FosA^{TN}$	660 ± 10	(1.4 ± 0.1) x 10^7	>20	15889
$FosA^{PA}$	175 ± 6	(9.0 ± 1.4) x 10^5	>20	15114
$FosB^{BS}$	4.8 ± 0.3	(4.0 ± 0.5) x 10^3	0.1	17173
$FosB^{SA}$	0.99 ± 0.02	(9.2 ± 0.1) x 10^3	0.4	16637
$FosX^{ML}$	0.15 ± 0.02	(5.0 ± 0.6) x 10^2	0.025	16181
$FosX^{LM}$	34 ± 2	(9 ± 2) x 10^4	>20	15655
None			<0.025	

The data presented herein concern the FosX enzymes encoded in two microorganisms, *Listeria monocytogenes* and *Pseudomonas putida.* A brief discussion of these species is necessary to understand the relevance of this project.

Listeria monocytogenes

Listeria monocytogenes is a Gram-positive, food-borne pathogen that can grow at temperatures as low as 3°C, which allows it to survive in refrigerated foods and makes it virtually undetectable. It is normally soil-dwelling but has also been isolated from wild and domesticated animals, insects, soil, water, and vegetation. As is the case for many bacterial species, people at highest risk for acquiring a *Listeria* infection are immunocompromised patients and pregnant women, for whom the fetal mortality rate is 80%. Following gastrointestinal symptoms, more serious disorders including meningitis and encephalitis often develop. However, since early symptoms resemble the flu, they are frequently ignored until the bacteria have multiplied and spread throughout the nervous system to cause irrevocable damage. *Listeria* infection is quite dangerous; in the year 2000, 95% of people infected with the bacteria required hospitalization (Figure 7), and over 20% of cases resulted in death (Figure 8). These numbers are in stark contrast to more commonly mentioned food-borne pathogens such as *E. coli* and *Salmonella* (25).

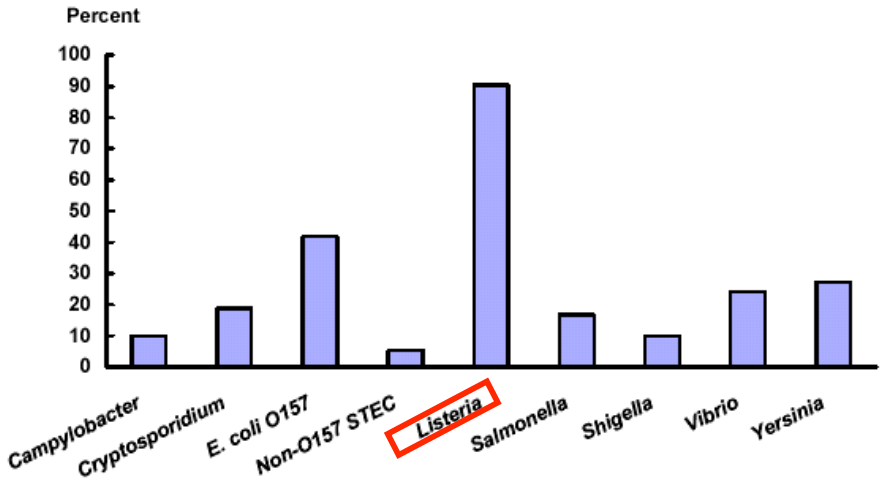

Figure 7. Percentage of hospitalizations from food-borne infections in 2000. [Adapted from (25)].

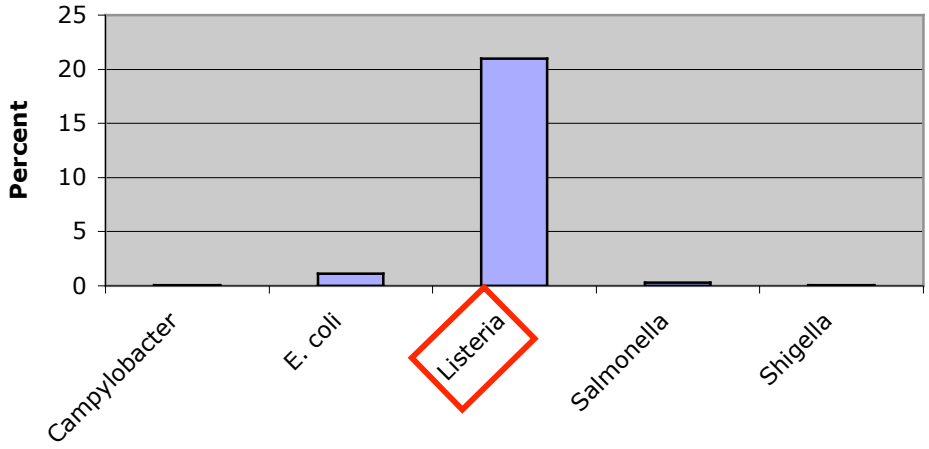

Figure 8. Percentage of fatalities from food-borne infections in 2000. [Adapted from (25)].

Pseudomonas putida

Pseudomonas putida is a saprophytic Gram-negative microorganism that has typically been considered non-pathogenic. It is soil-dwelling and has rarely been isolated from clinical specimens, so little is known about its capacity to cause human infection. Resistance to *P. putida* is poorly understood, since it is usually susceptible to standard antimicrobial agents. However, many experts believe that it has the capacity to become as resistant as its dangerous relative *Pseudomonas aeruginosa,* with which it shares 85% of its gene coding regions. *P. putida* shows a remarkable ability to decompose many carbon sources that other organisms cannot; therefore, it is not surprising that the bacterium could develop resistance to the fosfomycin molecule. The putative resistance protein studied in this work is located on an integron, making it even more dangerous because the genetic element also contains resistance enzymes β-lactamase and aminoglycoside acetyltransferase (Figure 9). The *Pseudomonas putida* FosX on this integron shares over 50% identity to established FosX enzymes (Figure 10) (26-28).

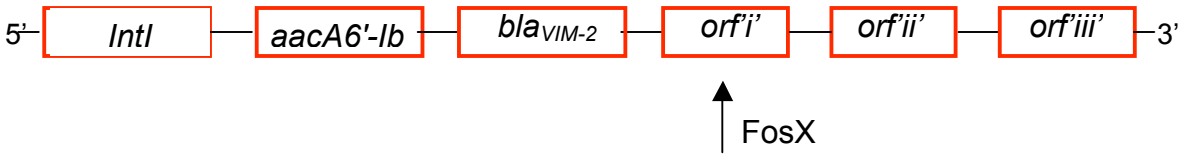

Figure 9. Structure of antibiotic resistance integron isolated from *Pseudomonas putida.* Modeled after GenBank accession number AY065966.

```
>gi|46395924|sp|Q8Y6I2|FOSX_LISMO  Fosfomycin resistance protein fosX
          Length=133

 Score =  162 bits (411),  Expect = 2e-40
 Identities = 74/130 (56%), Positives = 97/130 (74%), Gaps = 0/130 (0%)

Query  10   MEGISHITLIVRDLSRMTTFLCDGLGAREVYDSAGHNYSLSREKFFVLGGVWLAAMEGVP  69
            + G+SHITLIV+DL++ TTFL +   A E+Y S    +SLS+EKFF++ G+W+  MEG
Sbjct  2    ISGLSHITLIVKDLNKTTTFLREIFNAEEIYSSGDQTFSLSKEKFFLIAGLWICIMEGDS  61

Query  70   PSERSYQHVAFRVSESDLAVYQARLGSLGVEIRPPRPRVNGEGLSLYFYDFDNHLFELHT  129
              E++Y H+AFR+   ++  Y  R+ SLGVEI+P RPRV GEG S+YFYDFDNHLFELH
Sbjct  62   LQEQTYNHIAFRIQSEEVDEYIERIKSLGVEIKPERPRVEGEGRSIYFYDFDNHLFELHA  121

Query  130  GTLEQRLARY  139
            GTLE+RL RY
Sbjct  122  GTLEERLKRY  131
```

Figure 10. Sequence homology of *Pseudomonas putida* FosX ("Query") and *Listeria monocytogenes* FosX ("Sbjct"). Residues in red are metal-binders, green are catalytic bases, and blue are fosfomycin recognition sites.

Purpose

Antibiotic resistance is a dangerous consequence of a bacterium's ability to adapt to harmful environments. Drugs that once easily eradicated common illnesses have in many cases been rendered useless by the mounting resistance problem. To resolve this global healthcare issue, we must strive to learn all we can about the molecular bases of drug resistance so that we may devise new treatments for infectious diseases. This work discusses the FosX fosfomycin resistance proteins found in *Listeria monocytogenes* and *Pseudomonas putida*, as a thorough understanding of the chemical and biological properties of these enzymes is essential to restoring the power of fosfomycin as a robust antimicrobial agent. Knowledge of these proteins may one day lead to development of small molecule inhibitors that will lessen or eliminate bacterial resistance to this antibiotic.

CHAPTER II

HYDROGEN/DEUTERIUM EXCHANGE MASS SPECTROMETRY CONCEPTS AND ANALYSIS

Theory

Hydrogen/deuterium exchange mass spectrometry (HXMS) is a powerful technique that uses solvent accessibility of amide hydrogen atoms along a protein backbone to predict the solution structure of the protein. Linderstrøm-Lang first conceptualized the idea that the rate of amide hydrogen exchange with solvent molecules is a reflection of the protein's rigidity. Hydrogen atoms on a polypeptide such as the one shown in Figure 11 will exchange with solvent hydrogen (or deuterium) at different rates. The hydrogens colored green in the figure are covalently bonded to carbon atoms and hence do not undergo exchange. The blue ones, making up the side chains, exchange at rates too rapid to be detected by conventional methods. Finally, the red hydrogens, which compose the backbone amides of all amino acids except proline, exchange at measurable rates depending on such factors as protein structure and solution pH (29).

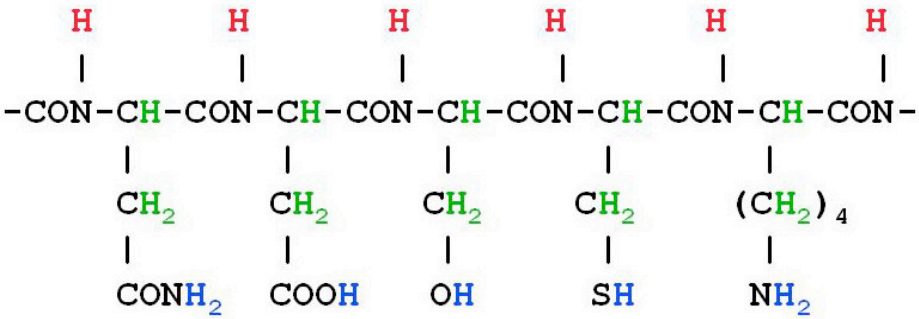

Figure 11. Three types of hydrogen atoms within a protein. [Adapted from (29)].

At neutral pH and with D_2O as solvent, OD^- will abstract these protons in a base-catalyzed reaction. The speed and efficiency of base catalysis is a function of each amide hydrogen's placement in the folded protein and can be described as lying on a continuum between immediate exchange and exchange that occurs only after complete unfolding of the protein. The fastest exchange is called "EX2" and results when refolding of the protein happens more quickly than the intrinsic rate of hydrogen exchange for deuterium. The rate expression for this process shows that the observed rate depends on the equilibrium constant between folded and unfolded protein states. On the other end of the continuum is

the “EX1” regime, whereby exchange occurs more quickly than opening of the protein and exposure of the amide hydrogen to solvent. Thus the observed rate for EX1 is defined as the rate of protein unfolding (Figure 12). In short, if the proton is engaged in hydrogen bonding or is part of tight secondary structure, the dynamic fluctuations that must occur for the proton to become solvent accessible will result in slower exchange rates. If the proton is in a more accessible region, then OD^- can approach more easily and faster exchange will occur. These rates can be monitored using mass spectrometry and reflect conformational changes that accompany ligand binding and enzyme catalysis (30, 31).

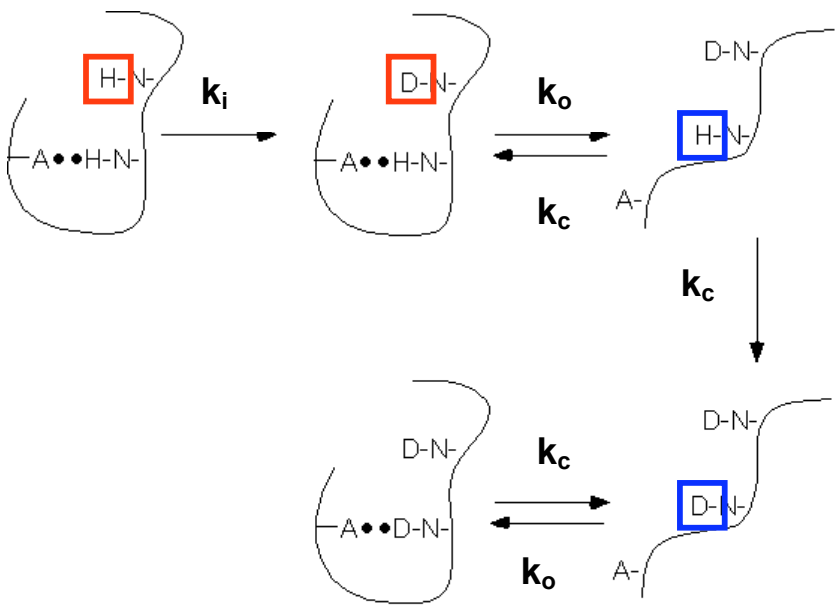

$k_{ex}=k_o/k_i\ (k_o + k_c + k_i)$

EX2: $k_c >> k_i$; $k_{ex} = (k_o/k_c)/k_i$

EX1: $k_i >> k_c$; $k_{ex} = k_o$

Figure 12. Schematic of hydrogen/deuterium exchange in a folded protein with representative rate expressions. [Adapted from (31)].

Experimentation

To determine the proton-deuterium exchange rates for the backbone protons, the protein must be proteolytically cleaved at as many residues as possible to attain the greatest spatial resolution. The ideal situation would be to cleave enough overlapping peptides to enable calculation of every amide hydrogen exchange rate. While this has not yet been

accomplished, the resolution can be significantly improved by using multiple proteases. This creates what is called a peptide map and is generated by incubating the protein with each acid protease that will be used in the HXMS experiments and sequencing the fragments using tandem MS/MS. The fragments are then used as reference points from which to calculate the mass increase upon hydrogen exchange with solvent deuterium.

Amide hydrogen exchange is temperature- and pH-dependent, as shown in Figure 13. To take advantage of this property, the protein is initially incubated with solvent D_2O for a range of time points at room temperature and neutral pH, where exchange occurs rapidly. Then to effectively "trap" deuterium onto the protein to prevent back-exchange to hydrogen, chilled acidic quench solution is added followed by an acid protease that cleaves along the backbone. The entire sample is then placed on ice for several minutes to further prevent back-exchange. At this point, protein cleavage is complete, and the solution is injected onto a reverse-phase HPLC column, and peptides are separated with a mobile phase gradient. Because electrospray ionization is used, the output of the HPLC becomes the input of the MS as fine droplets of the sample are sent to the mass analyzer (Figure 14) (30, 31).

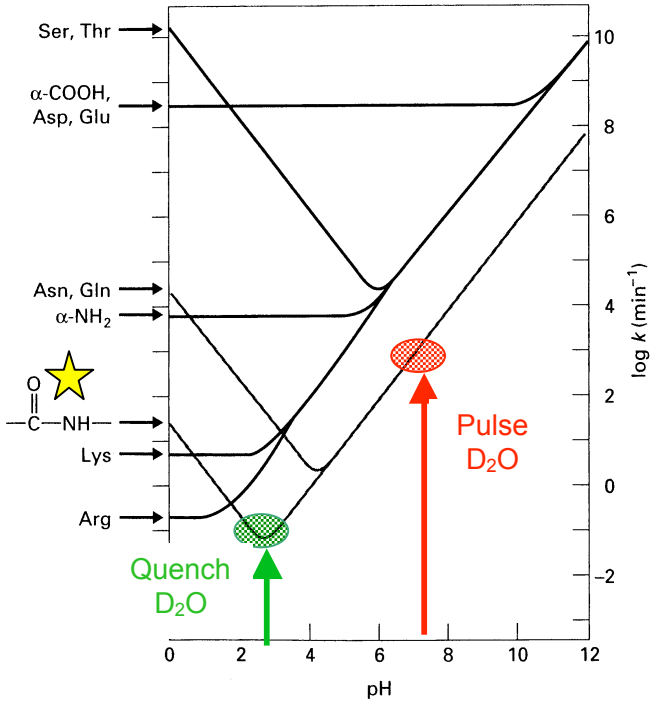

Figure 13. pH dependence of hydrogen exchange rates.

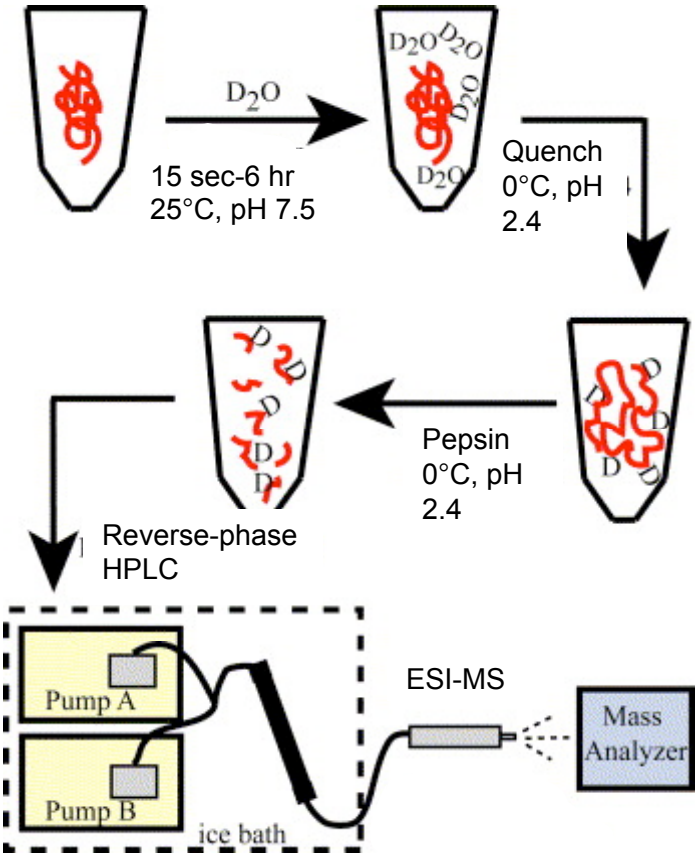

Figure 14. Schematic of HXMS experiment. [Adapted from (31)].

Analysis

To analyze deuterium incorporation into the protein, each of the peptides detected from the map is again detected in the deuterated spectra, but the masses will be shifted to a value dependent upon the extent of exchange for deuterium, a heavier isotope. The masses will appear as roughly symmetrical peaks separated by one mass unit for each deuterium that has been added. These values must be corrected for the amount of exchange occurring during the digest itself, which is called the 0% control for the reaction. All values are also placed in the context of the maximum possible exchange, the 100% control, which is determined by incubating the protein for a longer time (ideal time is determined experimentally) and at a high temperature to facilitate unfolding. Masses at each time point must be averaged using the same size mass envelope to ensure that values are normalized (30, 31). Further details of the analysis are included in the Methods section of this work.

CHAPTER III

MATERIALS AND METHODS

Materials

E. coli Rosetta (DE3) cells and XL1-Blue cells were from Novagen (San Diego, CA). BL-21 (DE3) cells were from Stratagene (La Jolla, CA). LB media, ampicillin, MOPS, IPTG, MES, and DTT were from RPI (Mt. Prospects, IL). Chloramphenicol, kanamycin, lactose, pepsin, *Aspergillus saitoi* protease XIII, *Rhizopus* protease XVIII, potassium phosphate, formic acid, HEPES, agarose, TRIS, EDTA, lysozyme, P2714 protease inhibitor, streptomycin sulfate, CHES, glutathione, and *L*-cysteine were from Sigma (St. Louis, MO). Acetonitrile, NaCl, and KCl were from Fisher (Hampton, NH). All metals (puratronic grade) in their chloride salt form were from Alfa Aesar (Ward Hill, MA). D_2O and TMA were from Acros (Geel, Belgium). Wizard DNA Purification System was from Promega (Madison, WI). Restriction enzymes *NdeI* and *XhoI* and ligation kit were from New England Biolabs (Ipswich, MA). Chelex 100 resin was from Bio-Rad (Hercules, CA). Fosfomycin was from Fluka (Ronkonkoma, NY). SP Sepharose Fast Flow resin was from Amersham Biosciences (Uppsala, Sweden).

Methods

Expression of Listeria monocytogenes *FosX*

The expression plasmid for gene *lmo*1702 was constructed and transformed into *E. coli* Rosetta (DE3) cells as previously described (32). Two 1.3 L cultures were inoculated with bacteria from an overnight starter culture (incubated approx. 13 hrs at 28.5°C and shaken at 160 RPM) to reach a starting OD_{600} of 0.025. Starter and inoculated cultures contained LB media, 80 μg/mL ampicillin, and 18 μg/mL chloramphenicol. Inoculated cultures were incubated at 30°C and shaken at 225 RPM until reaching an OD_{600} of 0.6. Protein overexpression was induced with 1 mg/mL lactose for 5-6 hrs. Cells were harvested by centrifugation and stored at -80°C.

Purification of L. monocytogenes *FosX*

Purification was carried out as previously described (32).

Identification of L. monocytogenes *FosX Peptic Fragments*

Pepsin digests using a 1:1.5 FosX:pepsin w/w ratio were performed under the quenching conditions of the HXMS experiment. 71 μg of FosX (5 μL) in 20-25 μL quench buffer (0.1 M potassium phosphate, pH 2.4) was digested by adding 106.5 μg of pepsin (3.6 μL of 30 mg/mL solution in H_2O) for 5 mins on ice (0°C). The pepsin-digested peptides were separated by reverse-phase HPLC using a ThermoFinnigan Surveyor HPLC (San Jose, CA) and identified by tandem ESI-MS/MS sequencing as peptides are eluted. Peptides were first separated on a Jupiter 50 x 1.00 mm C18 column (Phenomenex, Torrance, CA) using a mobile phase gradient of buffer A (98% H_2O, 2% acetonitrile, 0.4% formic acid) and buffer B (98% acetonitrile, 2% H_2O, 0.4% formic acid) over 25 mins (0.1 mL/min). A six-port divert valve was used to send early-eluting contaminant species to waste. Peptides were sequenced using a ThermoFinnigan TSQ triple quadrupole mass spectrometer (San Jose, CA) in positive-ion mode by data-dependent tandem MS/MS collision-induced dissociation (33, 34). Capillary temperature=190°C, scan time=4 s, peak width=0.2, collision energy=25 and 40, scanned 300-1500 *m*/*z*. Data processing was performed using Finnigan Xcalibur software (version 1.3). The identities of the peptides were determined using ExPASy-PeptideMass software (35) and were confirmed by analysis of the MS/MS sequencing of individual peptides by comparison to theoretical fragmentation patterns generated by the ProteinProspector program MS-Product (36).

Digests using *Aspergillus saitoi* protease XIII were performed using a 10:1 FosX: protease XIII w/w ratio. Digests using *Rhizopus* protease XVIII were performed using a 16:1 FosX: protease XVIII w/w ratio (37). Both cleavages were done under the same quench and digestion conditions, solvents, and instruments as described for pepsin above. As these are rare proteases whose cleavage patterns are unknown, the alternate Macintosh-based program Sherpa version 3.3.1 (Alex Taylor, University of Washington), which calculates all possible cleavage species, was used to analyze MS/MS sequencing of individual peptides generated by these enzymes. FosX maps obtained from each protease are shown in Appendix A.

HXMS Protocol

FosX protein used in HXMS was dissolved in 20 mM MOPS buffer, pH 7.5. For apoprotein or protein bound to Mn^{2+}, Co^{2+}, or Zn^{2+}, deuterium exchange was initiated by adding 45 D_2O to 5 μL of 400 μM protein solution. Metal stocks were prepared at approx. 10 mM in degassed H_2O at pH 7.0, and 1:1 eq. metal:FosX was incubated for at least 10

minutes preceding the addition of D_2O to ensure binding saturation. The protein/D_2O solution was incubated at 25°C for various times between 15 s and 6 hrs. At each time point, the reaction was quenched by placing the tube on ice and adding 50 µL of quench buffer listed above. After 30 s, 1.5 eq. pepsin:FosX w/w (30 mg/mL in H2O) was added to the quenched sample and incubated on ice for 5 min. All of the samples for each day of HXMS were prepared and run individually (33, 34).

0% and 100% Control Experiments

To determine the amount of deuterium incorporated during the digest step so that it can later be subtracted from the exchange at each time point ($m_{0\%}$), 50 µL quench buffer was added to 5 µL of 400 µM protein solution, immediately followed by 45 µL D_2O. After 30 s incubation, 1.5 eq. pepsin:FosX was added and the sample digested on ice for 5 mins.

The fully deuterated sample is also used a control in the mathematical analysis of partial deuteration. This sample ($m_{100\%}$) is obtained by incubating FosX and D_2O for an extended period of time (8 hrs here) at a high temperature (50°C here) to allow the protein to unfold. Acidic quench buffer and pepsin are then added as for the partially deuterated samples (33, 34).

HPLC/ESI-MS

The HPLC injection loop and gradient solvents were kept submerged in ice (0° C) for the entirety of the experiment to minimize deuterium-hydrogen back-exchange. The peptides were separated over 12 mins with a 2-60% gradient of buffers A and B. Peptides were separated and mass-analyzed as described above. The mass spectrometer was operated in full scan mode using Quad 1. Capillary temperature=190°C, scan time=1 s, peak width=0.7, collision energy=15, scanned 300-1500 *m*/*z*. MagTran 1.0 beta 9 software was used to determine the centroid of the mass envelope (38).

Kinetic Analysis

The amount of deuterium incorporated into each peptide as a function of time is adjusted for the gain ($m_{0\%}$) and loss ($m_{100\%}$) of deuterium during analysis. The corrected deuteration is defined by the following expression:

$$D = \left[N \left(\frac{m_t - m_{0\%}}{m_{100\%} - m_{0\%}} \right) \right]$$

where $m_{0\%}$ represents the nondeuterated average mass of a peptide, m_t is the partially deuterated average mass at time t, and $m_{100\%}$ is the fully deuterated average mass. N is the total number of exchangeable amide protons minus one for each N-terminal residue and any prolines contained on the peptide. Native protein results were the average of three data sets, Mn^{2+}-bound protein the average of five, and Co^{2+}- and Zn^{2+}-bound protein the average of two each. Deuterium incorporation was plotted versus time according to the following equation using the program Prism version 4.0a (Graphpad Software), where D is the number of incorporated deuterons, N is the total number of exchangeable amide protons, A_n is the number of deuterons incorporated for the rate constant described by $k_n t$, and t is the incubation time. For FosX, all traces were fit to either single- or double-exponential equations (33, 34).

$$D = N - A_1 e^{-k_1 t} - A_2 e^{-k_2 t} - A_3 e^{-k_3 t} \ldots - A_n e^{-k_n t}$$

Absorbance Spectroscopy

To probe binding properties of FosX for divalent metal ion cofactors, proteins are titrated with increasing amounts of metal in order to observe changes in intrinsic protein absorbance. Binding experiments using 100-200 μM protein were carried out in 20 mM TMA-MOPS, pH 7.5, 25°C. Optical spectra of native protein and protein plus each aliquot of metal titrant (5 μL increments) were collected on a Perkin-Elmer *lambda* 45 double-beam spectrophotometer (Wellesley, MA) with 2 min protein-metal equilibrations prior to the absorbance scan of 240-700 nm. Precise concentration of protein in the cuvette was determined from ε_{280} = 1.34 x 10^4 M^{-1} cm^{-1}. Spectra were corrected for background by establishing baseline at A_{650}, subtracting starting apoprotein spectrum, and correcting for dilution. Binding saturation was monitored by calculating the absorbance difference between 470 nm and 424 nm. Corrected absorbance was plotted against concentration to determine the number of equivalents needed to saturate FosX binding sites (39, 40). Plots were generated with Microsoft Excel X.

Fluorescence Spectroscopy

In a preliminary experiment, optimal excitation wavelength was determined to be 290 nm, and peak emission wavelength was determined to be 340 nm. Fluorescence experiments using 5 μM protein were carried out in 25 mM TMA-HEPES, 150 mM NaCl, pH 7.5 passed through a 0.2 μm syringe filter. Two-mL cuvettes that had been soaked in 10%

HNO_3 for >24 hours to eliminate contaminating metal species were thoroughly rinsed before beginning the titrations. Spectra of native protein and protein plus each aliquot of metal titrant (8 μL increments) were collected on a Horiba Fluorolog, allowing 10 min protein-metal equilibrations prior to each fluorescence scan. Precise protein concentration at the onset of the experiment was determined from $\varepsilon_{280} = 1.34 \times 10^4\ M^{-1}\ cm^{-1}$ on a Perkin-Elmer *lambda* 45 double-beam spectrophotometer. Spectra were corrected for background and intrinsic protein fluorescence, and corrected fluorescence was plotted against concentration to determine the number of equivalents needed to saturate FosX binding sites. Plots were generated with Microsoft Excel X.

Cloning of Pseudomonas putida *FosX*

The gene containing the putative FosX enzyme from *Pseudomonas putida* with codon optimization for expression in *E. coli* was ordered from the company DNA 2.0 (Menlo Park, CA). It was received in two forms: encoded in lyophilized plasmid pJ5:G02754 (trademarked by DNA 2.0 and containing kanamycin resistance cassette and desired restriction sites for insertion into plasmid of choice), and transformed into an *E. coli* stab culture for culture growth and DNA harvesting. *E. coli* stab culture was streaked and plated onto LB plates containing 30 μg/mL kanamycin. After overnight growth at 37°C, an individual colony was selected for small culture growth at 37°C and 225 RPM. Plasmid DNA was then extracted using Promega Wizard Miniprep kit. The pJ5 plasmid and pET20b(+) plasmid were digested simultaneously with 5' restriction enzyme *NdeI* and 3' restriction enzyme *xhoI*, and incubated for 4 hrs at 37°C. Digestion products were run on an agarose gel and the proper molecular weight bands were excised and purified using Amicon Ultrafree-DA spin columns. FosX gene insert and linear pET20b(+) plasmid were ligated using New England Biolabs ligation kit and transformed into XL-1 Blue cells. Transformed cells were plated onto LB plates containing 100 μg/mL ampicillin and placed in an incubator at 37°C overnight. DNA was harvested using Wizard kit. Presence of FosX gene insert was verified using PCR, and sequence was confirmed by submission to Vanderbilt Sequencing Core.

Expression of P. putida *FosX*

pET20b(+) expression vector containing FosX gene was transformed into *E. coli* BL-21 (DE3) cells for optimum protein expression. One 1 L culture was inoculated with bacteria

from an overnight starter culture (incubated approx. 14 hrs at 28.5°C and shaken at 165 RPM) to reach a starting OD_{600} of 0.025. Starter and inoculated cultures contained LB media and 100 μg/mL ampicillin. Inoculated cultures were incubated at 30°C and shaken at 180 RPM until reaching an OD_{600} of 0.6. Protein overexpression was induced with 0.4 mM IPTG for 5 hrs. Cells were harvested by centrifugation and stored at -80°C.

Purification of P. putida *FosX*

Cell pellets were thawed on ice and resuspended in 10-15 mL 25 mM TRIS buffer, 75 mM NaCl, 0.5 mM EDTA, pH 7.5 (buffer C). To aid cell lysis, ~2 mg lysozyme was added and cells incubated at 25°C for 1 hr with gentle rocking, and then incubated on ice (0°C) for an additional hr. Another 21 mL lysis buffer was added to cell suspension and mixture was further lysed using a Bronson sonicator (70% duty cycle, 6-7 output control) in 4 x 3 min cycles with a 3 min pause between each. Sigma P2714 protease inhibitor was added after first cycle. Cell debris was removed by centrifugation at 35,000 x *g* for 25 mins. The supernatant was treated with 500 mg streptomycin sulfate dissolved in 1 mL H_2O and stirred for 1.5 hrs at 4°C to remove nucleic acids. Centrifugation was repeated, and crude lysate was dialyzed (all dialysis performed overnight in 4°C unless otherwise noted) in 2 L 25 mM MES buffer, 150 mM NaCl, 0.5 mM EDTA, pH 6.0 (buffer D). In the morning, centrifugation was again repeated to ensure removal of all nucleic acids and precipitated proteins. Lysate was passed through an SP Sepharose Fast Flow column equilibrated with buffer D. Column was washed with buffer D and protein was eluted using a linear NaCl gradient (150-500 mM). Fractions containing putative FosX were identified by absorbance at 280 nm (ε_{280} = 1.465 x 10^4 M^{-1} cm^{-1}) and SDS-PAGE analysis. Fractions containing the protein were pooled and dialyzed against 2 L demetalation buffer E (20 mM MOPS, 10 mM NaCl, 5 mM EDTA, 0.5 mM DTT, 3 g Chelex resin, pH 7.5) for 2 days. Protein was then dialyzed in 2 L second dematalation buffer F (20 mM TMA-MOPS, 0.5 mM DTT, 2 g Chelex, pH 7.5), followed by another dialysis into 2 L more of buffer F. Protein was concentrated in a nitrogen pressure cell using a 5K molecular weight cutoff membrane and stored at -80°C. Identity was confirmed through MALDI mass spectrometry on an Applied Biosystems Voyager instrument (Foster City, CA). Final yield was 25 mg per L of culture.

Determination of Minimum Inhibitory Concentration of Fosfomycin

In agar. Growth of *E. coli* BL21 (DE3) cells containing the *Pseudomonas putida* FosX expression plasmid was compared to growth of cells containing *Listeria monocytogenes*

FosX expression plasmid, whose fosfomycin MIC value has been established, and empty vector control. Bacteria that had reached OD_{600} = 0.015 were streaked onto LB plates containing 100 μg/mL ampicillin, 40 μM glucose-6-phosphate, and various concentrations of fosfomycin (0-25 mg/mL, dissolved in H_2O). Plates were incubated at 37°C overnight and subsequent growth was noted and photographed.

In liquid cultures. Bacteria were added to 3 mL LB media containing 100 μg/mL ampicillin, 40 μM glucose-6-phosphate, and various concentrations of fosfomycin (0-20 mg/mL, dissolved in H_2O) to reach a final OD_{600} of 0.05. To assess the effect of FosA growth inhibitors Phosphonoformate (PF) and acetylphosphonate (AcP), 10-100 μM of either compound were added to cultures containing 20 mg/mL fosfomycin. All cultures were incubated at 37°C and shaken at 225 RPM, and growth was recorded.

Determination of P. putida *FosX Metal Preferences Using ^{31}P-NMR Spectroscopy*

A typical reaction involved 2.3 μM FosX preincubated for 10 mins with 100 μM Mn^{2+}, Fe^{2+}, Ni^{2+}, Co^{2+}, Cu^{2+}, or Ca^{2+}, or with 1 mM Mg^{2+} or Zn^{2+}, in 25 mM HEPES, pH 7.5. Reaction was initiated by the addition of 25 mM fosfomycin (pH 7.5 in H_2O) and allowed to proceed for several hours as needed to observe 10-15% product turnover. Reactions were quenched with 100 μL $CHCl_3$ and vigorous vortexing, followed by flash-freezing on dry ice. After ≥30 mins, reactions were thawed, centrifuged to separate precipitated protein, and the aqueous layer was gently rocked with Chelex resin for 1.5 hrs. Chelex was pelleted and removed, and the aqueous layer was used for NMR analysis after addition of solvent D_2O. Proton-decoupled spectra were collected at 121 MHz, with ^{31}P chemical shifts of 16.9 ppm for diol product and 11.1 ppm for fosfomycin.

Estimation of P. putida *Turnover Number (k_{cat}) Using ^{31}P-NMR Spectroscopy*

Reactions were carried out exactly the same way as for determination of metal preferences above. Turnover numbers were estimated by calculating the ratio of substrate and product peak heights and comparing to the amount of substrate used in the reaction, which yields the extent of product turnover.

Determination of P. putida *FosX Optimal pH Using ^{31}P-NMR Spectroscopy*

Reactions were carried out exactly the same way as for determination of metal preferences above, but with different buffers in desired pH range. The selected buffers tested the reaction efficiency at pH 5.5 (25 mM MES), pH 6.5 (25 mM MES), pH 7.5 (25 mM

HEPES), pH 8.5 (25 mM CHES), and pH 9.5 (25 mM CHES).

Determination of P. putida *FosX Promiscuous Catalytic Activity Using ^{31}P-NMR Spectroscopy*

Reactions were carried out exactly the same way as for determination of metal preferences above, but with minor modifications. To test ability of the enzyme to perform the FosA reaction, enzyme was preincubated with 100 μM Mn^{2+} and initiated with 25-200 mM GSH (dissolved in H_2O, pH 7.5). Reaction buffer 25 mM HEPES pH 7.5 was prepared with or without 100 mM KCl to test K^+ activation of FosA reaction. To test ability of the enzyme to perform the FosB reaction, enzyme was preincubated with 100 μM Mg^{+2} and initiated with 25-200 mM *L*-cys (dissolved in H_2O, pH 7.5). Reactions were quenched as above.

CHAPTER IV

LISTERIA MONOCYTOGENES FOSX DYNAMICS VARY BASED ON CATALYTIC METAL AS DETERMINED BY HYDROGEN-DEUTERIUM EXCHANGE MASS SPECTROMETRY

Many examples of decreased structural perturbations and protein dynamics upon ligand binding to protein exist in the literature. This work, however, includes the observation of a rare phenomenon; *increased* solvent accessibility and global conformational changes occur when divalent metal ion cofactors bind to *Listeria monocytogenes* FosX, the extent of which is directly proportional to the metal's ability to catalyze hydrolysis of FosX substrate fosfomycin. Previous work has shown that metal preference is as follows: Mn^{2+}>Co^{2+}>>Zn^{2+} (24). (**Note:** Due to a flaw in the graphing program that was used to generate the plots below, displaying more than one trace on the same plot causes the best-fit curves to appear skewed as compared to plotting one trace alone. However, the program generated identical amplitude and rate constants regardless of how the traces were displayed. To view the curves separately and verify that the lines fit the data better than the plots in this section seem to indicate, please see Appendix B.)

Results

Identification of Peptic Fragments

Three independently generated peptic maps with pepsin, *Aspergillus* protease XIII, and *Rhizopus* protease XVIII yielded 98% overall protein coverage. The pepsin map covers 85% of the protein, *Aspergillus* protease XIII covers 78%, and *Rhizopus* protease XVIII covers 69%. These contain several areas of heavy overlap permitting enhanced spatial resolution. Peptide maps showing all sequenced and identified peptides are in Appendix A.

FosX Dynamics at Metal Binding Residues

Crystal structures of this protein reveal three residues that coordinate a divalent metal ion to the FosX dimer: H7, H69, and E118, and one additional questionable residue, E126, that has not been shown to coordinate metal to the protein in any other organism (Figure 15). Intuitively, one would expect the structure of a protein to become more rigid upon binding ligand, because the act of binding translates to increased structure and therefore less solvent accessibility. However, upon observation of FosX dynamics in the

presence of three metal ion cofactors Mn^{2+}, Co^{2+}, and Zn^{2+}, we learn that this assumption is incorrect.

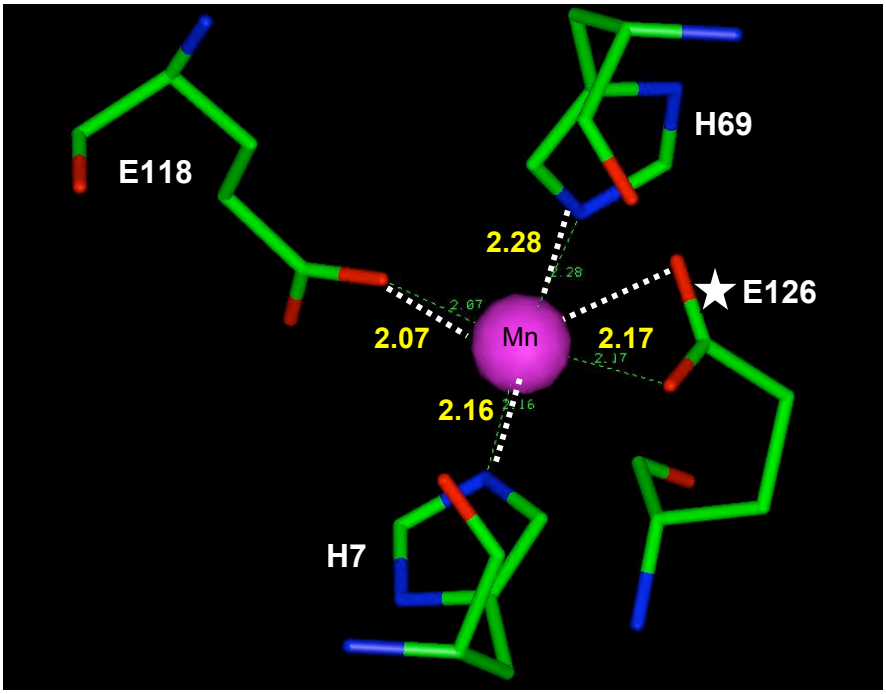

Figure 15. Mn^{2+}-bound FosX showing metal coordination residues and distances from Mn^{2+} center.

Metal binding residue H7. The peptides 1-5 and 1-10 can be used to assess how metal binding to FosX impacts residue H7. Figure 16 and Table 4 show that while the exchange behaviors of native enzyme and enzyme bound to Co^{2+} or Zn^{2+} are virtually identical, exchange with bound Mn^{2+} is about 30% faster. Comparing these rates with those of peptide 1-5, showing very fast exchange that differs among the four species by 5% at most, we deduce that the C-terminal half of peptide 1-10 is responsible for the differences in exchange. Peptide 6-10 was not found in enough HXMS trials to allow statistically significant analysis, so the subtraction method must suffice here. Therefore, increased exchange in the area of residues 6-10, which includes binding residue H7, is Mn^{2+}-dependent, with HXMS profiles of Co^{2+}- and Zn^{2+}-bound protein nearly identical to native enzyme. Segment 6-10 is a β-strand on the crystal structure, while 1-5 is an unstructured loop.

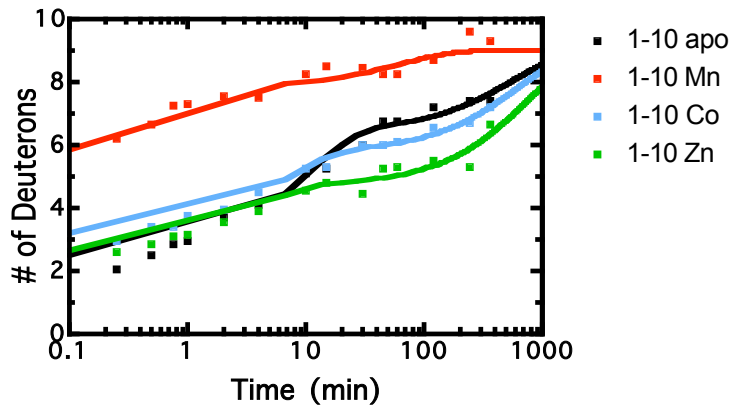

Figure 16. HXMS backbone amide kinetic profile for peptide 1-10.

Table 4. Rate constants and amplitudes for peptides 1-5 and 1-10.

sample	peptide	A_1 (D)	k_1 (min-1)	A_2 (D)	k_2 (min-1)
Native	1-5	0.62 ± 0.04	0.04 ± 0.01		
Mn^{2+}		0.46 ± 0.06	0.11 ± 0.05		
Co^{2+}		0.57 ± 0.06	0.05 ± 0.02		
Zn^{2+}		0.50 ± 0.09	0.06 ± 0.04		
Native	1-10	4.0 ± 0.3	0.10 ± 0.02	2.6± 0.3	(1.7 ± 0.7) x 10^{-3}
Mn^{2+}		2.3 ± 0.7	1.4 ± 0.7	1.2 ± 0.3	0.016 ± 0.009
Co^{2+}		3.2 ± 0.1	0.16 ± 0.03	2.6 ± 0.1	(1.6 ± 0.3) x 10^{-3}
Zn^{2+}		4.3 ± 0.2	0.3 ± 0.1	2.1 ± 0.3	(1.3 ± 0.3) x 10^{-3}

Metal binding residue E118. Peptide 117-124 contains metal coordination residue E118. FosX bound to Mn^{2+} exhibits an 87% fast exchange rate, followed by 73% for Co^{2+}, followed by Zn^{2+} and native protein which are roughly equal at 66% and 64%, respectively. Although this region of the protein exchanges quickly in all four species, the statistically significant results are consistent with the fastest exchange occurring with the preferred divalent metal Mn^{2+}. As the metal preference decreases to Co^{2+} and then Zn^{2+}, so does the speed of amide hydrogen exchange. Plots and rate data are exhibited in Figure 17 and Table 5 below, with similar amplitudes and rates displayed for peptide 117-125 to show the reproducibility of results gleaned from this technique.

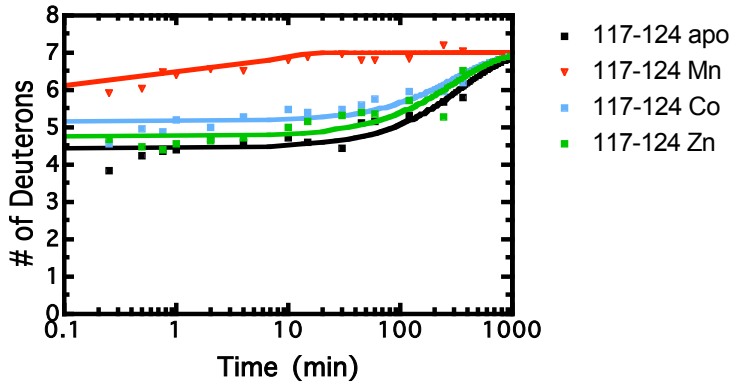

Figure 17. HXMS backbone amide kinetic profile for peptide 117-124.

Table 5. Rate constants and amplitudes for peptides 117-124 and 117-125.

sample	peptide	A_1 (D)	k_1 (min-1)	A_2 (D)	k_2 (min-1)
Native	117-124	2.55 ± 0.09	(2.8 ± 0.6) x 10^{-3}		
Mn^{2+}		0.9 ± 0.1	0.21 ± 0.09		
Co^{2+}		1.9 ± 0.1	(3.2 ± 0.9) x 10^{-3}		
Zn^{2+}		2.2 ± 0.1	(3.3 ± 0.8) x 10^{-3}		
Native	117-125	1.6 ± 0.3	1.1 ± 0.4	2.3 ± 0.1	(2.1 ± 0.4) x 10^{-3}
Mn^{2+}		1.10 ± 0.08	0.10 ± 0.03		
Co^{2+}		1.9 ± 0.1	0.020 ± 0.005		
Zn^{2+}		2.2 ± 0.2	0.010 ± 0.004		

Peptide 110-116 comprising a turn between two β-strands shows an exchange pattern that echoes the fast exchange trend of peptide 117-124 above. This not only provides verification that the results we see are likely correct, but also supports the notion that the entire protein must orient itself in such a way as to facilitate metal binding. It makes sense that this peptide near a metal binding residue would experience a structural perturbation to accommodate approach of the metal cation to the active site. This peptide, similar to 117-124, displays different kinetics for each of the four species in fast, intermediate, and slow exchange regimes, suggesting both an increase in solvent dynamics and a decrease in overall structure as the protein binds a more catalytically relevant metal (Figure 18, Table 6).

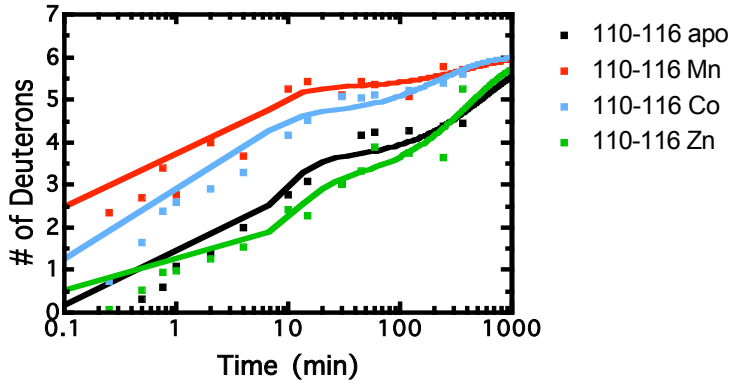

Figure 18. HXMS backbone amide kinetic profile for peptide 110-116.

Table 6. Rate constants and amplitudes for peptides 110-116.

sample	peptide	A_1 (D)	k_1 (min-1)	A_2 (D)	k_2 (min-1)
Native	110-116	2.4 ± 0.3	0.17 ± 0.05	3.4 ± 0.3	(1.7 ± 0.8) x 10^{-3}
Mn^{2+}		2.8 ± 0.3	0.25 ± 0.09	0.8 ± 0.3	0.002 ± 0.002
Co^{2+}		3.4 ± 0.4	0.3 ± 0.1	1.4 ± 0.3	0.004 ± 0.002
Zn^{2+}		2.9 ± 0.3	0.11 ± 0.05	2.5 ± 0.4	(2.5 ± 0.8) x 10^{-3}

Putative metal binding residue E126. One crystal structure of *Listeria monocytogenes* FosX shows that residue E126 is within coordination distance of the divalent Mn^{2+} cation. Although several short peptides spanning the C-terminal tail region were pinpointed in mapping experiments, the only one for which a consistent signal was observed during HXMS experiments was the long peptide 125-133, an α-helix in the structure. Since HXMS amplitudes and rate constants are averages of every amide hydrogen exchange along a peptide, it is impossible to deduce the dynamic properties at the precise residue E126. From Figure 19 and Table 7, however, we can equivocally state that exchange is very fast in the region *around* E126--about 80-85% for Co^{2+} and Zn^{2+}, 100% for Mn^{2+} (program could not fit data because exchange was complete by 15s), and 50% for apoenzyme (Although the best-fit lines look quite similar for the four species, the few low points at the beginning of the time course for native enzyme have been quite reproducible and should not be considered outliers.). Thus, these data again suggest that exchange increases proportionally with FosX preference for metal cofactor. The rapid exchange for this peptide is contrary to our

expectations for a helical peptide, which by nature is a moderately rigid element of secondary structure.

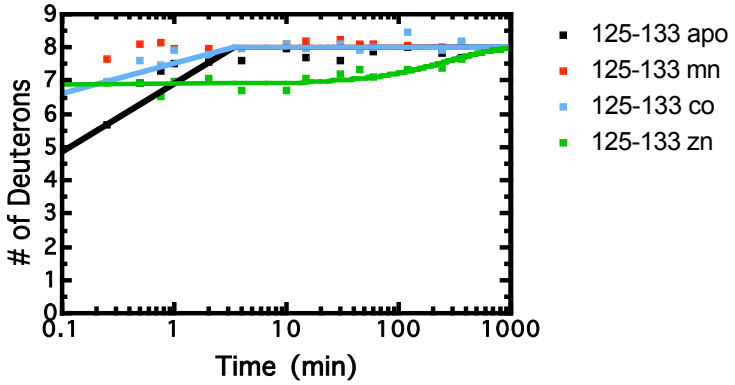

Figure 19. HXMS backbone amide kinetic profile for peptide 125-133.

Table 7. Rate constants and amplitudes for peptide 125-133.

sample	peptide	A_1 (D)	k_1 (min-1)	A_2 (D)	k_2 (min-1)
Native	125-133	4.0 ± 0.8	2.3 ± 0.5		
Mn^{2+}		100% exchange @ 15 s			
Co^{2+}		1.7 ± 0.6	2.2 ± 0.8		
Zn^{2+}		1.10 ± 0.06	0.004 ± 0.001		

FosX Dynamics at Regions Removed from Active Site

Though we often place little importance on regions of a protein that are not part of the catalytic active site, data presented here suggest that these residues do in fact play a role in catalysis despite their location several angstroms away from the activity center.

Peptide 11-21. This peptide does not contain any metal binding or substrate recognition sites, and it is the farthest away from the metal center than any other area of the protein. Nevertheless, we continue to observe the Mn^{2+}>Co^{2+}>Zn^{2+}≈native fast exchange trend explained above (Figure 20). Although the rate differences are not as pronounced in this example, they are still statistically relevant (Table 8). Constants for peptide 11-22 are also displayed to show the reproducibility of the results gleaned from this technique.

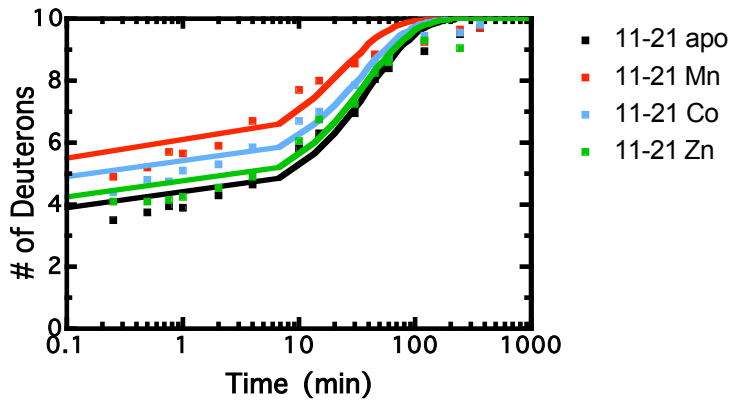

Figure 20. HXMS backbone amide kinetic profile for peptide 11-21.

Table 8. Rate constants and amplitudes for peptides 11-21 and 11-22.

sample	peptide	A_1 (D)	k_1 (min-1)	A_2 (D)	k_2 (min-1)
Native	11-21	6.1 ± 0.2	0.025 ± 0.003		
Mn^{2+}		4.5 ± 0.2	0.043 ± 0.008		
Co^{2+}		5.1 ± 0.2	0.032 ± 0.003		
Zn^{2+}		5.8 ± 0.2	0.027 ± 0.003		
Native	11-22	6.5 ± 0.3	0.015 ± 0.003		
Mn^{2+}		4.3 ± 0.2	0.43 ± 0.008		
Co^{2+}		4.8 ± 0.2	0.016 ± 0.003		
Zn^{2+}		6.0 ± 0.3	0.019 ± 0.004		

Peptide 22-29. This peptide covers the last few residues of the α-helix spanned by above peptide 11-21, and the beginning of a large loop whose exact length is unknown due to missing electron density in the crystal structure. As is the case with 11-21, this peptide does not contain any functionally significant residues and is removed from the active site, yet the same exchange trend is observed. The amide protons comprising this peptide exchange significantly throughout the time course in the intermediate and slow phases, suggesting a conformational change rather than heightened solvent accessibility. Several peptides spanning this area were isolated from the peptide mapping experiment and the HXMS results from each are shown to convey reproducibility in Table 9. The exchange plot for peptide 22-29 is shown in Figure 21.

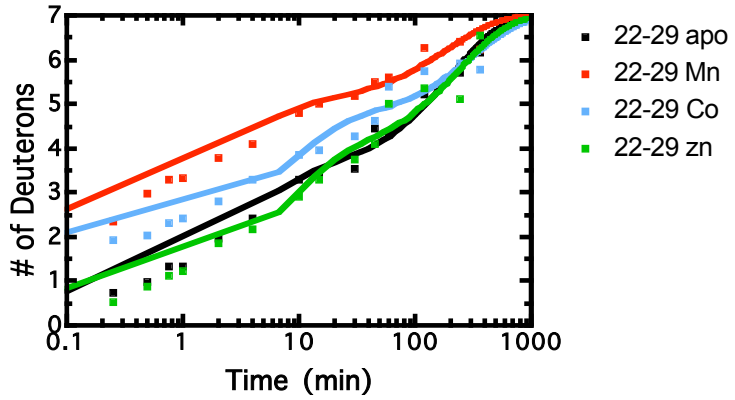

Figure 21. HXMS backbone amide kinetic profile for peptide 22-29.

Table 9. Rate constants and amplitudes for peptides 22-26, 22-28, and 22-29.

sample	peptide	A_1 (D)	k_1 (min-1)	A_2 (D)	k_2 (min-1)
Native	22-26	3.83 ± 0.06	(4.8 ± 0.4) x 10^{-3}		
Mn^{2+}		2.9 ± 0.1	0.009 ± 0.002		
Co^{2+}		3.08 ± 0.06	(3.5 ± 0.4) x 10^{-3}		
Zn^{2+}		3.80 ± 0.06	(3.5 ± 0.3) x 10^{-3}		
Native	22-28	3.5 ± 0.1	0.31 ± 0.09	2.0 ± 0.2	(5.0 ± 0.6) x 10^{-3}
Mn^{2+}		1.9 ± 0.2	0.12 ± 0.03	1.4 ± 0.2	(2.6 ± 0.9) x 10^{-3}
Co^{2+}		1.7 ± 0.3	0.5 ± 0.2	2.3 ± 0.2	0.005 ± 0.001
Zn^{2+}		3.6 ± 0.2	0.20 ± 0.07	2.2 ± 0.2	(4.4 ± 0.7) x 10^{-3}
Native	22-29	2.7 ± 0.2	0.26 ± 0.06	3.6 ± 0.2	(4.8 ± 0.6) x 10^{-3}
Mn^{2+}		2.4 ± 0.3	0.3 ± 0.1	2.0 ± 0.2	0.005 ± 0.001
Co^{2+}		2.5 ± 0.3	0.12 ± 0.04	2.5 ± 0.3	0.003 ± 0.001
Zn^{2+}		2.9 ± 0.4	0.13 ± 0.05	3.3 ± 0.4	0.004 ± 0.001

Peptide 54-62. The exchange results for this peptide are quite dramatic; the rates and amplitudes for native enzyme, Co^{2+}, and Zn^{2+} are virtually identical (they differ by <5%), while exchange of FosX bound to Mn^{2+} is >20% higher. This further demonstrates that a global conformational change is somehow induced upon binding to the catalytically preferred metal (Figure 22, Table 10).

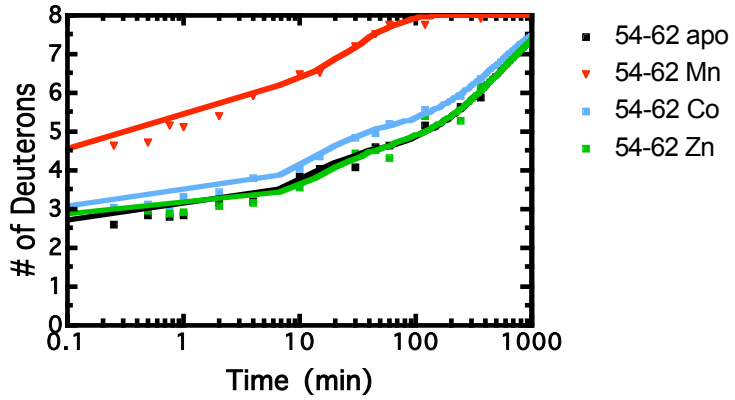

Figure 22. HXMS backbone amide kinetic profile for peptide 54-62.

Table 10. Rate constants and amplitudes for peptide 54-62.

sample	peptide	A_1 (D)	k_1 (min-1)	A_2 (D)	k_2 (min-1)
Native	54-62	3.7 ± 0.1	0.10 ± 0.02	1.6 ± 0.1	(1.8 ± 0.2) x 10^{-3}
Mn^{2+}		1.3 ± 0.2	0.6 ± 0.2	2.3 ± 0.2	0.034 ± 0.004
Co^{2+}		3.2 ± 0.1	0.09 ± 0.02	1.8 ± 0.1	(1.8 ± 0.2) x 10^{-3}
Zn^{2+}		3.7 ± 0.2	0.07 ± 0.03	1.4 ± 0.2	(1.8 ± 0.4) x 10^{-3}

Exchange Near Catalytic Base E44 Reveals Novel Mechanism

Perhaps the most striking observations from these experiments concern the structural fluctuations that occur at and around residue E44, which is the general base responsible for adding water to the oxirane carbon of fosfomycin. Previous work has shown that mutating this residue to glycine completely abolishes FosX activity (24). Data in this section indicate that increased dynamic motion around this site is necessary to enable fosfomycin hydrolysis and appears to be a function of which metal cofactor is bound to protein.

Peptides 40-46 and 42-46 containing E44. Like peptides 1-10 and 1-5 discussed earlier, observing the exchange rates for overlapping peptides permits enhanced spatial resolution, and in this case gives us a better idea of the dynamics near critical residue E44 than can be afforded by either peptide alone. Analysis of exchange rates for peptide 40-46 shows that

the profiles are very similar; rapid exchange by the first time point is approximately 40% for all species (Figure 23 left, Table 11). However, for peptide 42-46, we see that while there is no exchange by 15 s for native and Co^{2+}-bound enzyme, exchange with bound Mn^{2+} is 40% complete (Figure 23 right, Table 11).

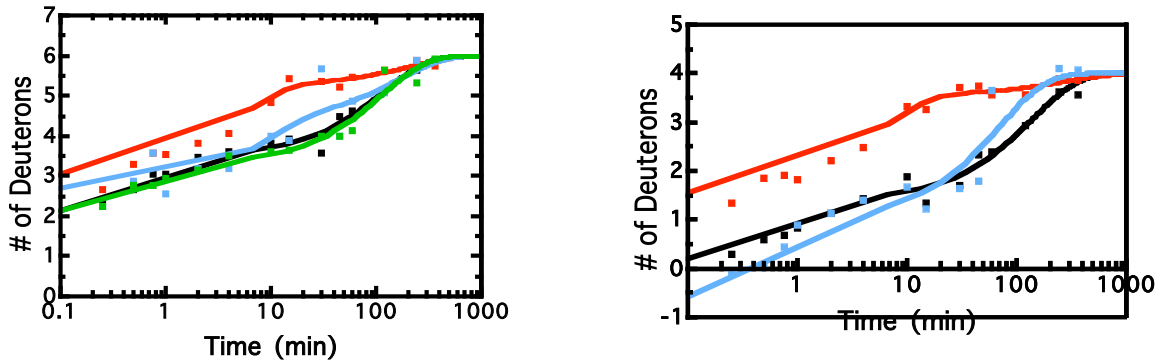

Figure 23. HXMS backbone amide kinetic profiles for peptides 40-46 (left) and 42-46 (right).

Table 11. Rate constants and amplitudes for peptides 40-46 and 42-46.

sample	peptide	A_1 (D)	k_1 (min-1)	A_2 (D)	k_2 (min-1)
Native	40-46	1.6 ± 0.4	1.3 ± 0.5	2.5 ± 0.1	0.009 ± 0.001
Mn^{2+}		2.3 ± 0.2	0.20 ± 0.06	0.8 ± 0.2	0.005 ± 0.003
Co^{2+}		1.7 ± 0.8	0.12 ± 0.11	1.6 ± 0.8	0.006 ± 0.006
Zn^{2+}		1.4 ± 0.5	1.2 ± 0.8	2.7 ± 0.2	0.009 ± 0.002
Native	42-46	1.3 ± 0.3	0.8 ± 0.4	2.6 ± 0.1	0.007 ± 0.001
Mn^{2+}		0.5 ± 0.1	0.18 ± 0.04	2.0 ± 0.1	0.004 ± 0.003
Co^{2+}		3.0 ± 0.4	1.7 ± 1.5	1.9 ± 1.1	0.014 ± 0.005
Zn^{2+}					

Peptide 45-47. The most significant change in dynamics across the entire protein is seen in this short peptide adjacent to residue E44. Fast exchange with bound Mn^{2+} is 50% greater than that of native, Co^{2+}-bound, or Zn^{2+}-bound enzyme (rates of these three differ by <5%). This peptide is also interesting because the only species experiencing full exchange of both deuterons is Mn^{2+}-bound FosX; the other three species appear to exchange only one hydrogen for deuterium. The HXMS data shown in Figure 24 and Table 12 demonstrate that a conformational change dependent on metal ion is occurring at this peptide. A

possible reason for this observation is that this region of the protein forms a channel to allow approach of the catalytic water molecule; this would explain why the fast exchange trend always proceeds from most preferred metal to least preferred metal. A more detailed discussion of this theory follows in the proceeding section.

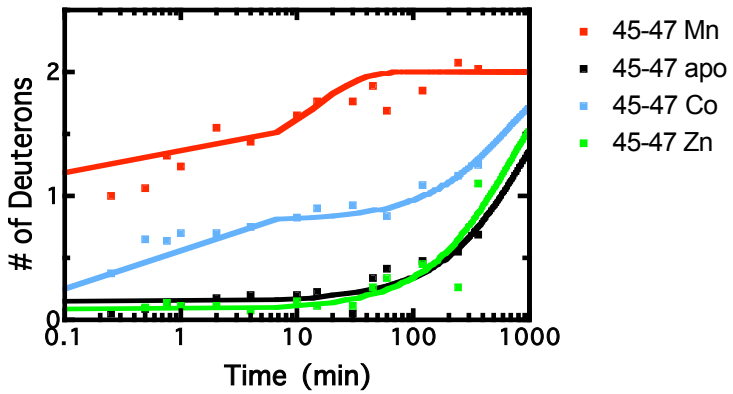

Figure 24. HXMS backbone amide kinetic profiles for peptide 45-47.

Table 12. Rate constants and amplitudes for peptides 40-46 and 42-46.

sample	peptide	A_1 (D)	k_1 (min-1)	A_2 (D)	k_2 (min-1)
Native	45-47	1.85 ± 0.03	(1.1 ± 0.2) x 10^{-3}		
Mn^{2+}		0.82 ± 0.08	0.08 ± 0.03		
Co^{2+}		0.7 ± 0.2	2.2 ± 0.9	1.20 ± 0.03	(1.5 ± 0.02) x 10^{-3}
Zn^{2+}		1.91 ± 0.05	(1.4 ± 0.3) x 10^{-3}		

Summary of HXMS data

The color-coded ribbon diagrams showing the fast exchange percentages for native, Mn^{2+}-bound, Co^{2+}-bound, and Zn^{2+}-bound enzyme are shown below in Figure 25. Examination of these structures emphasizes that the act of binding Mn^{2+} increases solvent accessibility throughout the protein, as indicated by the abundance of red segments (indicating >80% fast exchange). The Co^{2+} structure can be regarded as an exchange intermediate, lying between the abundant fast exchange of the Mn^{2+} structure and the minimal fast exchange of the Zn^{2+} and apoenzyme structures. As only very small percentages separate the exchange rates of Zn^{2+} and apoenzyme, these structures appear

virtually identical. The exchange rates for these species follow the previously observed trend in *Listeria monocytogenes* Fos X metal preference: Mn^{2+}>Co^{2+}>>Zn^{2+}≈apo.

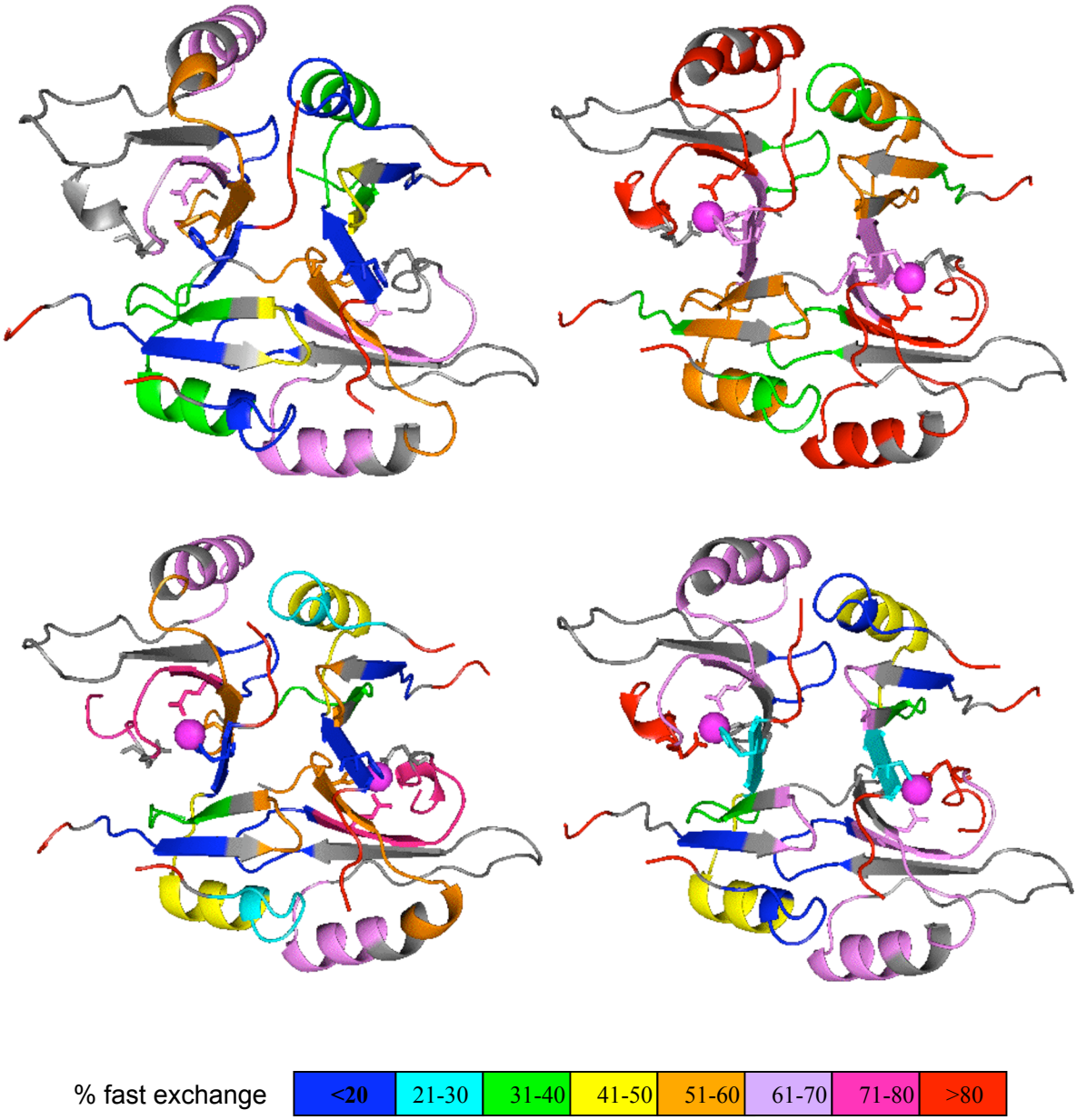

Figure 25. Ribbon diagrams illustrating fast exchange percentages for certain peptides selected to maximize protein coverage (clockwise from top left: native, Mn^{2+}-bound, Zn^{2+}-bound, Co^{2+}-bound).

Discussion

The results presented above demonstrate that the level of fast exchange, reflective of solvent accessibility and/or structural perturbations, peaks upon binding the preferred metal cation Mn^{2+}. As catalytic activity decreases with binding to less preferred metals, the exchange rates begin to more closely resemble those of the native enzyme. To verify that Mn^{2+} is not acting as a Lewis base to catalyze exchange, the distances between each backbone amide nitrogen and the nearest Mn^{2+} cation were measured. Appendix C shows that the rate does not depend on the distance from the metal. Although these experiments cannot determine the reason for this exchange phenomenon, examples in the literature can perhaps shed some light on this behavior and suggest future experiments to uncover the mechanism.

The protein Troponin C (TnC) is a Ca^{2+}-binding protein involved in regulating muscle contraction. When Ca^{2+} binds the protein, a conformational change signals neighboring protein Troponin I (TnI) to initiate a cascade of structural changes that ultimately results in contraction of the muscle. An H/D exchange NMR experiment probing the solution dynamics of TnC reveals that when the protein binds to Ca^{2+}, the structure undergoes a conformational opening whereby a hydrophobic patch necessary for binding TnI is exposed. NMR spectra reveal that both of the regulatory Ca^{2+} binding sites experience an increase in deuterium incorporation by several deuterons. Most of the protein shows faster exchange after binding metal, while the first approximately 30 residues maintain the same level of exchange as native TnC (41). Likening this example to FosX, it is possible that the FosX structure must open or partially unfold in such a way as to expose the fosfomycin binding site. (We have previously shown that FosX binding is ordered, with metal preceding fosfomycin.) This structural opening would be most stimulated by the most catalytically relevant metals, explaining why the dynamics are so much greater for Mn^{2+}, followed by Co^{2+} and finally Zn^{2+}.

Another example concerns β_2-microglobulin, a component of the major histocompatibility complex I that can form amyloid fibrils and aggregate in bone and joint tissue. Experiments show that Cu^{2+} increases dynamics throughout the protein and especially at the four metal binding residues. This conformational motion caused by Cu^{2+} is thought to be responsible for amyloid formation and does not occur in the presence of other divalent metals. To explain their findings, the authors state their theory that the binding of Cu^{2+} leads to a destabilization of the protein's native state that exhibits decreased stability

and increased flexibility. The shift to a destabilized state spreads cooperatively throughout the protein as hydrogen bonds and hydrophobic interactions are weakened, thus translating into a global increase in protein dynamics (42).

The idea of a partially folded FosX intermediate recalls the concept of protein folding "energy funnels." The current view of the protein folding problem is that there is no specific route by which a protein adopts its native conformation; rather, it can occur in many different ways, three of which are illustrated and explained below (Figure 26). In all of these hypothetical energy landscapes, a particular event is necessary to propel the protein over an energy barrier so that it can reach its native conformation. Until this event occurs, the protein is constantly in motion, in some cases adopting a higher entropy structure until it can "find its way downhill" to the bottom of the energy funnel (43). In the case of FosX, it may be that the binding of Mn^{2+} shifts the protein into a partially unfolded or destabilized native state with higher entropy than the native structure. This can be viewed as one of the kinetic traps on an energy funnel. Perhaps the binding of fosfomycin initiates stabilization and refolding, allowing the entropy and the free energy to decrease.

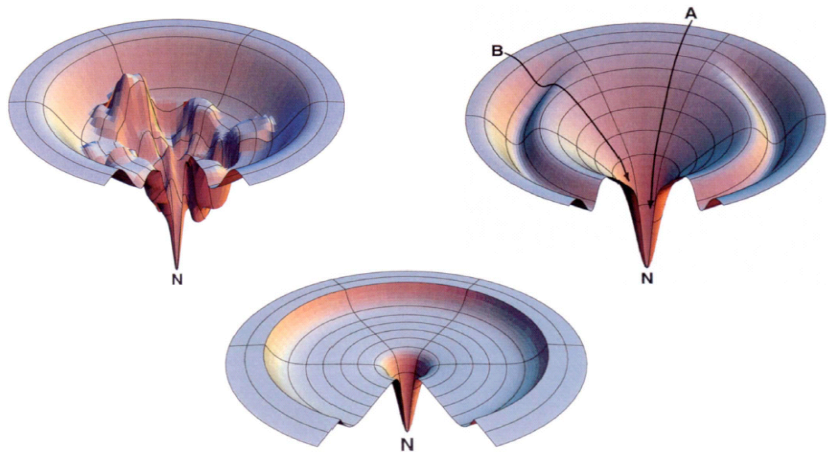

Figure 26. Protein folding landscapes, illustrating the complex paths a protein can take before arriving at its lowest energy state. Multiple routes are possible.

Another possible explanation for increased exchange with bound Mn^{2+} that does not concern protein folding can be illustrated by the behavior of peptides 42-46 and 45-47. Again, peptide 45-47 experiences the largest fast exchange percentage increase of any other peptide. Perhaps before FosX binds to metal, hydrogen bonding forces within the protein and interactions with ordered waters surrounding the protein are strong, thereby decreasing the overall flexibility of the structure. Then when the metal binds, the water

molecules become more disordered and their interactions with the backbone weaken to increase overall flexibility, allowing for the approach of the mechanistic water molecule and fosfomycin through a channel to the active site (44). This would explain why we see increased motion when Mn^{2+} binds as opposed to Co^{2+} or Zn^{2+}; since Mn^{2+} confers the highest catalytic activity, its binding to FosX induces a change in motion, particularly near residues 42-47, that allows the water molecule to readily approach the active site where E44 will abstract a proton. The channel created by Co^{2+} is not as large, so the water cannot approach or orient itself as quickly as it can for Mn^{2+}. It follows that Zn^{2+}, which is a very poor catalytic metal, would be ineffective at producing this channel and as a result we observe dynamic motions characteristic to native protein.

Since the FosX peptic maps for two other acid proteases are complete, HXMS experiments should be performed using these proteases to verify the results we have collected and to enhance spatial resolution. Other metals should be tried as well to determine how the exchange rates relate to FosX preference for the metal. The preference scale is as follows: $Mn^{2+} >> Ni^{2+} >> Fe^{2+} > Co^{2+} > Mg^{2+} \approx Ca^{2+} >> Zn^{2+}$ (unpublished observations). It would also be beneficial to perform HXMS experiments on protein/metal/fosfomycin and protein/metal/diol product complexes; observing a decrease in exchange rates would substantiate the theory that Mn^{2+} binding results in a partially folded intermediate or destabilized native state of FosX whose entropy is lessened by binding to fosfomycin.

To investigate the protein folding issue, a pulsed quench HXMS experiment can be conducted using a stopped-flow apparatus. The concept underlying the experiment is very similar to canonical HXMS except that pulsed quench investigates protein dynamics on a much smaller time scale. The protein is incubated with D_2O and a denaturant to promote unfolding, and the sample is then rapidly diluted in H_2O to initiate the refolding process and catalyze exchange of D for H. In this sense, this procedure is backwards from standard HXMS, since pulsed quench will measure a *decrease* in mass. The refolding period is analogous to the protein/D_2O incubations in canonical HXMS, because in both procedures the protein is quenched at particular time points (45). From this experiment, we would be able to compare folding of the protein/metal complex with the protein/metal/fosfomycin complex. If we detect slower folding *without* fosfomycin, we can conclude that the protein structure is more disordered with bound metal, and that fosfomycin binding may stabilize the structure so catalysis can occur.

CHAPTER V

INVESTIGATIONS INTO *LISTERIA MONOCYTOGENES* FOSX STEADY STATE METAL BINDING

Results

The main reason for performing these binding experiments was to determine the number of metal equivalents needed to fully saturate the binding sites of FosX for the HXMS experiments, since incubation with an excess of metal resulted in high signal to noise and impossible peptide mass analysis in many cases. Metal excess was initially used when performing HXMS because we hypothesized that a possible reason for the lower catalytic rates with certain metals was due to ineffective binding. As a result, we incubated the protein with as many as five equivalents of metal in some cases. The following spectroscopic experiments were designed to clarify the binding saturation of FosX with its metal ion cofactors so that we could later obtain the best signal to noise possible in HXMS while still ensuring that we were capturing a realistic picture of the protein/metal structure dynamics.

Co^{2+} was chosen for absorbance experiments because of its strong spectroscopic signal, and based on the knowledge that it does supply catalytic activity, albeit modest, to FosX. The plot in Figure 27 displays the entire absorbance spectrum for the titration of Co^{2+} into a predetermined concentration of protein. Binding saturation was monitored by calculating the absorbance difference between 470 nm and 424 nm, since the peak height was observed to level off in a series of preliminary experiments. No other selected wavelength(s) yielded an interpretable data set, so we believe this range is an ideal reporter of metal binding. The data in Figure 28 were obtained by correcting these absorbance values for background and dilution and plotting them versus concentration to determine the number of Co^{2+} equivalents needed to saturate FosX binding sites. Data points plateau at one equivalent [Co^{2+}]:[FosX], consistent with our original assumption that binding is stoichiometric. From this observation, adding one equivalent of Co^{2+} to FosX for HXMS binding experiments is necessary and sufficient to obtain an accurate profile of Co^{2+}-bound protein.

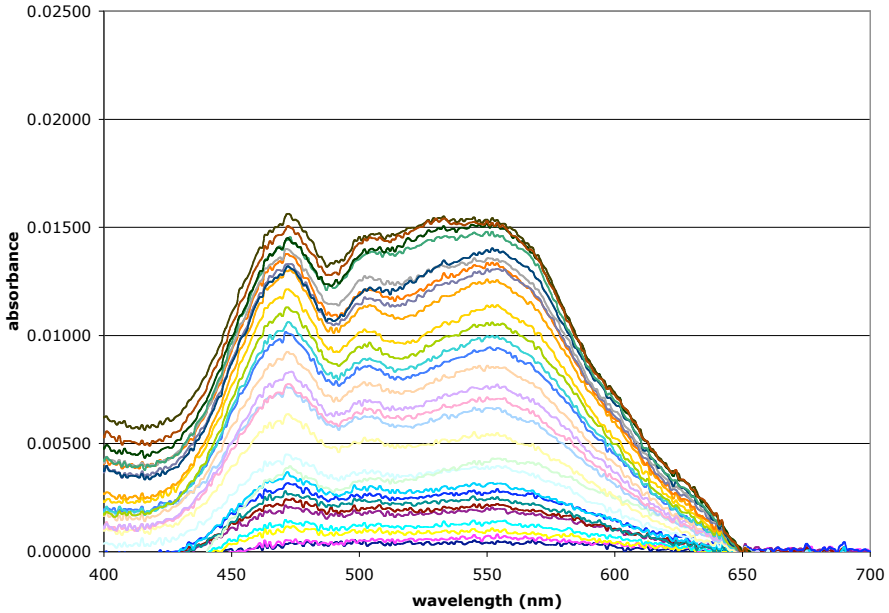

Figure 27. Ligand field envelope region of absorption spectra collected as increasing amounts of Co^{2+} (0-400 uM) were titrated into protein sample (200 uM).

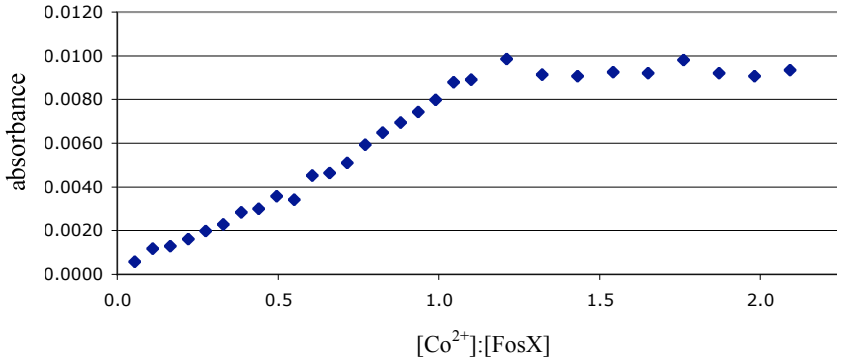

Figure 28. FosX absorbance saturation with **Co^{2+}** as a function of the ratio [Co^{2+}]:[FosX]. Absorbance reported is the result of difference spectroscopy between 470 and 424 nm.

Competition experiments whereby Mn^{2+} and Zn^{2+} were used to displace bound Co^{2+} were used to assess binding properties of these two metals, because they are spectroscopically silent. Unfortunately, results were inconclusive using the absorbance technique (data not shown). As a result, fluorescence was used as an alternate technique and proved to be very effective. First, the Co^{2+} titration experiment was repeated to verify that the number of saturating equivalents obtained was equal to the absorbance results.

Figure 29 shows that results produced are virtually identical, with a fluorescence plateau at approximately one equivalent. [Co^{2+}]:[FosX]. The segment leading up to the plateau is linear, permitting curve fitting analysis with a 1:1 binding model to determine K_D. Such an analysis cannot performed here, however, because a metal chelator is not present (more on this topic in Discussion).

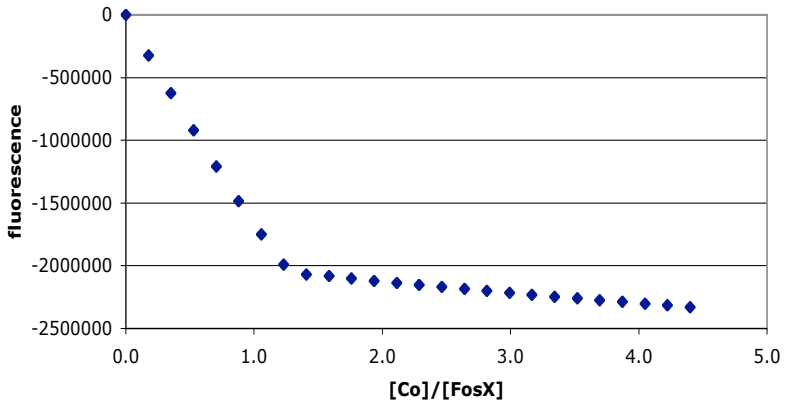

Figure 29. FosX fluorescence saturation with **Co^{2+}** as a function of the ratio [Co^{2+}]:[FosX]. Fluorescence reported is the result of difference spectroscopy between 470 and 424 nm.

An identical experiment to the one above with Co^{2+} was conducted to determine the binding stoichiometry of preferred metal Mn^{2+}. The fluorescence plot shown in Figure 30 reveals that although the data points appear to level off around 1-1.5 equivalents [Mn^{2+}]:[FosX], the shape of the curves are very different from those resulting from Co^{2+} binding. The segment leading to the approximate plateau is surely not linear as we saw with Co^{2+}; instead, it is best fit to a sigmoidal curve, implying that binding to this metal occurs in a different fashion than to Co^{2+}. Details on possible reasons for the shape observed here follow in the discussion section. What we can deduce, however, is that one equivalent [Mn^{2+}]:[FosX] should suffice for binding saturation in HXMS experiments.

The Zn^{2+} competition experiment with Co^{2+} also yields an approximately stoichiometric saturation value of one equivalent [Zn^{2+}]:[FosX] (Figure 31). Because the points preceding the plateau point connect in a linear fashion as was the case with Co^{2+}, the data can be fit to a 1:1 binding model under the proper conditions explained in the next section.

These experiments reveal that binding of Mn^{2+}, Co^{2+}, and Zn^{2+} to FosX occurs in stoichiometric fashion, permitting HXMS evaluation to be performed with only one equivalent

of metal in the incubation step. However, the dissimilar curve shapes among these metals indicate that the cofactors may have different protein binding mechanisms.

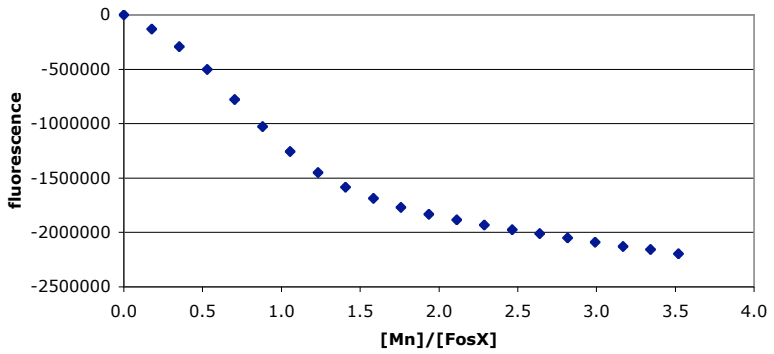

Figure 30. FosX fluorescence saturation with **Mn^{2+}** as a function of the ratio [Mn^{2+}]:[FosX]. Fluorescence reported is the result of difference spectroscopy between 470 and 424 nm.

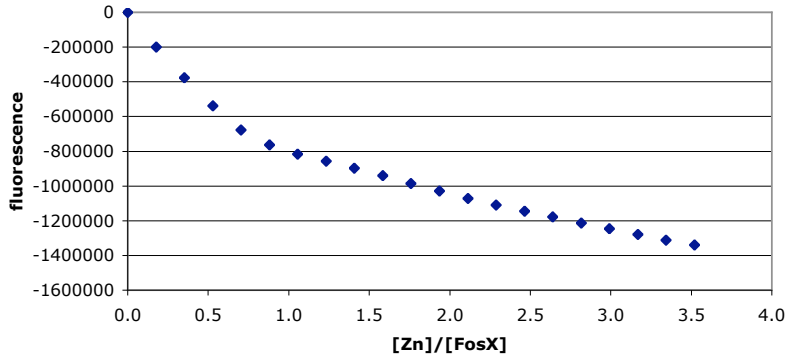

Figure 31. FosX fluorescence saturation with **Zn^{2+}** as a function of the ratio [Zn^{2+}]:[FosX]. Fluorescence reported is the result of difference spectroscopy between 470 and 424 nm.

Discussion

Although the Co^{2+} titration experiment produced data points that can be extrapolated to a 1:1 binding equation, the K_D yielded from such an analysis would be merely an upper limit, since these experiments were performed with an excess of metal. The upper limit K_D derived with extrapolation from the above Co^{2+} plot is 0.33 μM. For the most accurate determination of dissociation constants for each metal, however, a chelator should be present in a higher concentration than the metal so as to buffer the amount of free metal in solution. A common chelator used for this purpose is EGTA (39, 40). An accurate K_D for each metal can be obtained in the future using this technique.

The reason for the sigmoidal shape of the Mn^{2+} titration curve is unknown at this point. A possible explanation is that the cuvette contained a competing metal species, either from inadequate acid soaking of the cuvette to remove contaminants or from a metal other than Mn^{2+} being present in the Mn^{2+} stock used in the titration. This experiment should be repeated with a new Mn^{2+} stock to determine if metal contamination is the problem. Another possibility is that the metal/protein solution did not sufficiently equilibrate. Incubation times greater than ten minutes may lead to increased linear character of the data points. However, the likelihood remains that the sigmoidal shape of this curve is due to a complex binding mechanism between Mn^{2+} and FosX.

Figure 32 displays the superposition of the fluorescence titration data points for Mn^{2+} and Zn^{2+} and emphasizes that the shapes, as well as the fluorescence values themselves, are indeed very different. The fact that the plateaus do not occur at the same point along the y-axis implies that the protein fluoresces differently when bound to one metal versus another, and could be related to the differences in amide hydrogen observed for each metal. Further insights into the binding mechanisms of these metals cannot be determined from these studies, but future work including stopped-flow experiments would help to elucidate pre-steady state information. Since steady state kinetics represent a composite calculation of several microscopic rate constants, understanding the pre-steady state rates that make up the k_{cat} and K_M values will provide additional valuable information about the FosX reaction.

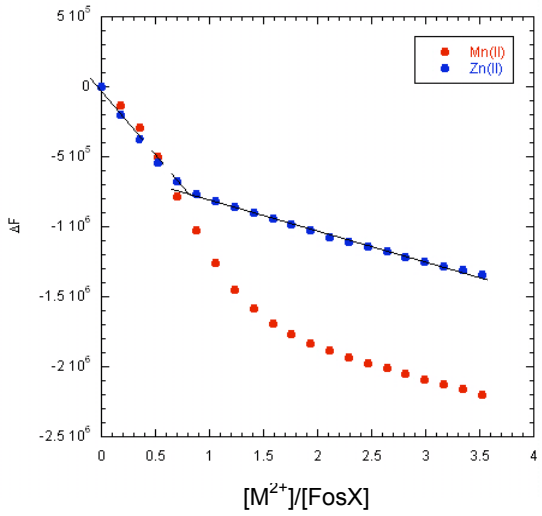

Figure 32. Superposition of Mn^{2+} and Zn^{2+} fluorescence titration data.

CHAPTER VI

CHARACTERIZATION OF A NOVEL FOSX ENZYME FROM THE *PSEUDOMONAS PUTIDA* GENOME

Results

Expression and Purification of Pseudomonas putida *FosX*

Because of the high purity of protein yield afforded by the cation exchange SP Sepharose column, only one column was needed for purification of the putative FosX enzyme (Figure 33). Final yield was 25 mg/L of protein. Actual molecular weight of 16150.18 Da as deduced from MALDI-MS spectrum (Figure 34) agrees with the theoretical value of 16,150 Da.

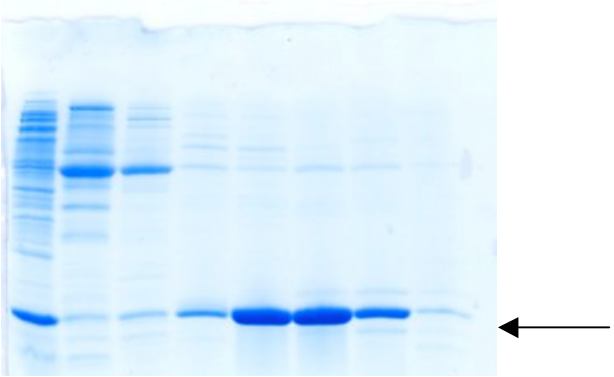

Figure 33. Purification gel with arrow marking the position of *Pseudomonas putida* FosX. Lane 1 is initial column flow-through.

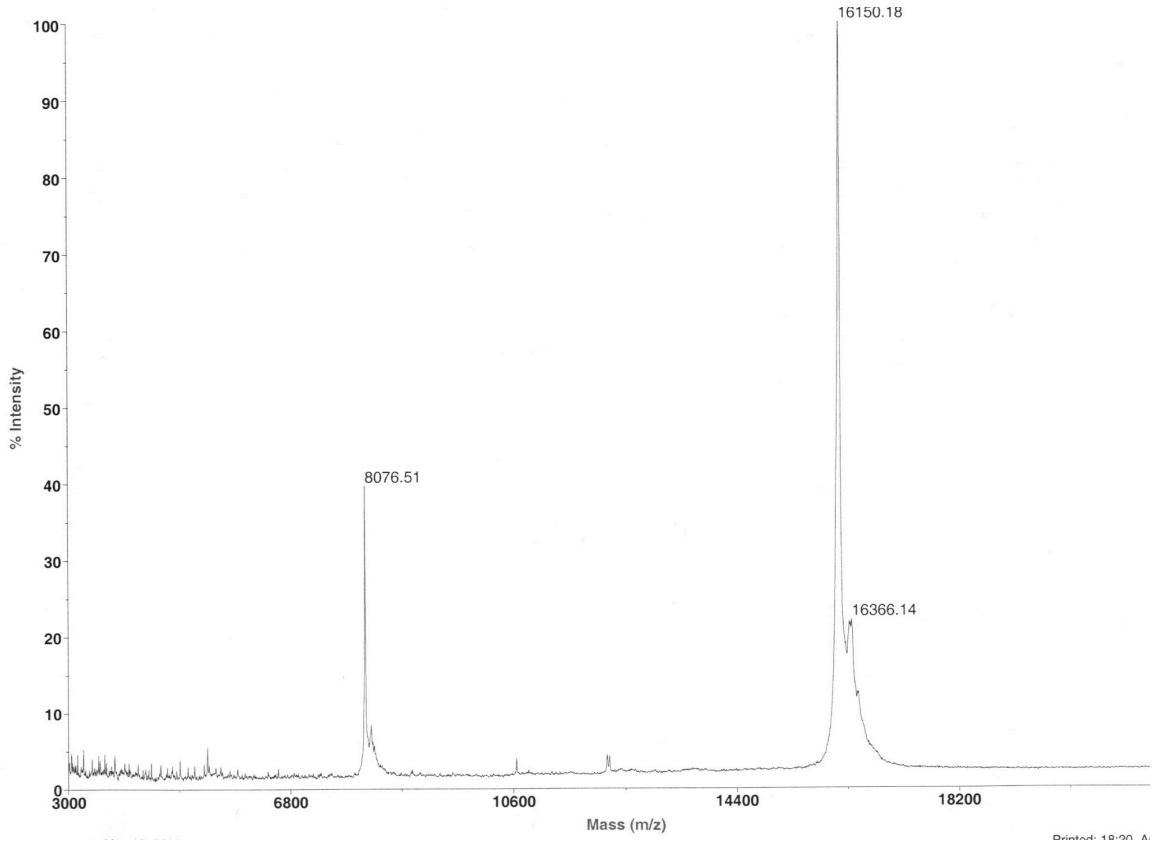

Figure 34. MALDI mass spectrum of *Pseudomonas putida* FosX at molecular weight of 16150 Da.

Determination of Minimum Inhibitory Concentration of Fosfomycin

Discovery of this protein's ability to confer fosfomycin resistance to *E. coli* cells will allow us to classify the enzyme as a true FosX. In order to provide a basis for comparison, cell growth was compared to cells that had been transformed with the robust *Listeria monocytogenes* FosX, whose fosfomycin MIC value has been established as >25 mg/mL. Resistance values above this cannot be accurately determined due to fosfomycin solubility. Empty pET20b(+) vector was also transformed into cells as a control and should be susceptible to fosfomycin treatment. MIC values, or the fosfomycin concentration at which bacterial no longer survive, are assessed by visually inspecting the plates or liquid cultures; thus the higher the value, the more resistance the enzyme confers.

Figure 35 shows the results of the plated cell growth assays. The *P. putida* enzyme clearly confers robust resistance to fosfomycin, since even in the presence of 20 mg/mL of the antibiotic, a lawn of bacterial colonies survive and appear to be healthier than those containing the gene from *Listeria*, which to this point has been regarded as the most resistant of all the FosX enzymes. Although the *Listeria* MIC value has been defined as >25 mg/mL, results shown here indicate that even though the colonies do survive, the number and size of the colonies diminish with increasing concentrations of fosfomycin.

A reason for the better health of *Pseudomonas* versus *Listeria* colonies on these plates is unclear at this time, since all cells were grown to an OD_{600} of 0.015 and plated simultaneously. The abundance and largeness of the *Pseudomonas* FosX-expressing colonies were reproducible across several experiments. Cells containing empty vector or FosX gene inserts were grown in small cultures according to their established expression protocols, so that expression of each would be as high as possible. As expected, the empty vector control showed complete obliteration of cell growth at fosfomycin concentrations greater than 0 mg/mL.

To ensure that the observed results were not due to experimental error (since it is rare for us to see such heightened resistance in FosX enzymes other than the one from *Listeria)*, a similar experiment was performed in liquid culture media. Growth was assessed by measuring the OD_{600} of cell cultures that had been treated with 0-20 mg/mL fosfomycin, and FosA inhibitors PF and AcP were added to 20 mg/mL fosfomycin cultures to determine if cell density increased. Table 13 shows that regardless of fosfomycin or FosA inhibitor concentration, cell growth is almost identical in all conditions except 100 uM AcP, which may indicate that this compound inhibits FosX activity at high concentrations. However, AcP inhibition was not observed in ^{31}P-NMR experiments (data not shown), so the observation

may simply be due to an unhealthy cell culture. The liquid culture assays were performed twice and should be repeated to verify results.

From the MIC experiments, we conclude that the enzyme confers robust resistance in the biological context of *E. coli*, rivaling even the MIC values for *Listeria*, which thus far had been the most fosfomycin-resistant FosX.

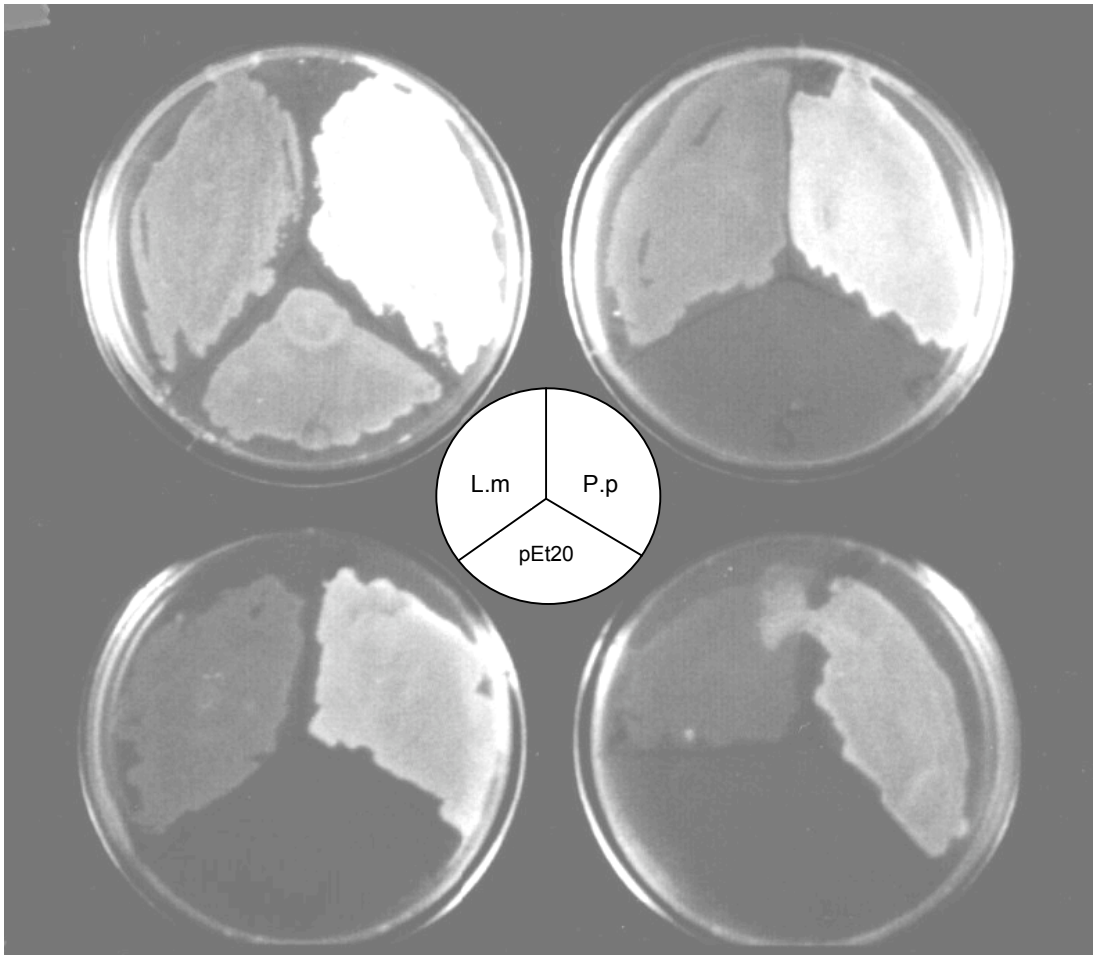

Figure 35. Growth of *E. coli* cells expressing *P. putida* and *L. monocytogenes* FosX as well as empty vector control. Clockwise from top left: 0 mg/mL, 5 mg/mL, 20 mg/mL, 10 mg/mL fosfomycin.

Table 13. Liquid culture growth in cells expressing *P. putida* FosX. Left: 4-hr growth with different fosfomycin concentrations. Right: 4- and 7-hr growth in 20 mg/mL fosfomycin with different inhibitor concentrations.

mg/mL fosfomycin	OD_{600} (4 hrs)
0	2.3
0.05	2.08
0.1	1.82
0.5	1.98
2	1.39
10	1.52

[inhibitor]	OD_{600} (4 hrs)	OD_{600} (7 hrs)
none	0.32	1.1
10uM Pf	0.23	1.15
50uM Pf	0.21	1.09
100uM Pf	0.26	1.07
10uM AcP	0.24	1.1
50uM AcP	0.25	1.05
100uM AcP	0.08	0.8

Catalytic Properties Deduced from ^{31}P-NMR Spectroscopy

Interestingly, NMR results do not corroborate the *in vivo* resistance that we observe in the previous section; in fact, the enzyme appears to be a very poor catalyst. The enzyme was incubated with a variety of divalent metals to determine with which it exhibits the highest catalytic activity. FosX enzymes characterized to date have displayed the highest turnover rates with either Mn^{2+} or Cu^{2+}, and preferences for the remaining metals vary depending on the enzyme (unpublished observations). Optimum reaction times were determined experimentally and are defined as the period during which 10-15% product conversion is observed; 19 hours reaction time are required to observe this product turnover, which implies that this enzyme performs the FosX reaction at an extremely low rate. The metal preference of the *Pseudomonas* FosX is $Mn^{2+} > Ni^{2+} > Mg^{2+} > Cu^{2+} > Ca^{2+}$ (Figure 36). No activity is observed for Co^{2+}, Zn^{2+}, Fe^{2+}, or the no metal control (data not shown). The only metals with which we observe the proper turnover to allow rate determination at pH 7.5 are Mn^{2+}, Ni^{2+}, and Mg^{2+}; the k_{cat} values are 0.024 s^{-1}, 0.015 s^{-1}, and 0.010 s^{-1}, respectively.

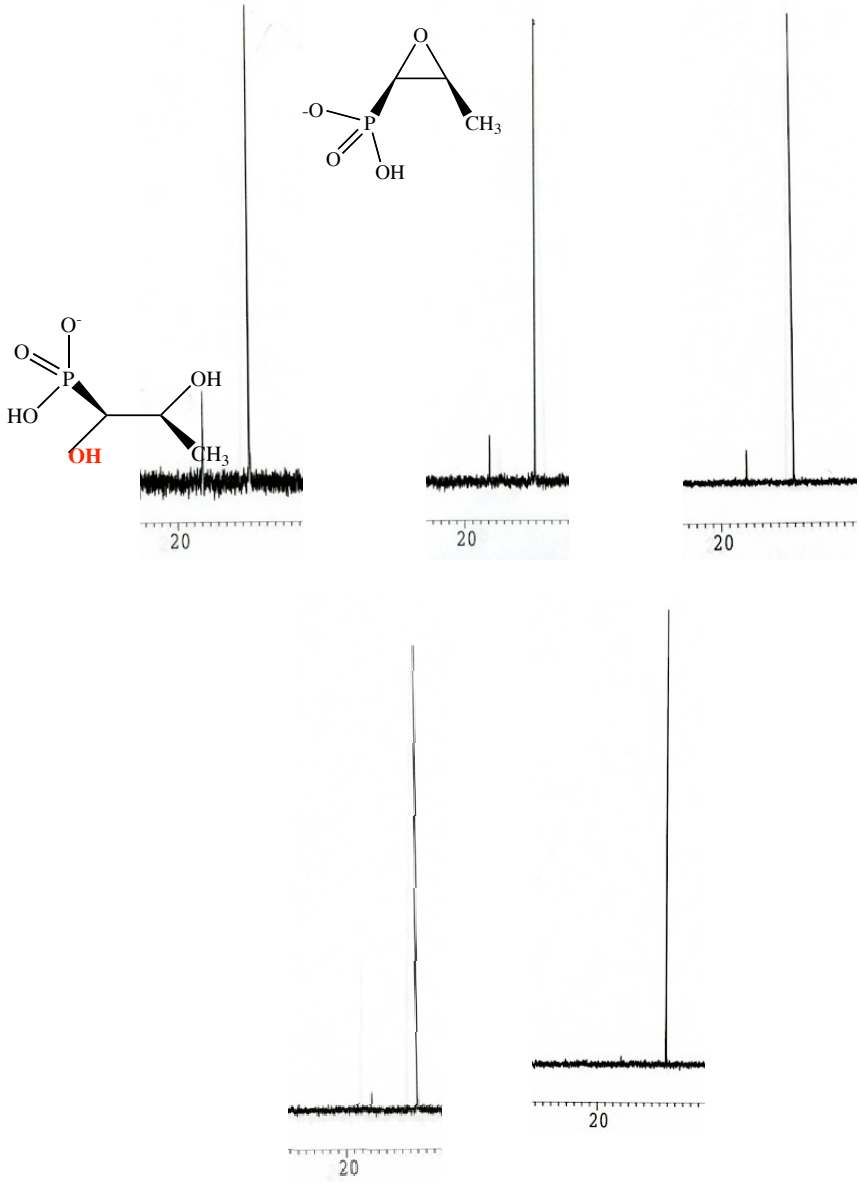

Figure 36. ^{31}P-NMR spectra showing metal preferences of *Pseudomonas putida* FosX reaction at pH 7.5, 19-hour incubation. In preference order from left to right, top to bottom: Mn^{2+}, Ni^{2+}, Mg^{2+}, Cu^{2+}, Ca^{2+}.

However, a puzzling phenomenon occurs when the reactions are carried out at pH 9.5--the rates dramatically increase. Figure 37 shows the pH profile of FosX reactions incubated for 19 hours. To determine turnover rates, all conditions were kept the same except incubation times were reduced to 2 hours. Significant rate improvement is observed only for the top two preferred metals Mn^{2+} (15-fold increase to 0.35 s^{-1}) and Ni^{2+} (5-fold

increase to 0.076 s^{-1}). To determine whether this high optimum pH is characteristic of the *Listeria* enzyme as well, NMR experiments were carried out according to the same procedure. Turnover at pH 9.5 is improved only 1.05-fold over pH 7.5, not an appreciable difference (data not shown).

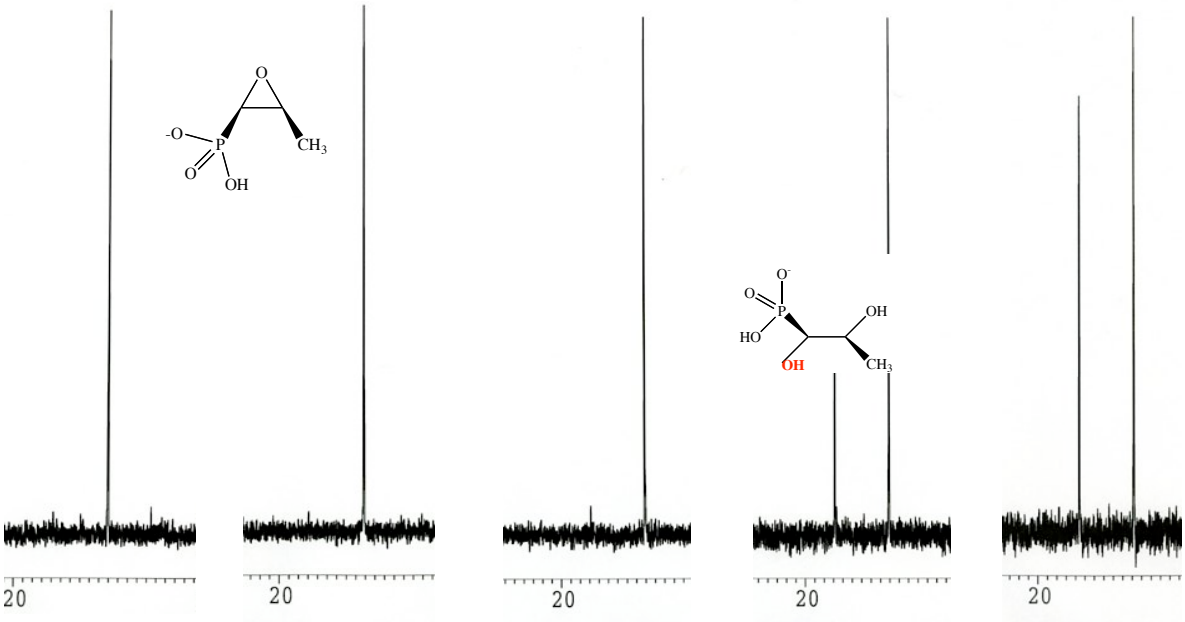

Figure 37. ^{31}P-NMR spectra showing pH profile of *Pseudomonas putida* FosX reaction with 19-hour incubation. From left: pH 5.5, 6.5, 7.5, 8.5, and 9.5.

The enzyme does not show any catalytic activity whatsoever when GSH or L-cys are used as substrates for the FosA and FosB reactions, respectively, nor is the FosX activity affected by adding FosA inhibitors Pf or AcP (Figure 38). These reactions were tested at variable substrate and inhibitor concentrations to guard against the possibility of substrate inhibition.

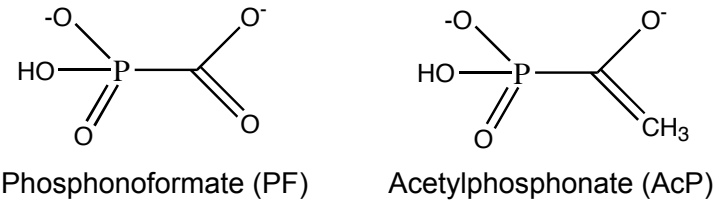

Figure 38. Structures of FosA inhibitors Phosphonoformate (PF) and Acetylphosphonate (AcP).

Discussion

Clearly, we must resolve the discrepancy between the *in vitro* NMR results, showing that the enzyme has very low catalytic activity, and the *in vivo* results, showing that the enzyme confers robust resistance to fosfomycin when expressed in *E. coli.* The NMR data shows that FosX activity is nominal, and since the only peaks on the spectra are fosfomycin and its hydrolyzed product, this implies that the only alteration of the fosfomycin molecule is conversion to diol. At least when the only reactants are enzyme, fosfomycin, and metal cofactor, the only enzymatic reaction is hydrolysis.

However, we observe a very different outcome when the enzyme is overexpressed in *E. coli*; the robust resistance signifies that the bacteria are somehow consuming and inactivating fosfomycin. From these observations, we must conclude that this enzyme is capable of an alternate activity that is undetectable by ^{31}P-NMR. Several examples in the literature may help to clarify this incongruity.

The related species *Pseudomonas fluorescens* encodes a phosphonoacetate hydrolase gene (*phnA*) capable of cleaving the carbon-phosphorus bond of substrates phosphonoacetate (PA) and 2-phosphonopropionate (2PP) (Figure 39). Interestingly, analysis revealed that the substrate is necessary to induce the gene required for substrate utilization. When the gene was subcloned into *E. coli* and *P. putida* host strains, hydrolase activity was not detected unless a second gene *phnR*, located upstream of *phnA* in *P. fluorescens*, was also subcloned. In this way, *phnR* acts as a transcriptional regulator. This activity represents the only known example of a C-P cleavage enzyme not under control of the *pho* operon (46).

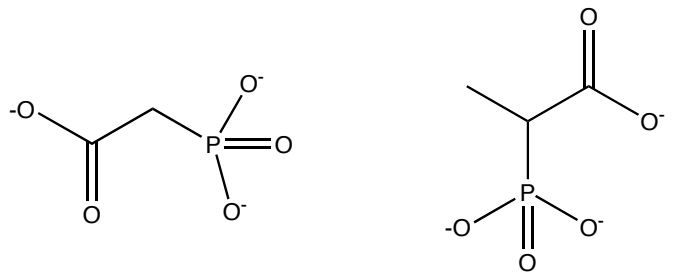

Phosphonoacetate (PA) 2-Phosphonopropionate (2PP)

Figure 39. Structures of potential FosX substrates Phosphonoacetate (PA) and 2-Phosphonopropionate (2PP).

The novel properties of this phosphate hydrolase gene lend some insight into the hydrolase enzyme found in *P. putida*. Perhaps on the *P. putida* integron encoding FosX, one of the uncharacterized ORFs acts as a transcriptional regulator in much the same way as the above example; if so, the enzyme has very little or no activity without the second gene. Without the additional gene product being present in our NMR experiments, the FosX is only slight. However, when the gene encoding the *P. putida* FosX is expressed in *E. coli*, perhaps a similar regulator to the one in *P. putida* is present in the *E. coli* genome, serves as an inducer, and thereby allows the enzyme to confer resistance. In other words, the gene's activity can only be "turned on" in the cell but cannot be simulated in *in vitro* assays. To test this possibility, the other enzymes encoded on the *P. putida* integron can be engineered into the plasmid containing FosX and activity then assessed. Substrates PA and 2PP, whose structures bear similarity to fosfomycin, would also be worthwhile to test as potential FosX substrates.

A related explanation for these peculiar results could be that the unknown product is somehow utilized by another enzyme *in vivo* which allows resistance to occur in *E. coli* cells but not in the NMR experiment. The above example describes a reaction in which the C-P bond is cleaved, a mechanism different from the FosX ring-opening reaction that cleaves a C-O bond. Perhaps the *P. putida* enzyme also catalyzes a C-P bond breakage, and the resulting reaction product can then act as a substrate for a second enzyme—possibly a transporter protein that shuttles the molecule outside the cell. Immunoprecipitation assays can be used to determine if a second protein interacts with the FosX *in vivo.* To test for C-P bond breakage activity, a procedure can be used to measure inorganic phosphate release.

Alternatively, maybe the reaction product is used as a nutrient phosphate source. Several years ago, a paper illustrated that *P. putida* cultures grew when incubated separately with phosphonates 2-aminoethylphosphonic acid (AEP) and methylphosphonic acid (MPA) (Figure 40) (47). Maybe the *P. putida* enzyme somehow generates one of these products and then uses it for nutrition. This seems likely, because another paper reported robust *P. putida* growth when cultures were incubated with fosfomycin but without other phosphorus or carbon sources (48). Of course, if this scenario is correct, there still must be a missing cofactor, because otherwise a free phosphate peak would appear on NMR spectra.

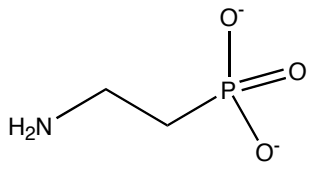

2-Aminoethylphosphonic acid (AEP)

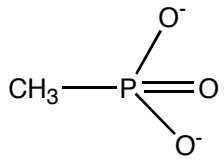

Methylphosphonic acid (MP)

Figure 40. Structures of potential FosX substrates 2-Aminoethylphosphonic acid (AEP) and Methylphosphonic acid (MP).

The possibility still remains that our *in vitro* assay simply does not contain the metal cofactor necessary for optimum activity. Future experiments could include metals with charges of +1, +3, or +4. Crystallography structures in the presence of a catalytically relevant metal would greatly aid our understanding of this enzyme, because they may indicate what residues are responsible for the heightened catalytic activity at increasingly basic pH. But considering these many potential reasons for the lack of NMR activity, the best way to determine the role of this enzyme is still to study it in its native context, the organism *Pseudomonas putida.* This species is known for its incredible ability to deactivate countless compounds in the soil, so it makes sense that it would develop a mechanism to degrade and utilize fosfomycin to its advantage. Assuring that strict safety precautions are followed, perhaps the laboratory can one day determine how this enzyme confers resistance by investigating the bacterium directly.

APPENDIX

LISTERIA MONOCYTOGENES PEPTIDE MAPS GENERATED BY PROTEOLYTIC CLEAVAGE WITH PEPSIN, *ASPERGILLUS SAITOI* PROTEASE XIII, AND *RHIZOPUS* PROTEASE XVIII

PEPSIN

85% Coverage

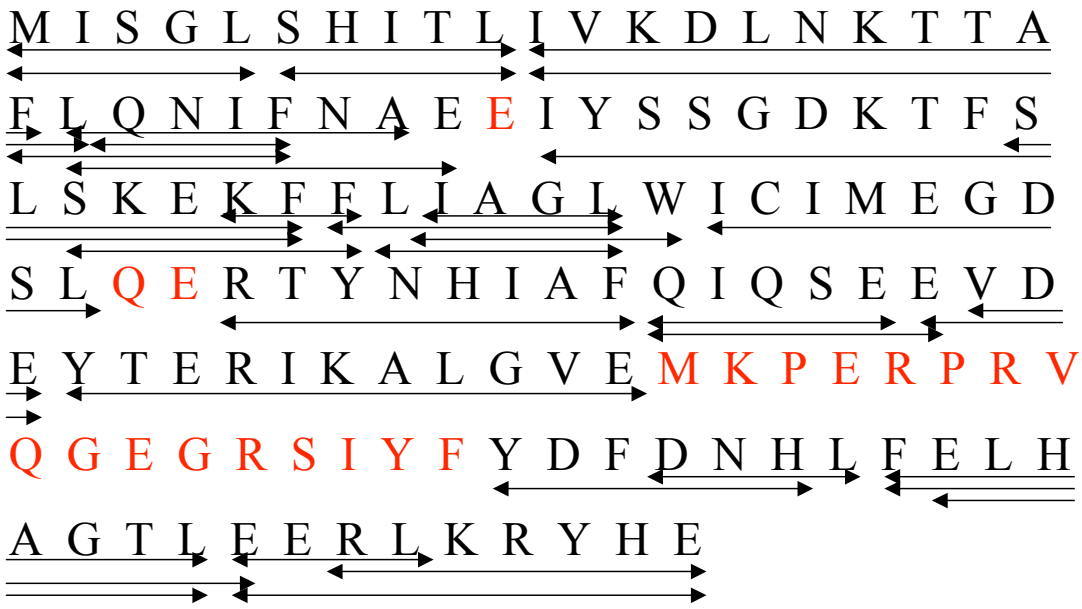

***ASPERGILLUS SAITOI* PROTEASE XIII**

78% Coverage

***RHIZOPUS* PROTEASE XVIII**

69% Coverage

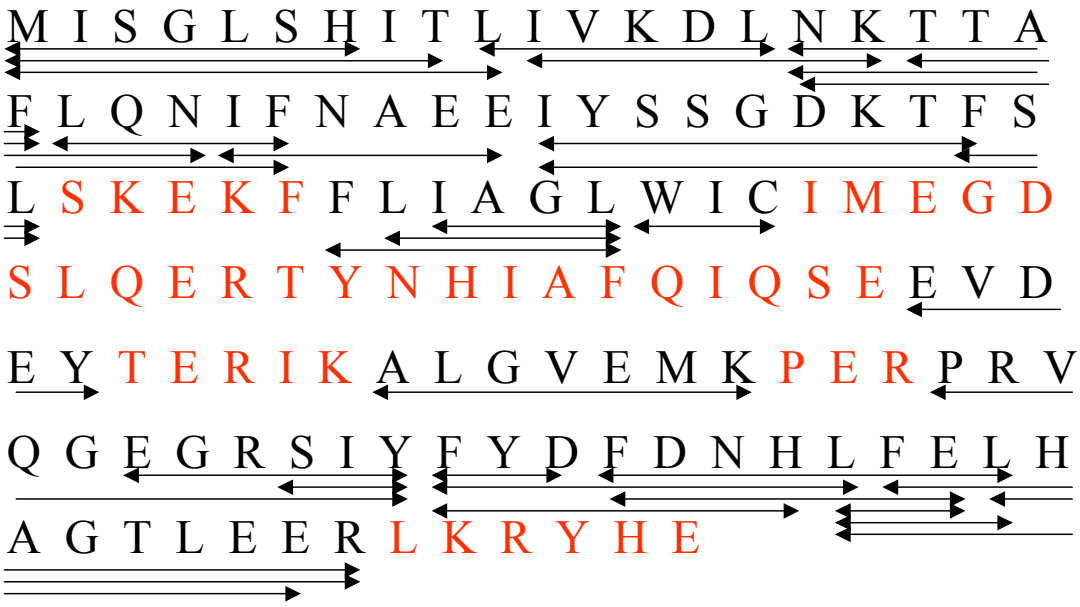

ALL HYDROGEN/DEUTERIUM EXCHANGE MASS SPECTROMETRY PLOTS, SHOWN INDIVIDUALLY WITH GOODNESS OF FIT DATA

Black: native

Red: Mn^{2+}-bound

Blue: Co^{2+}-bound

Green: Zn^{2+}-bound

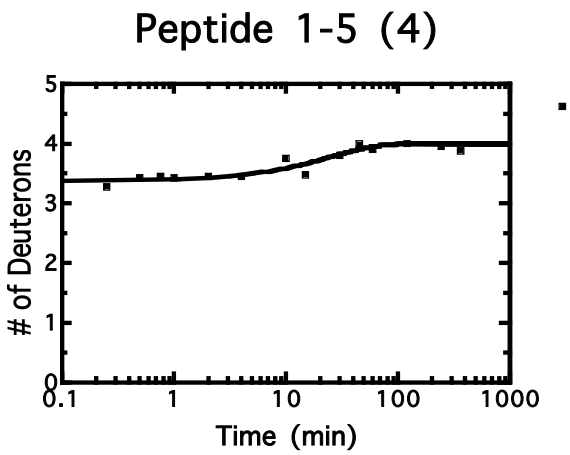

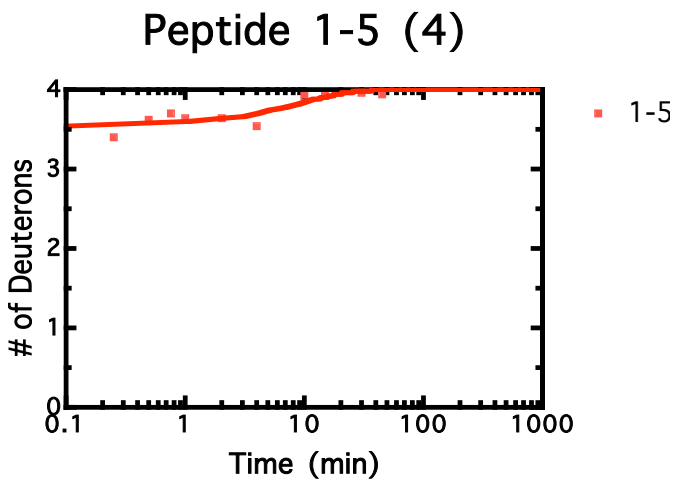

	1-5 (4)
single exponential	
Best-fit values	
A1	0.6204
K1	0.04014
Std. Error	
A1	0.04247
K1	0.009975
95% Confidence Intervals	
A1	0.5278 to 0.7129
K1	0.01841 to 0.06188
Goodness of Fit	
Degrees of Freedom	12
R squared	0.8800
Absolute Sum of Squares	0.1050
Sy.x	0.09355
Constraints	
A1	A1 > 0.0
K1	K1 > 0.0
Data	
Number of X values	14
Number of Y replicates	1

	1-5 (4)
single exponential	
Best-fit values	
A1	0.4599
K1	0.1051
Std. Error	
A1	0.05658
K1	0.04557
95% Confidence Intervals	
A1	0.3366 to 0.5831
K1	0.005794 to 0.2044
Goodness of Fit	
Degrees of Freedom	12
R squared	0.8241
Absolute Sum of Squares	0.1275
Sy.x	0.1031
Constraints	
A1	A1 > 0.0
K1	K1 > 0.0
Data	
Number of X values	14
Number of Y replicates	1

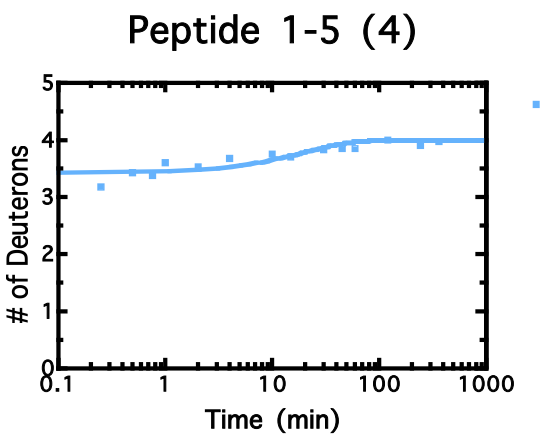

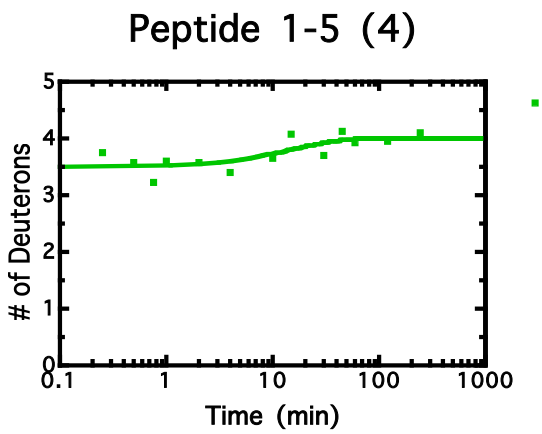

	1-5 (4)
single exponential	
Best-fit values	
A1	0.5700
K1	0.04756
Std. Error	
A1	0.05651
K1	0.01718
95% Confidence Intervals	
A1	0.4469 to 0.6931
K1	0.01013 to 0.08498
Goodness of Fit	
Degrees of Freedom	12
R squared	0.7704
Absolute Sum of Squares	0.1755
Sy.x	0.1209
Constraints	
A1	A1 > 0.0
K1	K1 > 0.0
Data	
Number of X values	14
Number of Y replicates	1

	1-5 (4)
single exponential	
Best-fit values	
A1	0.4999
K1	0.06141
Std. Error	
A1	0.08777
K1	0.03912
95% Confidence Intervals	
A1	0.3067 to 0.6930
K1	0.0 to 0.1475
Goodness of Fit	
Degrees of Freedom	11
R squared	0.6094
Absolute Sum of Squares	0.3539
Sy.x	0.1794
Constraints	
A1	A1 > 0.0
K1	K1 > 0.0
Data	
Number of X values	13
Number of Y replicates	1

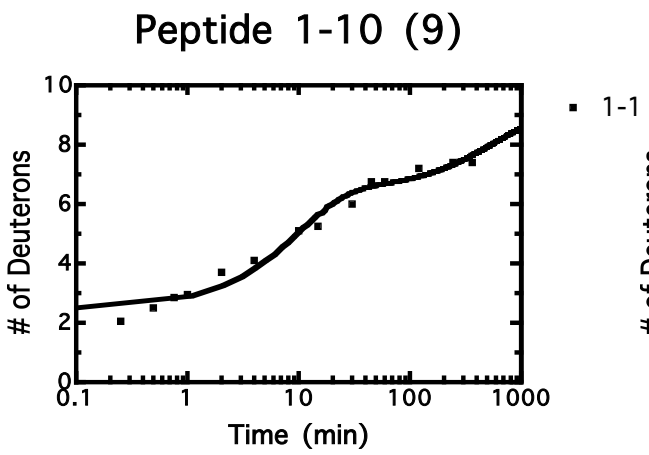

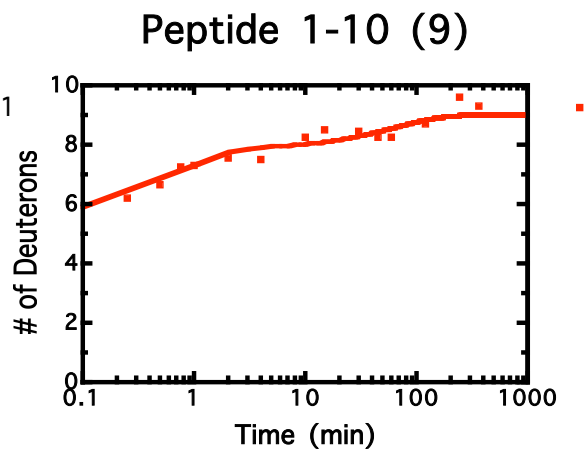

	1-10 (9)
double exponential	
Best-fit values	
A1	3.975
K1	0.1007
A2	2.562
K2	0.001744
Std. Error	
A1	0.3145
K1	0.02263
A2	0.2934
K2	0.0007400
95% Confidence Intervals	
A1	3.275 to 4.676
K1	0.05024 to 0.1511
A2	1.909 to 3.216
K2	9.4953e-005 to 0.003392
Goodness of Fit	
Degrees of Freedom	10
R squared	0.9776
Absolute Sum of Squares	1.128
Sy.x	0.3358

	1-10 (9)
double exponential	
Best-fit values	
A1	2.255
K1	1.371
A2	1.159
K2	0.01559
Std. Error	
A1	0.6904
K1	0.7481
A2	0.2620
K2	0.009004
95% Confidence Intervals	
A1	0.7171 to 3.793
K1	0.0 to 3.038
A2	0.5753 to 1.743
K2	0.0 to 0.03565
Goodness of Fit	
Degrees of Freedom	10
R squared	0.9058
Absolute Sum of Squares	1.134
Sy.x	0.3367

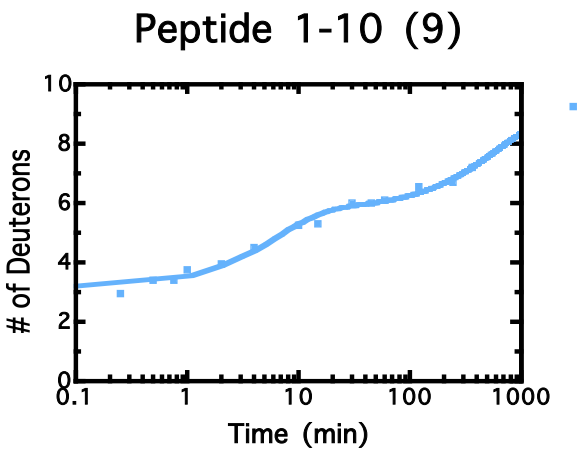

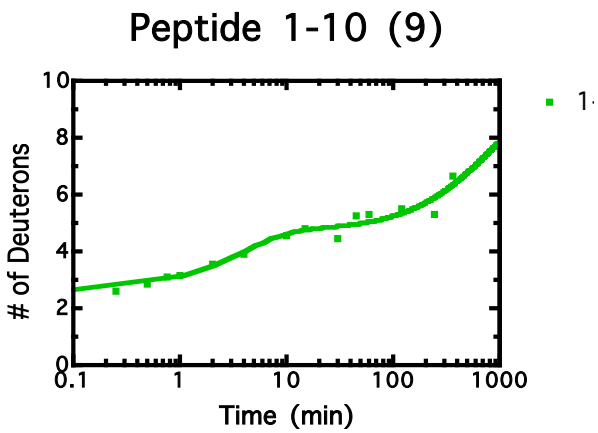

	1-10 (9)
double exponential	
Best-fit values	
A1	3.230
K1	0.001608
A2	2.625
K2	0.1577
Std. Error	
A1	0.1257
K1	0.0002729
A2	0.1488
K2	0.02825
95% Confidence Intervals	
A1	2.950 to 3.510
K1	0.001000 to 0.002
A2	2.293 to 2.956
K2	0.09477 to 0.2206
Goodness of Fit	
Degrees of Freedom	10
R squared	0.9881
Absolute Sum of Squares	0.3037
Sy.x	0.1743

	1-10 (9)
double exponential	
Best-fit values	
A1	4.290
K1	0.001315
A2	2.091
K2	0.2627
Std. Error	
A1	0.1745
K1	0.0002979
A2	0.2563
K2	0.1016
95% Confidence Intervals	
A1	3.901 to 4.678
K1	0.0006515 to 0.001979
A2	1.520 to 2.663
K2	0.03623 to 0.4891
Goodness of Fit	
Degrees of Freedom	10
R squared	0.9540
Absolute Sum of Squares	0.8455
Sy.x	0.2908

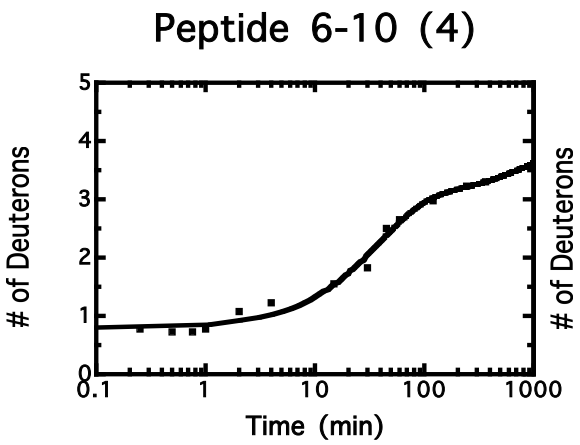

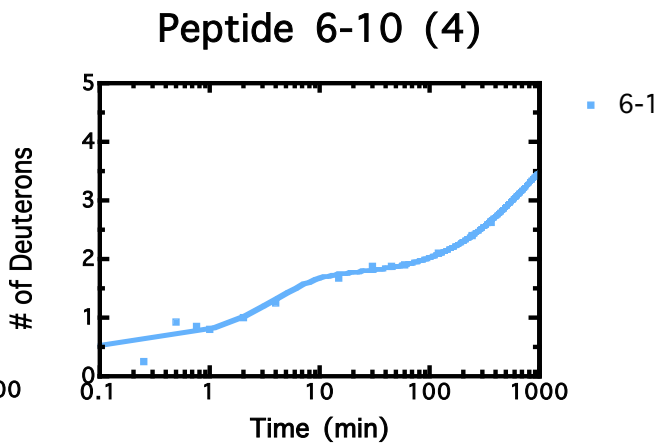

double exponential	
Best-fit values	
A1	2.214
K1	0.02670
A2	0.9959
K2	0.0009715
Std. Error	
A1	0.3289
K1	0.006473
A2	0.3360
K2	0.001262
95% Confidence Intervals	
A1	1.470 to 2.958
K1	0.01205 to 0.04134
A2	0.2360 to 1.756
K2	0.0 to 0.003826
Goodness of Fit	
Degrees of Freedom	9
R squared	0.9870
Absolute Sum of Squares	0.1590
Sy.x	0.1329

	6-10 (4)
double exponential	
Best-fit values	
A1	1.218
K1	0.2769
A2	2.290
K2	0.001471
Std. Error	
A1	0.1489
K1	0.1001
A2	0.09683
K2	0.0003128
95% Confidence Intervals	
A1	0.8814 to 1.555
K1	0.05040 to 0.5033
A2	2.071 to 2.509
K2	0.0007631 to 0.002178
Goodness of Fit	
Degrees of Freedom	9
R squared	0.9644
Absolute Sum of Squares	0.2156
Sy.x	0.1548

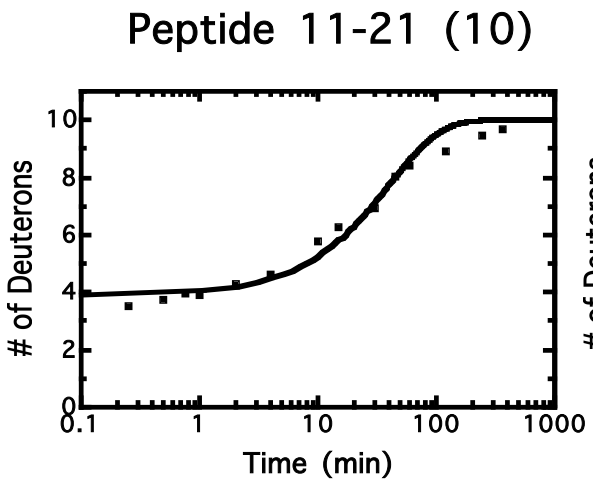

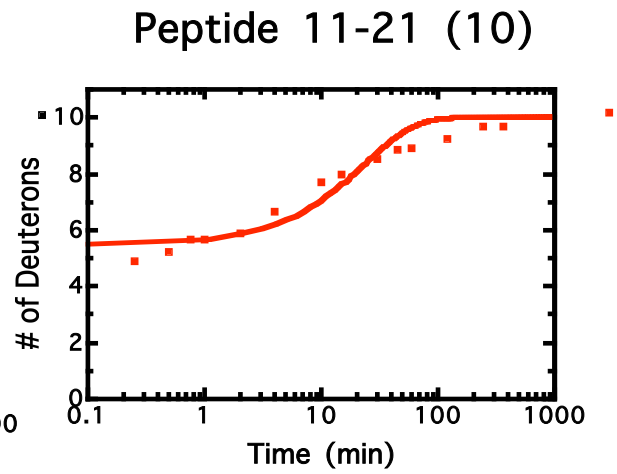

	11-21 (10)
single exponential	
Best-fit values	
A1	6.106
K1	0.02486
Std. Error	
A1	0.1662
K1	0.002520
95% Confidence Intervals	
A1	5.744 to 6.468
K1	0.01936 to 0.03035
Goodness of Fit	
Degrees of Freedom	12
R squared	0.9735
Absolute Sum of Squares	1.835
Sy.x	0.3910
Constraints	
A1	A1 > 0.0
K1	K1 > 0.0
Data	
Number of X values	14
Number of Y replicates	1

	11-21 (10)
single exponential	
Best-fit values	
A1	4.525
K1	0.04262
Std. Error	
A1	0.2259
K1	0.007730
95% Confidence Intervals	
A1	4.033 to 5.017
K1	0.02578 to 0.05946
Goodness of Fit	
Degrees of Freedom	12
R squared	0.9264
Absolute Sum of Squares	2.913
Sy.x	0.4927
Constraints	
A1	A1 > 0.0
K1	K1 > 0.0
Data	
Number of X values	14
Number of Y replicates	1

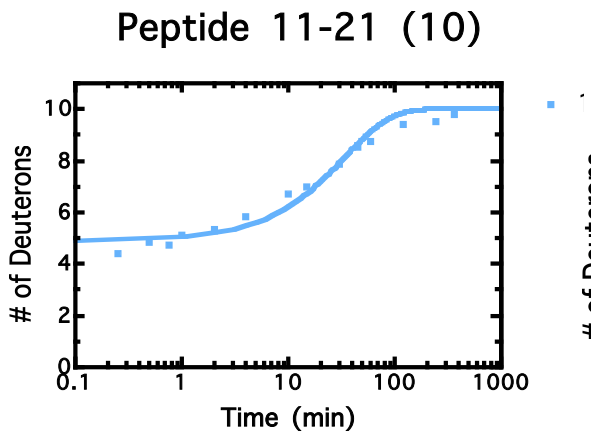

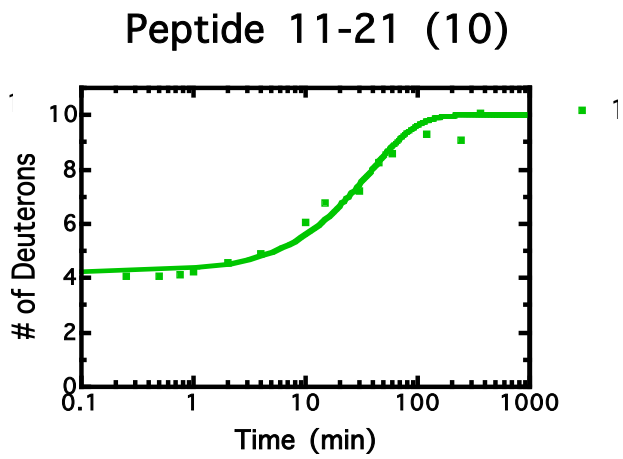

	11-21 (10)
single exponential	
Best-fit values	
A1	5.105
K1	0.02961
Std. Error	
A1	0.1511
K1	0.003212
95% Confidence Intervals	
A1	4.776 to 5.434
K1	0.02261 to 0.03660
Goodness of Fit	
Degrees of Freedom	12
R squared	0.9714
Absolute Sum of Squares	1.450
Sy.x	0.3477
Constraints	
A1	A1 > 0.0
K1	K1 > 0.0
Data	
Number of X values	14
Number of Y replicates	1

	11-21 (10)
single exponential	
Best-fit values	
A1	5.787
K1	0.02717
Std. Error	
A1	0.1726
K1	0.002991
95% Confidence Intervals	
A1	5.411 to 6.164
K1	0.02066 to 0.03369
Goodness of Fit	
Degrees of Freedom	12
R squared	0.9698
Absolute Sum of Squares	1.936
Sy.x	0.4016
Constraints	
A1	A1 > 0.0
K1	K1 > 0.0
Data	
Number of X values	14
Number of Y replicates	1

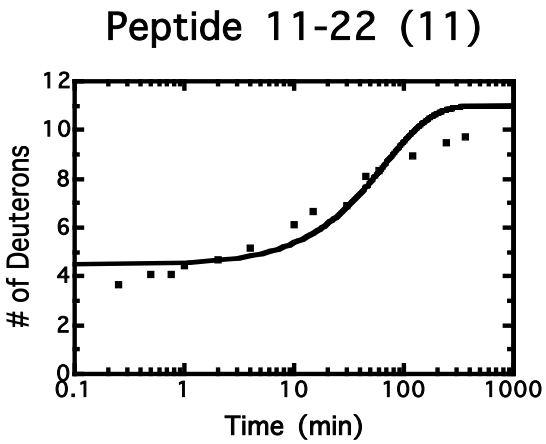

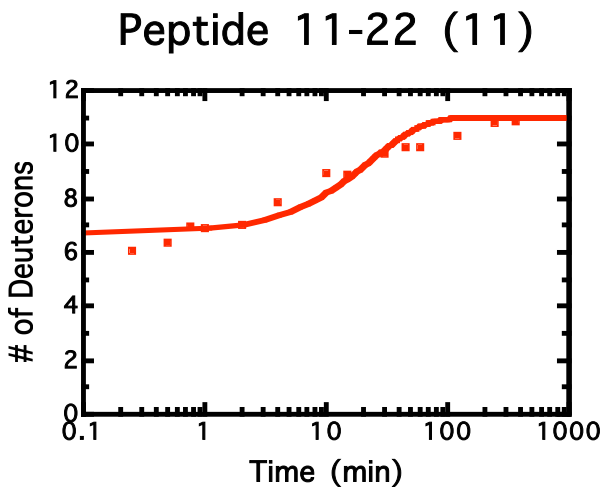

	11-22 (11)
single exponential	
Best-fit values	
A1	6.535
K1	0.01486
Std. Error	
A1	0.3074
K1	0.002843
95% Confidence Intervals	
A1	5.865 to 7.205
K1	0.008668 to 0.02106
Goodness of Fit	
Degrees of Freedom	12
R squared	0.8830
Absolute Sum of Squares	7.052
Sy.x	0.7666
Constraints	
A1	A1 > 0.0
K1	K1 > 0.0
Data	
Number of X values	14
Number of Y replicates	1

	11-22 (11)
single exponential	
Best-fit values	
A1	4.321
K1	0.04257
Std. Error	
A1	0.2199
K1	0.007872
95% Confidence Intervals	
A1	3.841 to 4.8
K1	0.02541 to
Goodness of Fit	
Degrees of Freedom	12
R squared	0.9268
Absolute Sum of Squares	2.762
Sy.x	0.4798
Constraints	
A1	A1 > 0.0
K1	K1 > 0.0
Data	
Number of X values	14
Number of Y replicates	1

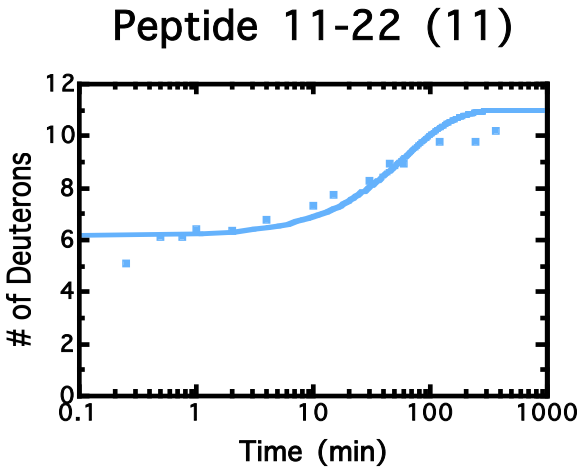

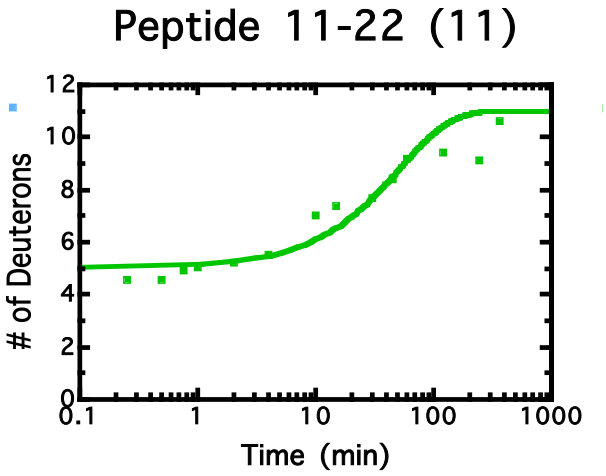

	11-22 (11)
single exponential	
Best-fit values	
A1	4.831
K1	0.01614
Std. Error	
A1	0.2376
K1	0.003173
95% Confidence Intervals	
A1	4.314 to 5.3
K1	0.009230 to
Goodness of Fit	
Degrees of Freedom	12
R squared	0.8804
Absolute Sum of Squares	4.137
Sy.x	0.5872
Constraints	
A1	A1 > 0.0
K1	K1 > 0.0
Data	
Number of X values	14
Number of Y replicates	1

	11-22 (11)
single exponential	
Best-fit values	
A1	5.965
K1	0.01927
Std. Error	
A1	0.3050
K1	0.003805
95% Confidence Intervals	
A1	5.300 to 6.6
K1	0.01098 to
Goodness of Fit	
Degrees of Freedom	12
R squared	0.8830
Absolute Sum of Squares	6.555
Sy.x	0.7391
Constraints	
A1	A1 > 0.0
K1	K1 > 0.0
Data	
Number of X values	14
Number of Y replicates	1

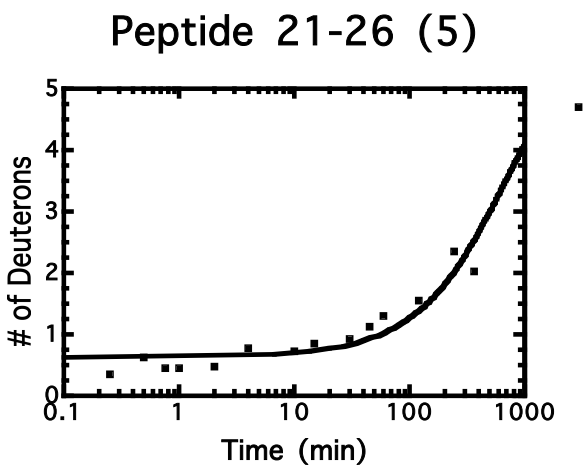

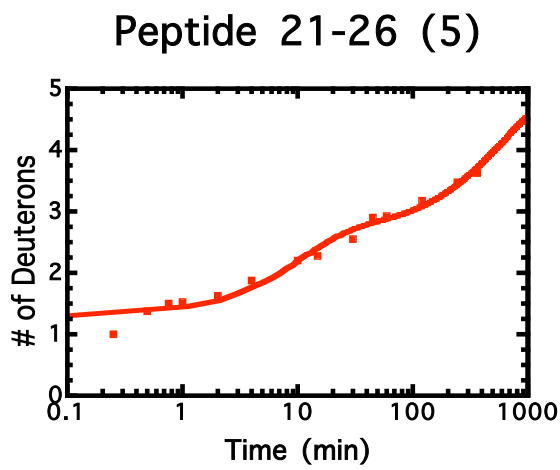

single exponential	
Best-fit values	
A1	4.368
K1	0.001566
Std. Error	
A1	0.07901
K1	0.0002149
95% Confidence Intervals	
A1	4.196 to 4.540
K1	0.001098 to 0.00
Goodness of Fit	
Degrees of Freedom	12
R squared	0.8542
Absolute Sum of Squares	0.7107
Sy.x	0.2434
Constraints	
A1	A1 > 0.0
K1	K1 > 0.0
Data	
Number of X values	14
Number of Y replicates	1
Total number of values	14
Number of missing values	0

	21-26 (5)
double exponential	
Best-fit values	
A1	1.365
K1	0.09737
A2	2.336
K2	0.001644
Std. Error	
A1	0.1385
K1	0.02806
A2	0.1296
K2	0.0003500
95% Confidence Intervals	
A1	1.057 to 1.674
K1	0.03485 to 0.159
A2	2.047 to 2.625
K2	0.0008642 to 0.0
Goodness of Fit	
Degrees of Freedom	10
R squared	0.9761
Absolute Sum of Squares	0.2174
Sy.x	0.1475

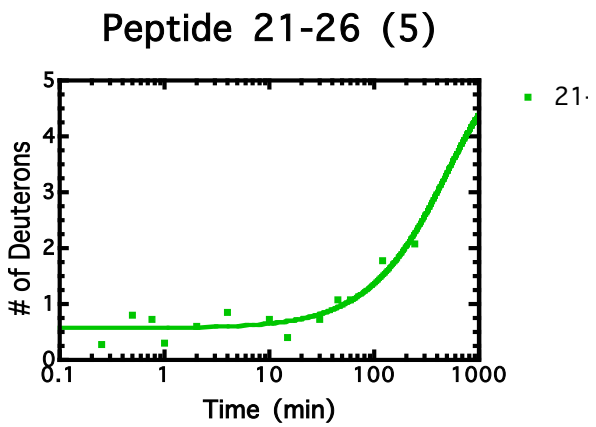

	21-26 (5)
single exponential	
Best-fit values	
A1	4.437
K1	0.001990
Std. Error	
A1	0.07297
K1	0.0002894
95% Confidence Intervals	
A1	4.277 to 4.598
K1	0.001353 to 0.002627
Goodness of Fit	
Degrees of Freedom	11
R squared	0.8491
Absolute Sum of Squares	0.5133
Sy.x	0.2160
Constraints	
A1	A1 > 0.0
K1	K1 > 0.0
Data	
Number of X values	13
Number of Y replicates	1

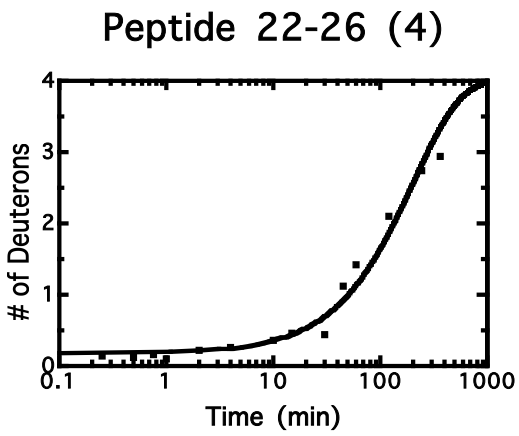

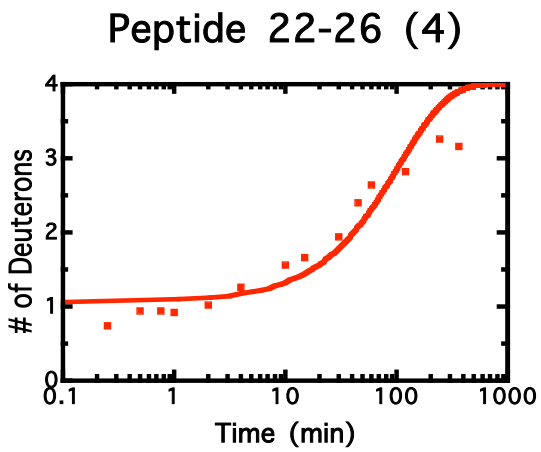

	22-26 (4)
single exponential	
Best-fit values	
A1	3.826
K1	0.004834
Std. Error	
A1	0.06483
K1	0.0003960
95% Confidence Intervals	
A1	3.684 to 3.967
K1	0.003971 to 0.0056
Goodness of Fit	
Degrees of Freedom	12
R squared	0.9689
Absolute Sum of Squares	0.4126
Sy.x	0.1854
Constraints	
A1	A1 > 0.0
K1	K1 > 0.0
Data	
Number of X values	14
Number of Y replicates	1

	22-26 (4)
single exponential	
Best-fit values	
A1	2.940
K1	0.009347
Std. Error	
A1	0.1242
K1	0.001750
95% Confidence Intervals	
A1	2.669 to 3.2
K1	0.005535 to
Goodness of Fit	
Degrees of Freedom	12
R squared	0.8771
Absolute Sum of Squares	1.287
Sy.x	0.3275
Constraints	
A1	A1 > 0.0
K1	K1 > 0.0
Data	
Number of X values	14
Number of Y replicates	1

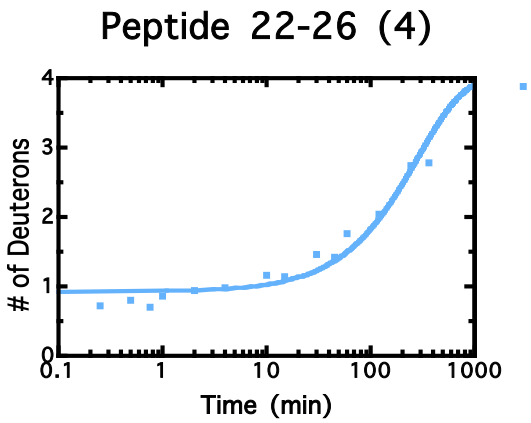

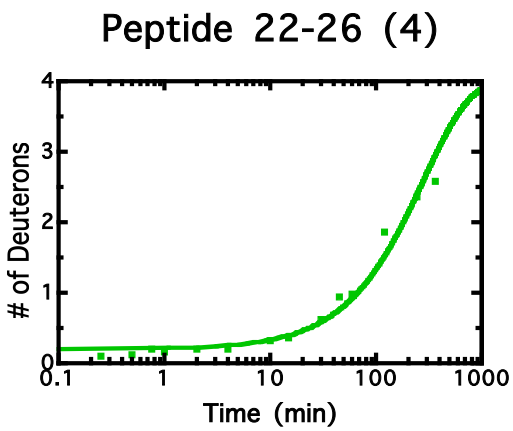

	22-26 (4)
single exponential	
Best-fit values	
A1	3.077
K1	0.003466
Std. Error	
A1	0.06023
K1	0.0003534
95% Confidence Intervals	
A1	2.946 to 3.2
K1	0.002696 to
Goodness of Fit	
Degrees of Freedom	12
R squared	0.9401
Absolute Sum of Squares	0.3785
Sy.x	0.1776
Constraints	
A1	A1 > 0.0
K1	K1 > 0.0
Data	
Number of X values	14
Number of Y replicates	1

	22-26 (4)
single exponential	
Best-fit values	
A1	3.801
K1	0.003537
Std. Error	
A1	0.05519
K1	0.0002660
95% Confidence Intervals	
A1	3.681 to 3.9
K1	0.002957 to
Goodness of Fit	
Degrees of Freedom	12
R squared	0.9672
Absolute Sum of Squares	0.3169
Sy.x	0.1625
Constraints	
A1	A1 > 0.0
K1	K1 > 0.0
Data	
Number of X values	14
Number of Y replicates	1

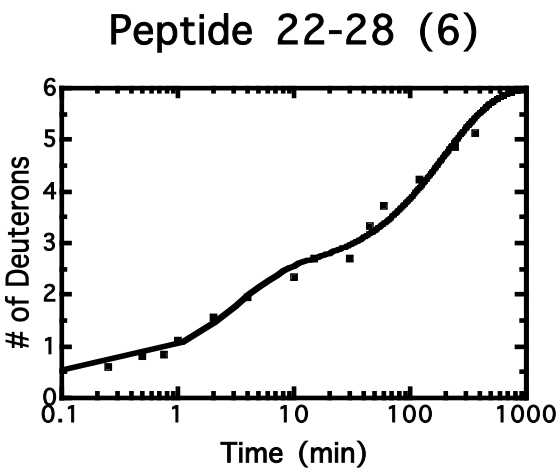

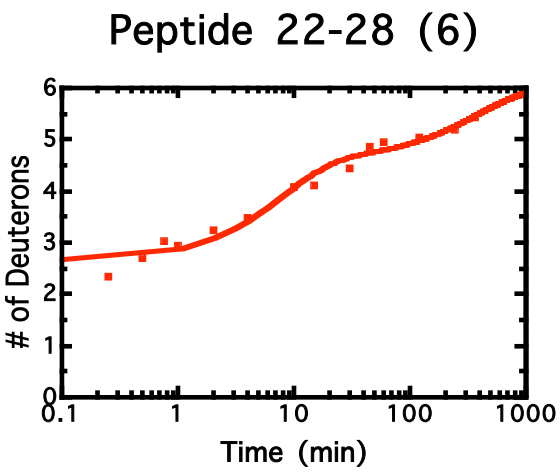

double exponential	
Best-fit values	
A1	1.976
K1	0.3145
A2	3.533
K2	0.005012
Std. Error	
A1	0.1934
K1	0.09070
A2	0.1439
K2	0.0005765
95% Confidence Intervals	
A1	1.545 to 2.407
K1	0.1125 to 0.5166
A2	3.212 to 3.854
K2	0.003727 to 0.006296
Goodness of Fit	
Degrees of Freedom	10
R squared	0.9875
Absolute Sum of Squares	0.3770
Sy.x	0.1942

	22-28 (6)
double exponential	
Best-fit values	
A1	1.949
K1	0.1220
A2	1.408
K2	0.002619
Std. Error	
A1	0.1813
K1	0.03284
A2	0.1674
K2	0.0009284
95% Confidence Intervals	
A1	1.545 to 2.3
K1	0.04881 to
A2	1.035 to 1.7
K2	0.0005503
Goodness of Fit	
Degrees of Freedom	10
R squared	0.9731
Absolute Sum of Squares	0.3701
Sy.x	0.1924

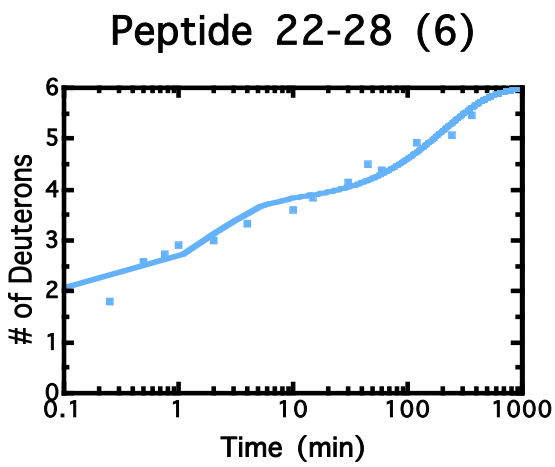

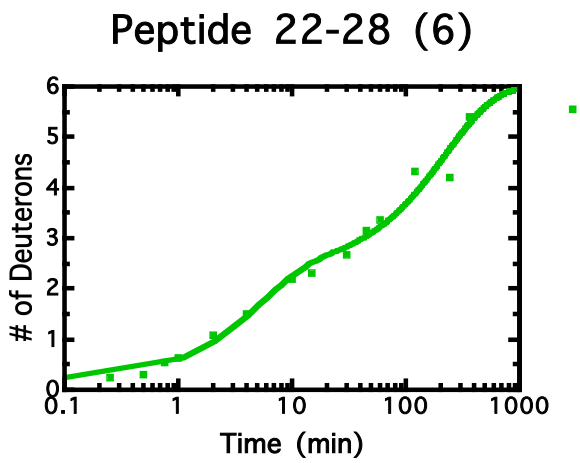

	22-28 (6)
double exponential	
Best-fit values	
A1	1.748
K1	0.4871
A2	2.258
K2	0.004831
Std. Error	
A1	0.2709
K1	0.1957
A2	0.1581
K2	0.001040
95% Confidence Intervals	
A1	1.144 to 2.3
K1	0.05114 to
A2	1.906 to 2.6
K2	0.002513 to
Goodness of Fit	
Degrees of Freedom	10
R squared	0.9604
Absolute Sum of Squares	0.5883
Sy.x	0.2425

	22-28 (6)
double exponential	
Best-fit values	
A1	3.609
K1	0.004404
A2	2.208
K2	0.2002
Std. Error	
A1	0.2145
K1	0.0006880
A2	0.2425
K2	0.06775
95% Confidence Intervals	
A1	3.131 to 4.0
K1	0.002871 to
A2	1.668 to 2.7
K2	0.04921 to
Goodness of Fit	
Degrees of Freedom	10
R squared	0.9819
Absolute Sum of Squares	0.6442
Sy.x	0.2538

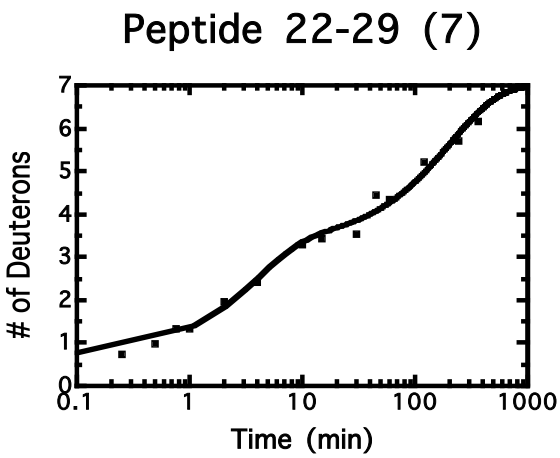

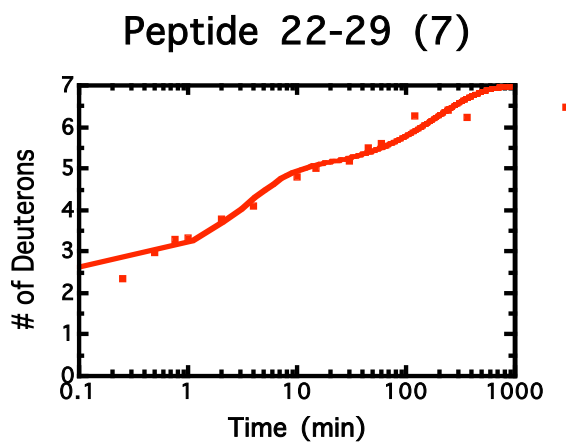

	22-29 (7)
double exponential	
Best-fit values	
A1	2.668
K1	0.2642
A2	3.642
K2	0.004830
Std. Error	
A1	0.2081
K1	0.06305
A2	0.1676
K2	0.0006090
95% Confidence Intervals	
A1	2.204 to 3.1
K1	0.1237 to 0
A2	3.268 to 4.(
K2	0.003473 tc
Goodness of Fit	
Degrees of Freedom	10
R squared	0.9891
Absolute Sum of Squares	0.4615
Sy.x	0.2148
Constraints	
A1	A1 > 0.0
K1	K1 > 0.0
A2	A2 > 0.0
K2	K2 > 0.0
Data	

	22-29 (7)
double exponential	
Best-fit values	
A1	2.403
K1	0.2988
A2	2.042
K2	0.005147
Std. Error	
A1	0.2603
K1	0.09628
A2	0.2004
K2	0.001396
95% Confidence Intervals	
A1	1.823 to 2.9
K1	0.08426 to
A2	1.596 to 2.4
K2	0.002036 tc
Goodness of Fit	
Degrees of Freedom	10
R squared	0.9700
Absolute Sum of Squares	0.6897
Sy.x	0.2626
Constraints	
A1	A1 > 0.0
K1	K1 > 0.0
A2	A2 > 0.0
K2	K2 > 0.0
Data	

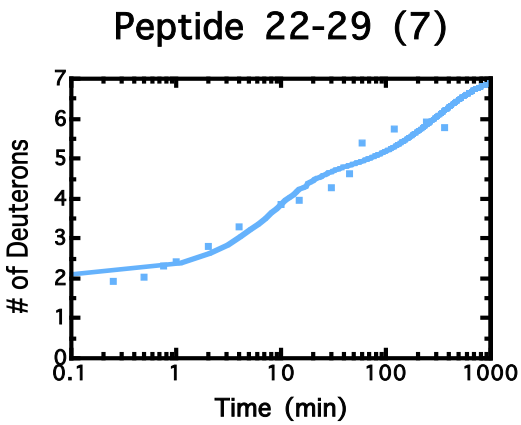

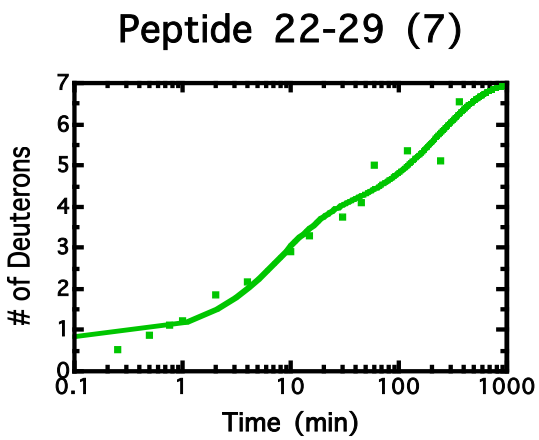

	22-29 (7)
double exponential	
Best-fit values	
A1	2.456
K1	0.1175
A2	2.480
K2	0.003126
Std. Error	
A1	0.3186
K1	0.04287
A2	0.3003
K2	0.001012
95% Confidence Intervals	
A1	1.746 to 3.1
K1	0.02200 to
A2	1.811 to 3.1
K2	0.0008706
Goodness of Fit	
Degrees of Freedom	10
R squared	0.9623
Absolute Sum of Squares	1.040
Sy.x	0.3226
Constraints	
A1	A1 > 0.0
K1	K1 > 0.0
A2	A2 > 0.0
K2	K2 > 0.0
Data	

	22-29 (7)
double exponential	
Best-fit values	
A1	2.921
K1	0.1259
A2	3.285
K2	0.004088
Std. Error	
A1	0.3967
K1	0.04694
A2	0.3800
K2	0.001133
95% Confidence Intervals	
A1	2.037 to 3.8
K1	0.02128 to
A2	2.438 to 4.1
K2	0.001565 to
Goodness of Fit	
Degrees of Freedom	10
R squared	0.9693
Absolute Sum of Squares	1.450
Sy.x	0.3807
Constraints	
A1	A1 > 0.0
K1	K1 > 0.0
A2	A2 > 0.0
K2	K2 > 0.0
Data	

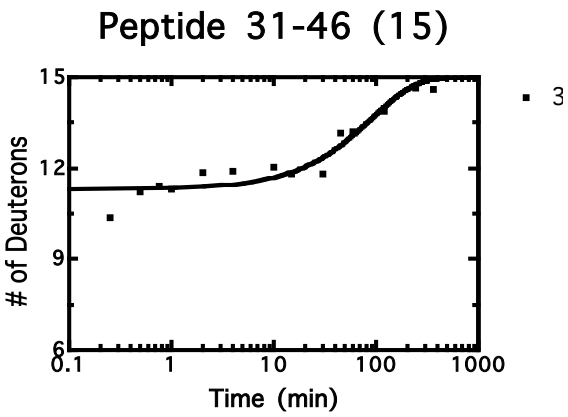

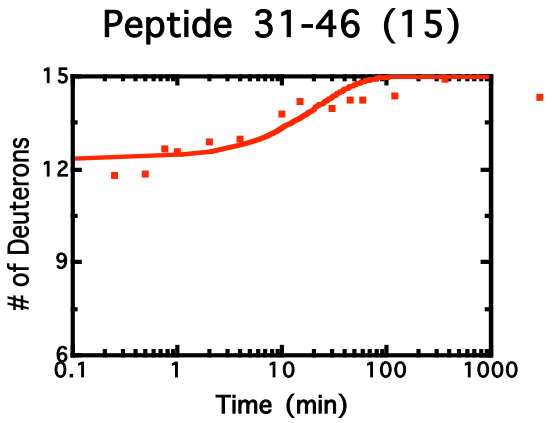

	31-46 (15)
single exponential	
Best-fit values	
A1	3.697
K1	0.01096
Std. Error	
A1	0.1593
K1	0.002037
95% Confidence Intervals	
A1	3.350 to 4.044
K1	0.006521 to 0.01540
Goodness of Fit	
Degrees of Freedom	12
R squared	0.9084
Absolute Sum of Squares	2.034
Sy.x	0.4117
Constraints	
A1	A1 > 0.0
K1	K1 > 0.0
Data	
Number of X values	14
Number of Y replicates	1

	31-46 (15)
single exponential	
Best-fit values	
A1	2.652
K1	0.04569
Std. Error	
A1	0.2235
K1	0.01403
95% Confidence Intervals	
A1	2.165 to 3.139
K1	0.01512 to 0.07626
Goodness of Fit	
Degrees of Freedom	12
R squared	0.8351
Absolute Sum of Squares	2.782
Sy.x	0.4815
Constraints	
A1	A1 > 0.0
K1	K1 > 0.0
Data	
Number of X values	14
Number of Y replicates	1

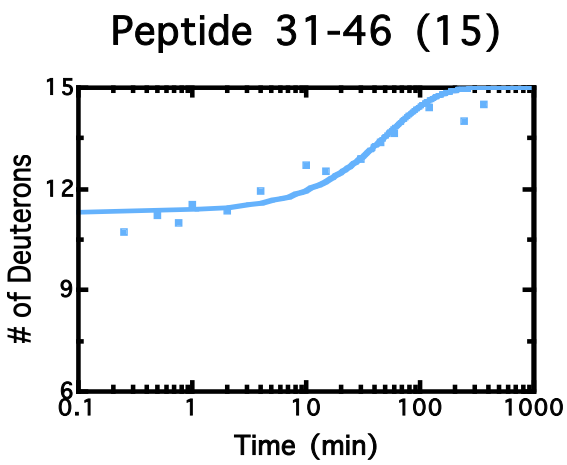

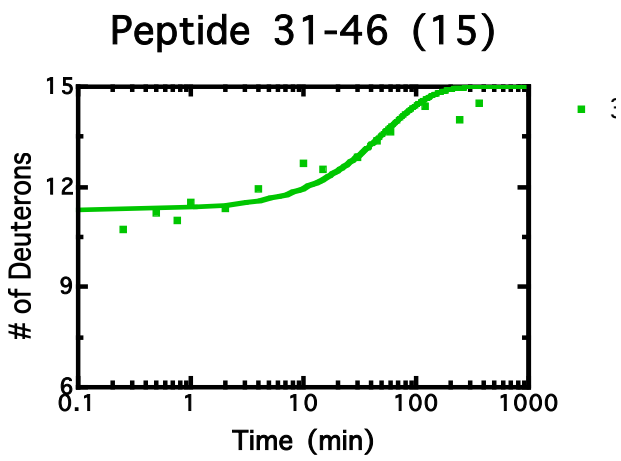

	31-46 (15)
single exponential	
Best-fit values	
A1	3.691
K1	0.01892
Std. Error	
A1	0.1900
K1	0.003779
95% Confidence Intervals	
A1	3.277 to 4.105
K1	0.01069 to 0.02716
Goodness of Fit	
Degrees of Freedom	12
R squared	0.8829
Absolute Sum of Squares	2.552
Sy.x	0.4611
Constraints	
A1	A1 > 0.0
K1	K1 > 0.0
Data	
Number of X values	14
Number of Y replicates	1

	31-46 (15)
single exponential	
Best-fit values	
A1	3.691
K1	0.01892
Std. Error	
A1	0.1900
K1	0.003779
95% Confidence Intervals	
A1	3.277 to 4.105
K1	0.01069 to 0.02716
Goodness of Fit	
Degrees of Freedom	12
R squared	0.8829
Absolute Sum of Squares	2.552
Sy.x	0.4611
Constraints	
A1	A1 > 0.0
K1	K1 > 0.0
Data	
Number of X values	14
Number of Y replicates	1

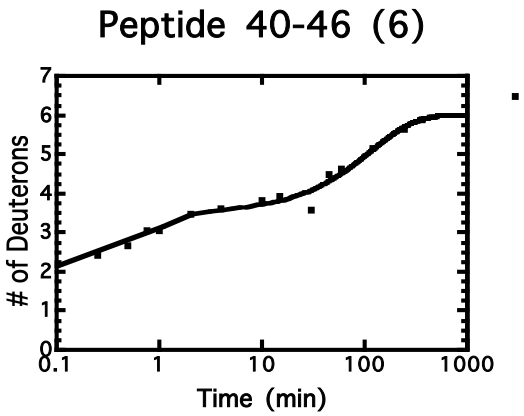

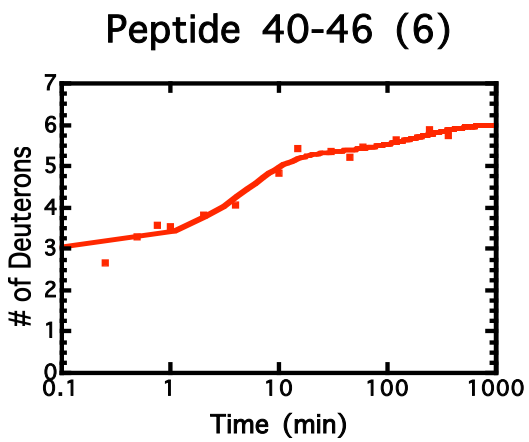

	40-46 (6)
double exponential	
Best-fit values	
A1	1.550
K1	1.307
A2	2.494
K2	0.008601
Std. Error	
A1	0.3722
K1	0.5453
A2	0.1210
K2	0.001277
95% Confidence Intervals	
A1	0.7213 to 2.380
K1	0.09204 to 2.522
A2	2.224 to 2.763
K2	0.005755 to 0.01145
Goodness of Fit	
Degrees of Freedom	10
R squared	0.9766
Absolute Sum of Squares	0.3528
Sy.x	0.1878

	40-46 (6)
double exponential	
Best-fit values	
A1	2.256
K1	0.1996
A2	0.7595
K2	0.004830
Std. Error	
A1	0.2089
K1	0.05649
A2	0.1879
K2	0.003038
95% Confidence Intervals	
A1	1.791 to 2.722
K1	0.07373 to 0.3254
A2	0.3408 to 1.178
K2	0.0 to 0.01160
Goodness of Fit	
Degrees of Freedom	10
R squared	0.9692
Absolute Sum of Squares	0.4569
Sy.x	0.2138

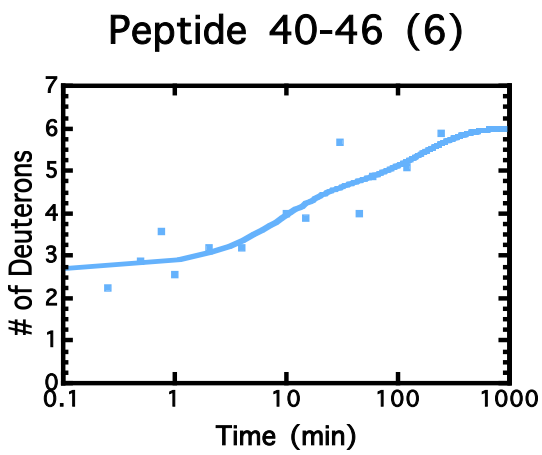

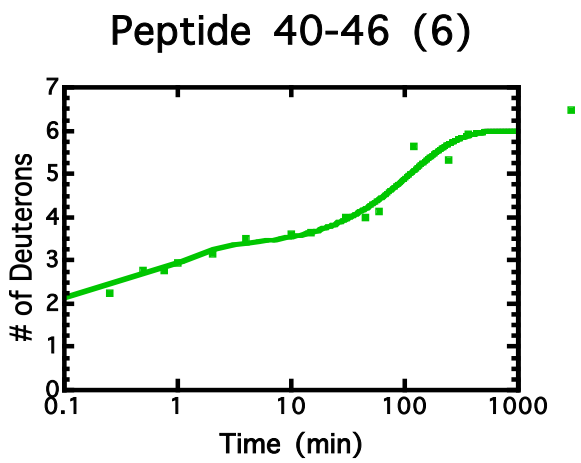

	40-46 (6)
double exponential	
Best-fit values	
A1	1.700
K1	0.1157
A2	1.619
K2	0.006087
Std. Error	
A1	0.7957
K1	0.1147
A2	0.8081
K2	0.006400
95% Confidence Intervals	
A1	0.0 to 3.500
K1	0.0 to 0.3751
A2	0.0 to 3.447
K2	0.0 to 0.02056
Goodness of Fit	
Degrees of Freedom	9
R squared	0.8218
Absolute Sum of Squares	2.840
Sy.x	0.5617

	40-46 (6)
double exponential	
Best-fit values	
A1	1.346
K1	1.212
A2	2.685
K2	0.008819
Std. Error	
A1	0.4722
K1	0.7723
A2	0.1666
K2	0.001645
95% Confidence Intervals	
A1	0.2940 to 2.398
K1	0.0 to 2.933
A2	2.314 to 3.056
K2	0.005153 to 0.01248
Goodness of Fit	
Degrees of Freedom	10
R squared	0.9612
Absolute Sum of Squares	0.6336
Sy.x	0.2517

Peptide 42-46 (4)

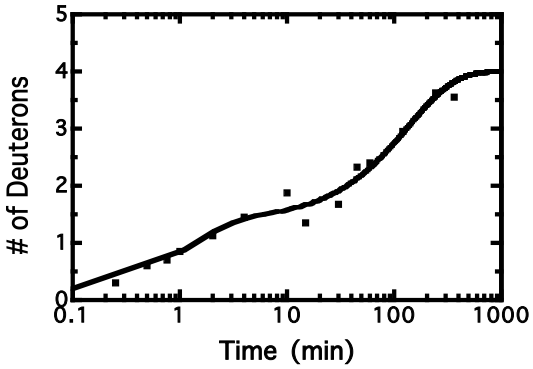

	42-46 (4)
double exponential	
Best-fit values	
A1	1.295
K1	0.8027
A2	2.607
K2	0.007324
Std. Error	
A1	0.2766
K1	0.3801
A2	0.1310
K2	0.001091
95% Confidence Intervals	
A1	0.6788 to 1
K1	0.0 to 1.65(
A2	2.315 to 2.8
K2	0.004894 tc
Goodness of Fit	
Degrees of Freedom	10
R squared	0.9754
Absolute Sum of Squares	0.3686
Sy.x	0.1920

Peptide 42-46 (4)

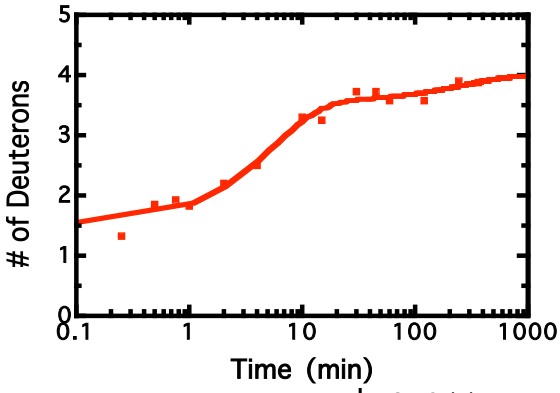

	42-46 (4)
double exponential	
Best-fit values	
A1	2.035
K1	0.1795
A2	0.4511
K2	0.003628
Std. Error	
A1	0.1419
K1	0.03868
A2	0.1255
K2	0.002795
95% Confidence Intervals	
A1	1.719 to 2.:
K1	0.09328 to
A2	0.1714 to 0
K2	0.0 to 0.00!
Goodness of Fit	
Degrees of Freedom	10
R squared	0.9785
Absolute Sum of Squares	0.2331
Sy.x	0.1527

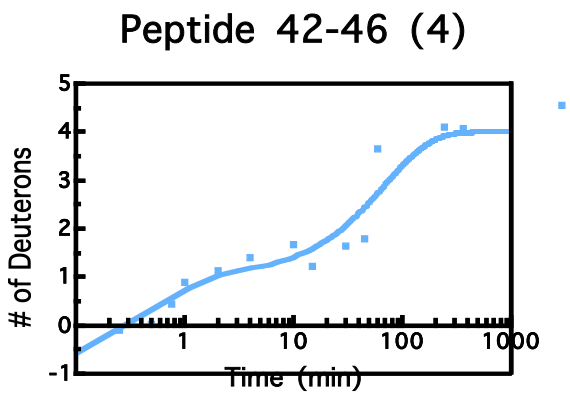

	42-46 (4)
double exponential	
Best-fit values	
A1	1.867
K1	1.696
A2	2.994
K2	0.01448
Std. Error	
A1	1.079
K1	1.559
A2	0.3399
K2	0.004937
95% Confidence Intervals	
A1	0.0 to 4.307
K1	0.0 to 5.222
A2	2.226 to 3.763
K2	0.003315 to 0.02565
Goodness of Fit	
Degrees of Freedom	9
R squared	0.9244
Absolute Sum of Squares	1.827
Sy.x	0.4506

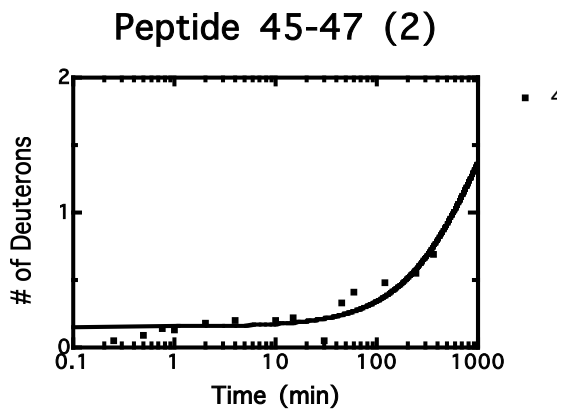

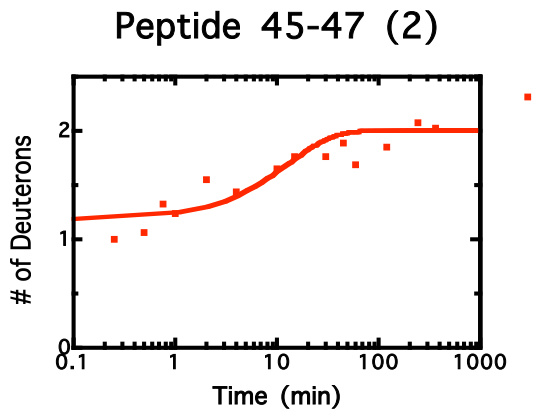

	45-47 (2)
single exponential	
Best-fit values	
A1	1.845
K1	0.001072
Std. Error	
A1	0.02757
K1	0.0001580
95% Confidence Intervals	
A1	1.785 to 1.906
K1	0.0007277 to 0.001416
Goodness of Fit	
Degrees of Freedom	12
R squared	0.8244
Absolute Sum of Squares	0.08853
Sy.x	0.08589
Constraints	
A1	A1 > 0.0
K1	K1 > 0.0
Data	
Number of X values	14
Number of Y replicates	1

	45-47 (2)
single exponential	
Best-fit values	
A1	0.8161
K1	0.07547
Std. Error	
A1	0.07951
K1	0.02636
95% Confidence Intervals	
A1	0.6428 to 0.9893
K1	0.01804 to 0.1329
Goodness of Fit	
Degrees of Freedom	12
R squared	0.8044
Absolute Sum of Squares	0.2927
Sy.x	0.1562
Constraints	
A1	A1 > 0.0
K1	K1 > 0.0
Data	
Number of X values	14
Number of Y replicates	1

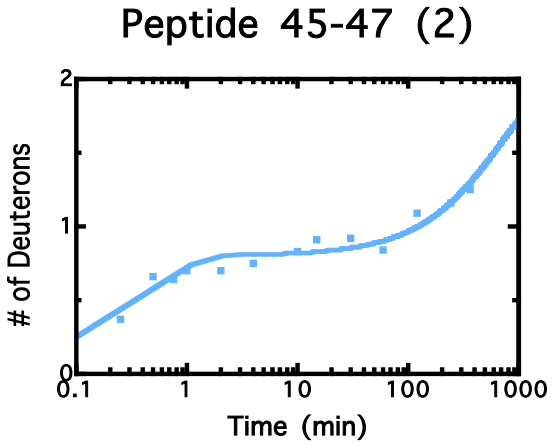

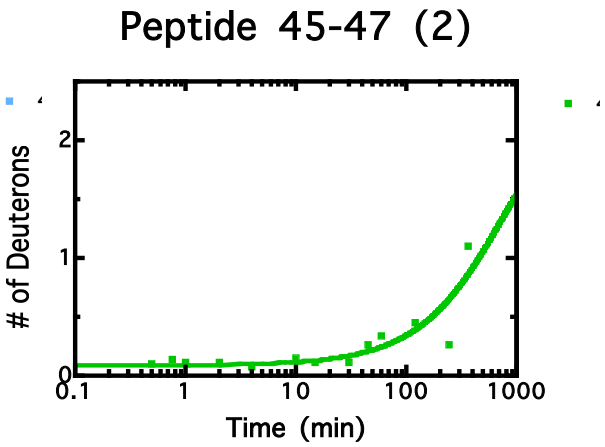

	45-47 (2)
double exponential	
Best-fit values	
A1	0.6800
K1	2.169
A2	1.198
K2	0.001467
Std. Error	
A1	0.2221
K1	0.8880
A2	0.03333
K2	0.0002466
95% Confidence Intervals	
A1	0.1777 to 1.182
K1	0.1601 to 4.177
A2	1.123 to 1.273
K2	0.0009088 to 0.002025
Goodness of Fit	
Degrees of Freedom	9
R squared	0.9301
Absolute Sum of Squares	0.04746
Sy.x	0.07262

	45-47 (2)
single exponential	
Best-fit values	
A1	1.912
K1	0.001425
Std. Error	
A1	0.04533
K1	0.0002725
95% Confidence Intervals	
A1	1.814 to 2.011
K1	0.0008310 to 0.002019
Goodness of Fit	
Degrees of Freedom	12
R squared	0.7610
Absolute Sum of Squares	0.2355
Sy.x	0.1401
Constraints	
A1	A1 > 0.0
K1	K1 > 0.0
Data	
Number of X values	14
Number of Y replicates	1

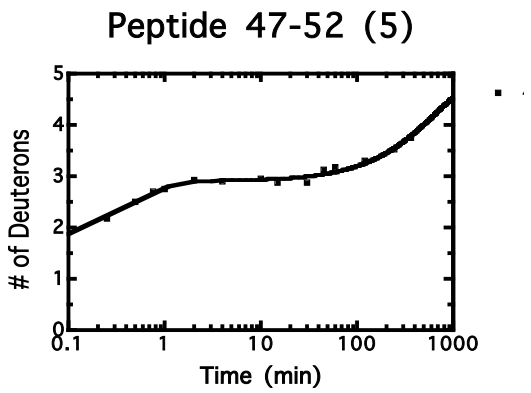

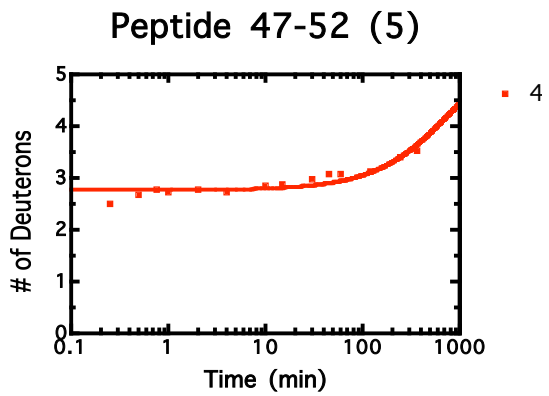

	47-52 (5)
double exponential	
Best-fit values	
A1	2.100
K1	0.001506
A2	1.287
K2	2.344
Std. Error	
A1	0.02750
K1	0.0001238
A2	0.2125
K2	0.4616
95% Confidence Intervals	
A1	2.039 to 2.161
K1	0.001230 to 0.001782
A2	0.8132 to 1.760
K2	1.315 to 3.372
Goodness of Fit	
Degrees of Freedom	10
R squared	0.9804
Absolute Sum of Squares	0.04038
Sy.x	0.06354

	47-52 (5)
single exponential	
Best-fit values	
A1	2.235
K1	0.001367
Std. Error	
A1	0.03869
K1	0.0001964
95% Confidence Intervals	
A1	2.150 to 2.319
K1	0.0009393 to 0.001795
Goodness of Fit	
Degrees of Freedom	12
R squared	0.8393
Absolute Sum of Squares	0.1720
Sy.x	0.1197
Constraints	
A1	A1 > 0.0
K1	K1 > 0.0
Data	
Number of X values	14
Number of Y replicates	1

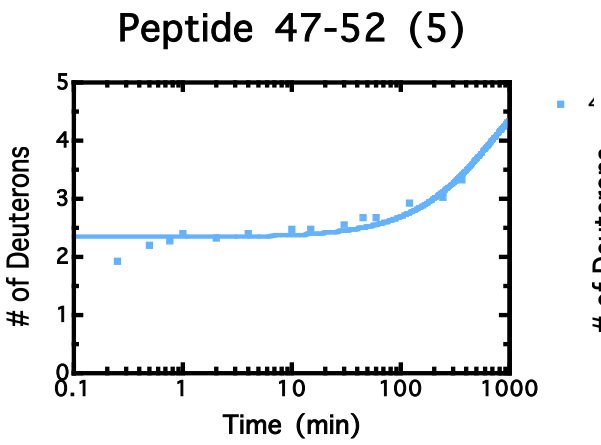

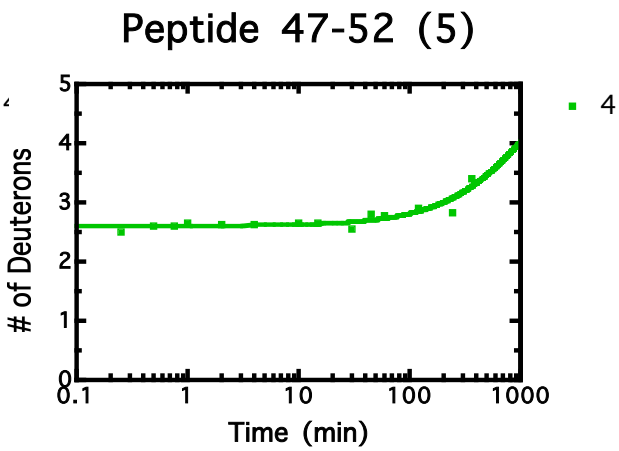

	47-52 (5)
single exponential	
Best-fit values	
A1	2.662
K1	0.001425
Std. Error	
A1	0.05148
K1	0.0002223
95% Confidence Intervals	
A1	2.550 to 2.774
K1	0.0009409 to 0.001910
Goodness of Fit	
Degrees of Freedom	12
R squared	0.8179
Absolute Sum of Squares	0.3037
Sy.x	0.1591
Constraints	
A1	A1 > 0.0
K1	K1 > 0.0
Data	
Number of X values	14
Number of Y replicates	1

	47-52 (5)
single exponential	
Best-fit values	
A1	2.396
K1	0.0008940
Std. Error	
A1	0.03192
K1	0.0001351
95% Confidence Intervals	
A1	2.326 to 2.465
K1	0.0005997 to 0.001188
Goodness of Fit	
Degrees of Freedom	12
R squared	0.8168
Absolute Sum of Squares	0.1197
Sy.x	0.09986
Constraints	
A1	A1 > 0.0
K1	K1 > 0.0
Data	
Number of X values	14
Number of Y replicates	1

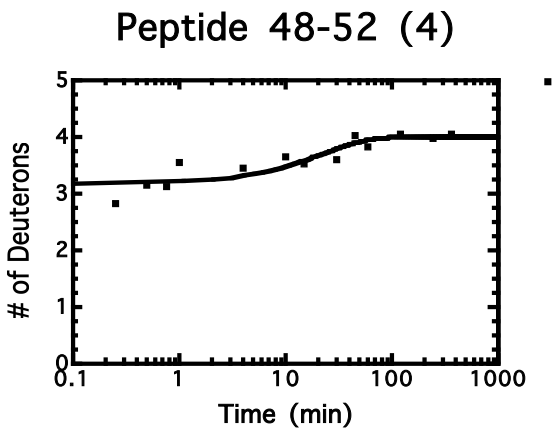

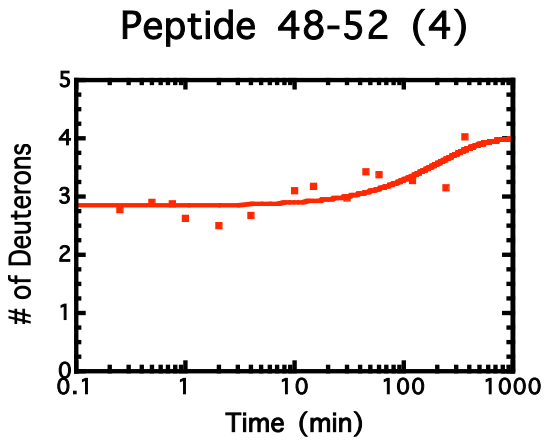

	48-52 (4)
single exponential	
Best-fit values	
A1	0.8248
K1	0.04541
Std. Error	
A1	0.09107
K1	0.01699
95% Confidence Intervals	
A1	0.6244 to 1
K1	0.008020 to
Goodness of Fit	
Degrees of Freedom	11
R squared	0.7973
Absolute Sum of Squares	0.3707
Sy.x	0.1836
Constraints	
A1	A1 > 0.0
K1	K1 > 0.0
Data	
Number of X values	14
Number of Y replicates	1

	48-52 (4)
single exponential	
Best-fit values	
A1	1.155
K1	0.004799
Std. Error	
A1	0.09068
K1	0.001823
95% Confidence Intervals	
A1	0.9574 to 1
K1	0.0008270
Goodness of Fit	
Degrees of Freedom	12
R squared	0.5993
Absolute Sum of Squares	0.8085
Sy.x	0.2596
Constraints	
A1	A1 > 0.0
K1	K1 > 0.0
Data	
Number of X values	14
Number of Y replicates	1

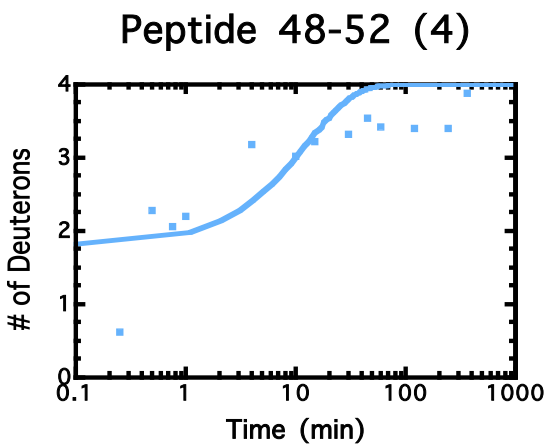

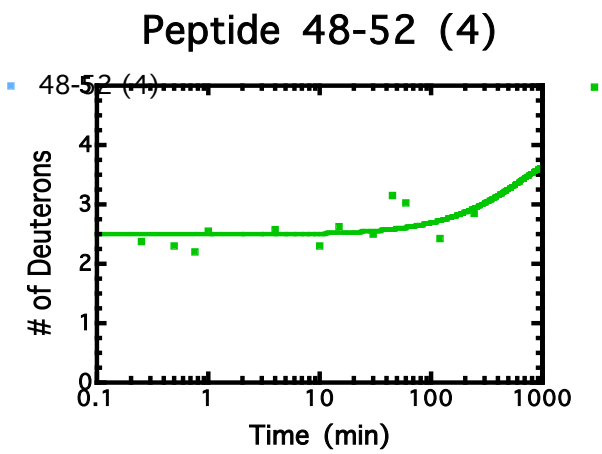

	48-52 (4)
single exponential	
Best-fit values	
A1	2.195
K1	0.07873
Std. Error	
A1	0.3165
K1	0.03895
95% Confidence Intervals	
A1	1.498 to 2.8
K1	0.0 to 0.164
Goodness of Fit	
Degrees of Freedom	11
R squared	0.5964
Absolute Sum of Squares	3.742
Sy.x	0.5832
Constraints	
A1	A1 > 0.0
K1	K1 > 0.0
Data	
Number of X values	14
Number of Y replicates	1

	48-52 (4)
single exponential	
Best-fit values	
A1	1.513
K1	0.001434
Std. Error	
A1	0.09854
K1	0.001006
95% Confidence Intervals	
A1	1.293 to 1.7
K1	0.0 to 0.003
Goodness of Fit	
Degrees of Freedom	10
R squared	0.1862
Absolute Sum of Squares	0.7756
Sy.x	0.2785
Constraints	
A1	A1 > 0.0
K1	K1 > 0.0
Data	
Number of X values	13
Number of Y replicates	1

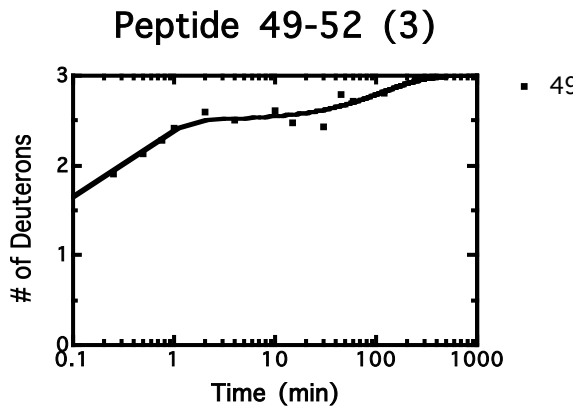

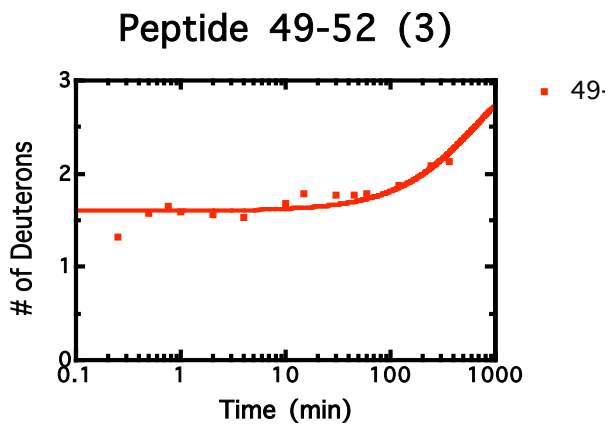

	49-52 (3)
double exponential	
Best-fit values	
A1	1.061
K1	2.185
A2	0.4942
K2	0.008490
Std. Error	
A1	0.2690
K1	0.7262
A2	0.05012
K2	0.002826
95% Confidence Intervals	
A1	0.4618 to 1.660
K1	0.5673 to 3.803
A2	0.3825 to 0.6058
K2	0.002193 to 0.01479
Goodness of Fit	
Degrees of Freedom	10
R squared	0.9386
Absolute Sum of Squares	0.07503
Sy.x	0.08662

	49-52 (3)
single exponential	
Best-fit values	
A1	1.400
K1	0.001636
Std. Error	
A1	0.03549
K1	0.0003062
95% Confidence Intervals	
A1	1.322 to 1.477
K1	0.0009684 to 0.002303
Goodness of Fit	
Degrees of Freedom	12
R squared	0.7645
Absolute Sum of Squares	0.1429
Sy.x	0.1091
Constraints	
A1	A1 > 0.0
K1	K1 > 0.0
Data	
Number of X values	14
Number of Y replicates	1

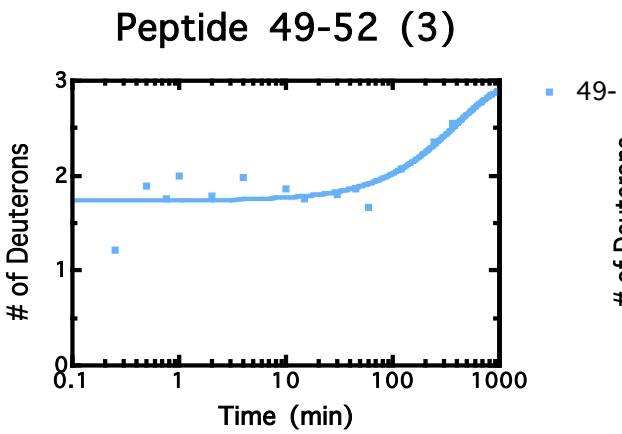

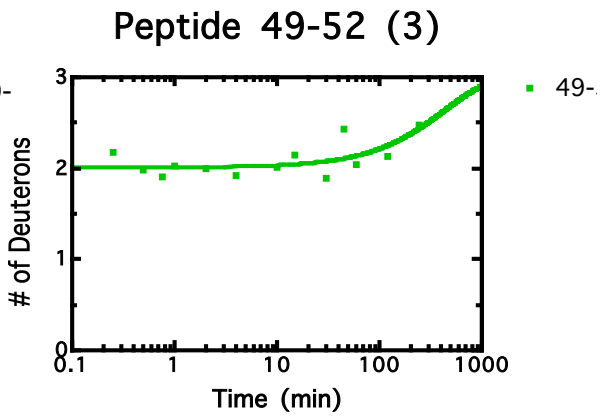

	49-52 (3)
single exponential	
Best-fit values	
A1	1.263
K1	0.002550
Std. Error	
A1	0.06732
K1	0.0007921
95% Confidence Intervals	
A1	1.117 to 1.410
K1	0.0008238 to 0.004276
Goodness of Fit	
Degrees of Freedom	12
R squared	0.6114
Absolute Sum of Squares	0.4932
Sy.x	0.2027
Constraints	
A1	A1 > 0.0
K1	K1 > 0.0
Data	
Number of X values	14
Number of Y replicates	1

	49-52 (3)
single exponential	
Best-fit values	
A1	0.9907
K1	0.002306
Std. Error	
A1	0.04833
K1	0.0009012
95% Confidence Intervals	
A1	0.8843 to 1.097
K1	0.0003221 to 0.004289
Goodness of Fit	
Degrees of Freedom	11
R squared	0.4592
Absolute Sum of Squares	0.2225
Sy.x	0.1422
Constraints	
A1	A1 > 0.0
K1	K1 > 0.0
Data	
Number of X values	13
Number of Y replicates	1

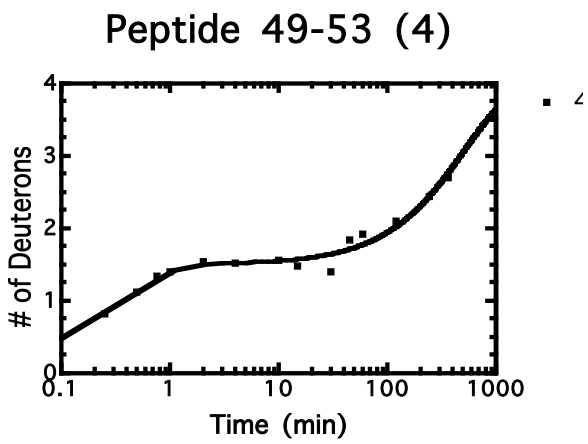

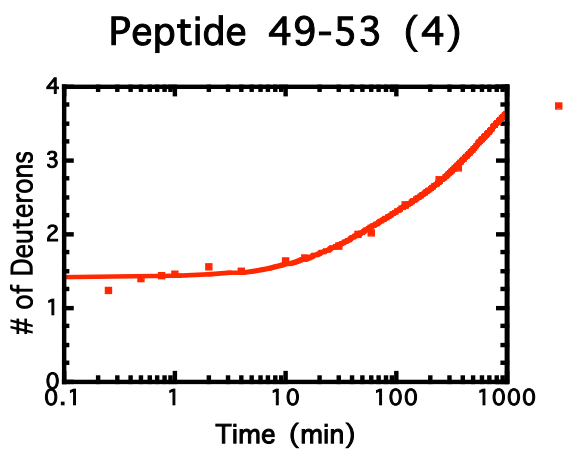

	49-53 (4)
double exponential	
Best-fit values	
A1	1.308
K1	2.533
A2	2.498
K2	0.001939
Std. Error	
A1	0.3968
K1	0.8824
A2	0.04726
K2	0.0001971
95% Confidence Intervals	
A1	0.4242 to 2.192
K1	0.5668 to 4.499
A2	2.392 to 2.603
K2	0.001499 to 0.002378
Goodness of Fit	
Degrees of Freedom	10
R squared	0.9643
Absolute Sum of Squares	0.1170
Sy.x	0.1082

	49-53 (4)
double exponential	
Best-fit values	
A1	0.6396
K1	0.02592
A2	1.949
K2	0.001694
Std. Error	
A1	0.2212
K1	0.01329
A2	0.2271
K2	0.0004497
95% Confidence Intervals	
A1	0.1466 to 1.132
K1	0.0 to 0.05554
A2	1.443 to 2.454
K2	0.0006922 to 0.00269
Goodness of Fit	
Degrees of Freedom	10
R squared	0.9833
Absolute Sum of Squares	0.05768
Sy.x	0.07595

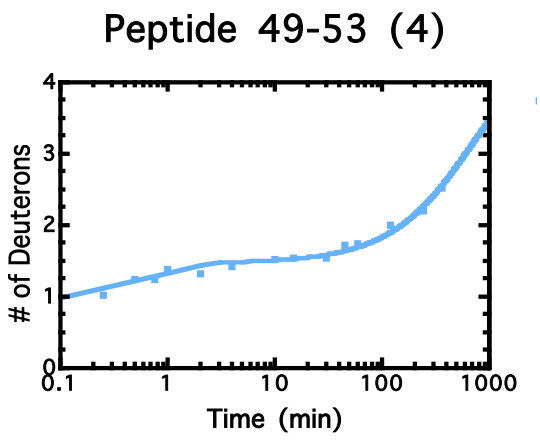

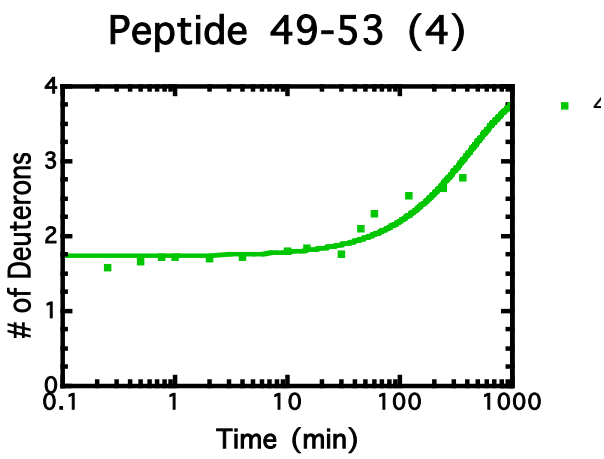

	49-53 (4)
double exponential	
Best-fit values	
A1	0.5451
K1	1.246
A2	2.530
K2	0.001544
Std. Error	
A1	0.1404
K1	0.5356
A2	0.03453
K2	0.0001235
95% Confidence Intervals	
A1	0.2322 to 0.8580
K1	0.05312 to 2.440
A2	2.453 to 2.607
K2	0.001269 to 0.00181
Goodness of Fit	
Degrees of Freedom	10
R squared	0.9749
Absolute Sum of Squares	0.05457
Sy.x	0.07387

	49-53 (4)
single exponential	
Best-fit values	
A1	2.264
K1	0.002279
Std. Error	
A1	0.04971
K1	0.0003072
95% Confidence Intervals	
A1	2.156 to 2.373
K1	0.001609 to 0.002948
Goodness of Fit	
Degrees of Freedom	12
R squared	0.8747
Absolute Sum of Squares	0.2723
Sy.x	0.1506
Constraints	
A1	A1 > 0.0
K1	K1 > 0.0
Data	
Number of X values	14
Number of Y replicates	1

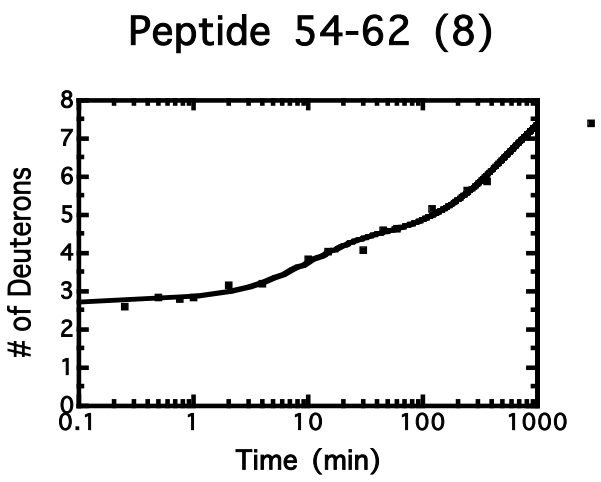

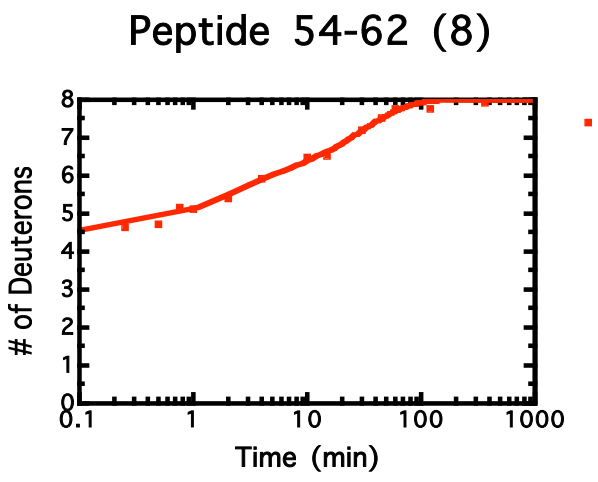

	54-62 (8)
double exponential	
Best-fit values	
A1	3.726
K1	0.001775
A2	1.581
K2	0.09936
Std. Error	
A1	0.1252
K1	0.0002173
A2	0.1337
K2	0.02374
95% Confidence Intervals	
A1	3.447 to 4.(
K1	0.001291 tc
A2	1.283 to 1.8
K2	0.04646 to
Goodness of Fit	
Degrees of Freedom	10
R squared	0.9875
Absolute Sum of Squares	0.2011
Sy.x	0.1418

	54-62 (8)
double exponential	
Best-fit values	
A1	1.275
K1	0.5848
A2	2.262
K2	0.03397
Std. Error	
A1	0.1945
K1	0.2139
A2	0.1922
K2	0.004480
95% Confidence Intervals	
A1	0.8420 to 1
K1	0.1081 to 1
A2	1.833 to 2.(
K2	0.02399 to
Goodness of Fit	
Degrees of Freedom	10
R squared	0.9937
Absolute Sum of Squares	0.1337
Sy.x	0.1156

Peptide 54-62 (8)

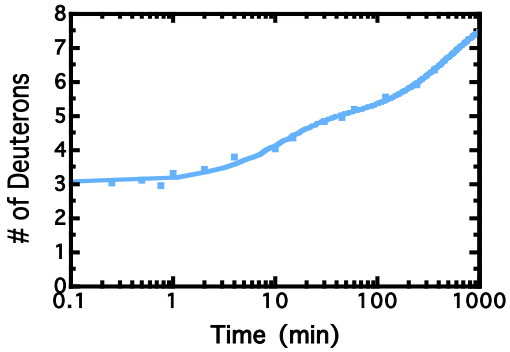

	54-62 (8)
double exponential	
Best-fit values	
A1	3.171
K1	0.001843
A2	1.783
K2	0.08532
Std. Error	
A1	0.1139
K1	0.0002237
A2	0.1181
K2	0.01536
95% Confidence Intervals	
A1	2.917 to 3.4
K1	0.001344 to
A2	1.520 to 2.0
K2	0.05110 to
Goodness of Fit	
Degrees of Freedom	10
R squared	0.9918
Absolute Sum of Squares	0.1384
Sy.x	0.1176

Peptide 54-62 (8)

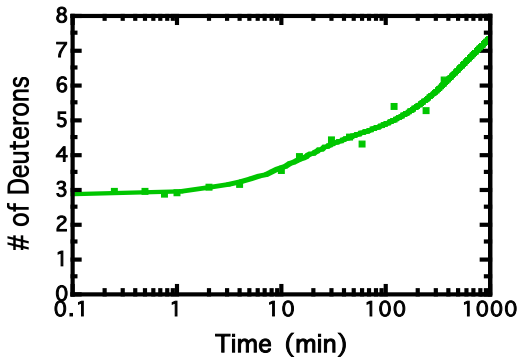

	54-62 (8)
double exponential	
Best-fit values	
A1	3.696
K1	0.001758
A2	1.442
K2	0.06710
Std. Error	
A1	0.2325
K1	0.0003540
A2	0.2324
K2	0.02745
95% Confidence Intervals	
A1	3.178 to 4.2
K1	0.0009695
A2	0.9242 to 1
K2	0.005931 to
Goodness of Fit	
Degrees of Freedom	10
R squared	0.9723
Absolute Sum of Squares	0.4180
Sy.x	0.2044

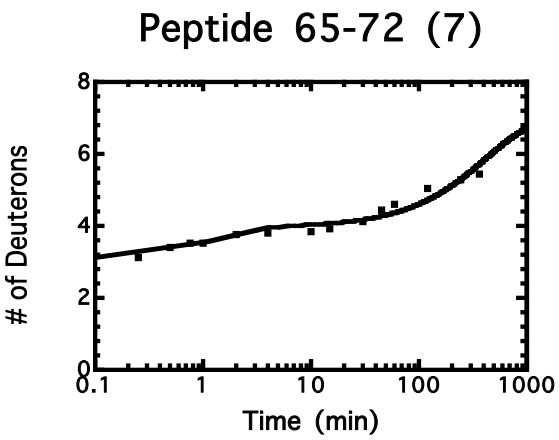

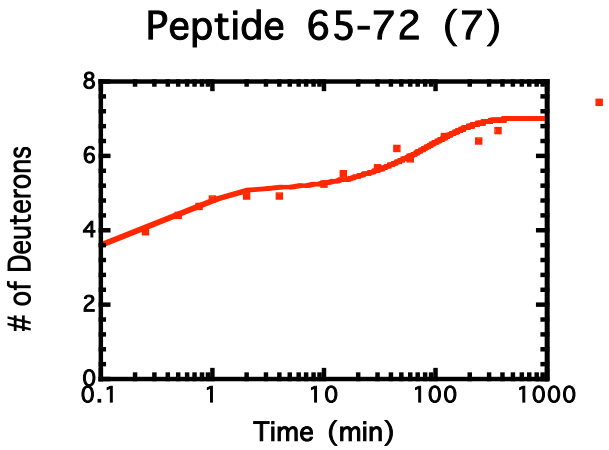

	65-72 (7)
double exponential	
Best-fit values	
A1	3.036
K1	0.002366
A2	0.9088
K2	0.6966
Std. Error	
A1	0.1005
K1	0.0003343
A2	0.2476
K2	0.4275
95% Confidence Intervals	
A1	2.812 to 3.260
K1	0.001621 to 0.00311
A2	0.3573 to 1.460
K2	0.0 to 1.649
Goodness of Fit	
Degrees of Freedom	10
R squared	0.9477
Absolute Sum of Squares	0.3601
Sy.x	0.1898

	65-72 (7)
double exponential	
Best-fit values	
A1	1.748
K1	1.857
A2	1.938
K2	0.01109
Std. Error	
A1	0.6128
K1	0.9504
A2	0.1505
K2	0.002579
95% Confidence Intervals	
A1	0.3824 to 3.113
K1	0.0 to 3.974
A2	1.603 to 2.273
K2	0.005340 to 0.01683
Goodness of Fit	
Degrees of Freedom	10
R squared	0.9414
Absolute Sum of Squares	0.5423
Sy.x	0.2329

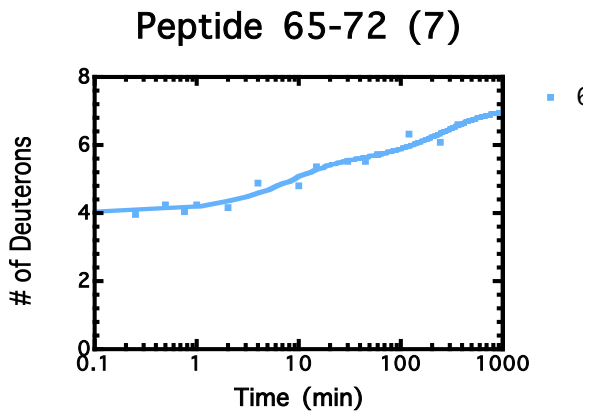

	65-72 (7)
double exponential	
Best-fit values	
A1	1.395
K1	0.1229
A2	1.591
K2	0.003605
Std. Error	
A1	0.2135
K1	0.05213
A2	0.2026
K2	0.001156
95% Confidence Intervals	
A1	0.9198 to 1.871
K1	0.006800 to 0.2391
A2	1.140 to 2.042
K2	0.001031 to 0.00618
Goodness of Fit	
Degrees of Freedom	10
R squared	0.9572
Absolute Sum of Squares	0.4458
Sy.x	0.2111

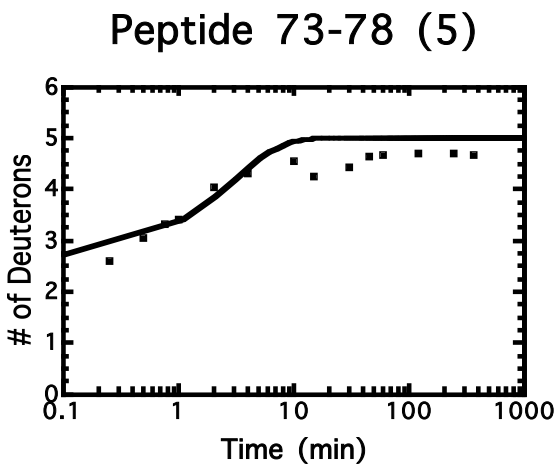

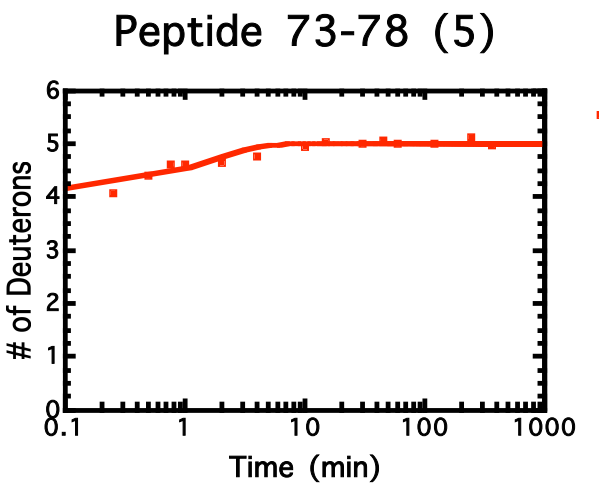

	73-78 (5)
single exponential	
Best-fit values	
A1	2.356
K1	0.3491
Std. Error	
A1	0.3210
K1	0.1320
95% Confidence Intervals	
A1	1.656 to 3.055
K1	0.06151 to 0.6368
Goodness of Fit	
Degrees of Freedom	12
R squared	0.7490
Absolute Sum of Squares	1.641
Sy.x	0.3698
Constraints	
A1	A1 > 0.0
K1	K1 > 0.0
Data	
Number of X values	14
Number of Y replicates	1

	73-78 (5)
single exponential	
Best-fit values	
A1	0.8943
K1	0.6287
Std. Error	
A1	0.1239
K1	0.1869
95% Confidence Intervals	
A1	0.6243 to 1.164
K1	0.2213 to 1.036
Goodness of Fit	
Degrees of Freedom	12
R squared	0.8912
Absolute Sum of Squares	0.1295
Sy.x	0.1039
Constraints	
A1	A1 > 0.0
K1	K1 > 0.0
Data	
Number of X values	14
Number of Y replicates	1

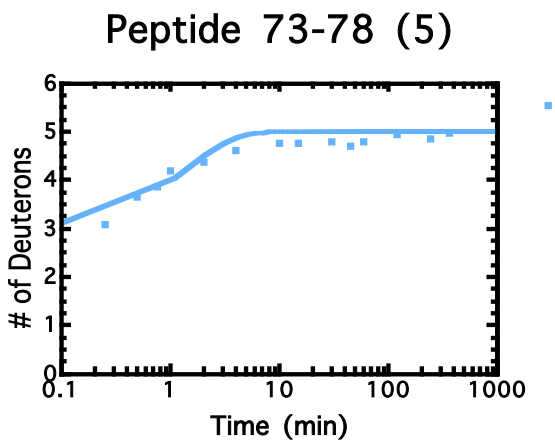

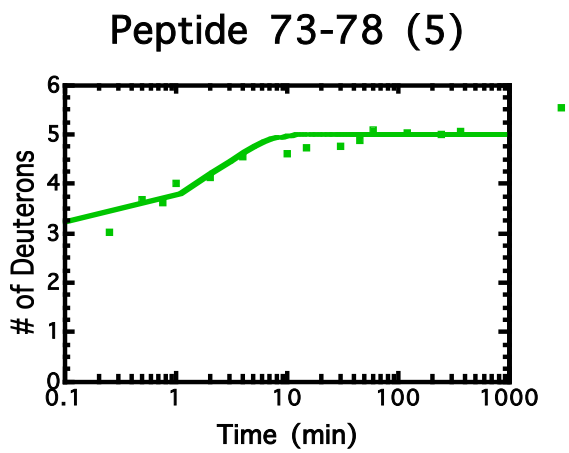

	73-78 (5)
single exponential	
Best-fit values	
A1	2.029
K1	0.6839
Std. Error	
A1	0.2642
K1	0.1836
95% Confidence Intervals	
A1	1.454 to 2.605
K1	0.2840 to 1.084
Goodness of Fit	
Degrees of Freedom	12
R squared	0.8707
Absolute Sum of Squares	0.5280
Sy.x	0.2098
Constraints	
A1	A1 > 0.0
K1	K1 > 0.0
Data	
Number of X values	14
Number of Y replicates	1

	73-78 (5)
single exponential	
Best-fit values	
A1	1.855
K1	0.4060
Std. Error	
A1	0.1887
K1	0.1077
95% Confidence Intervals	
A1	1.444 to 2.267
K1	0.1713 to 0.6407
Goodness of Fit	
Degrees of Freedom	12
R squared	0.9101
Absolute Sum of Squares	0.4893
Sy.x	0.2019
Constraints	
A1	A1 > 0.0
K1	K1 > 0.0
Data	
Number of X values	14
Number of Y replicates	1

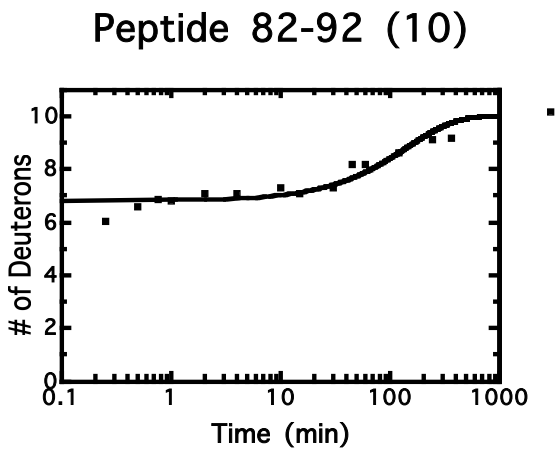

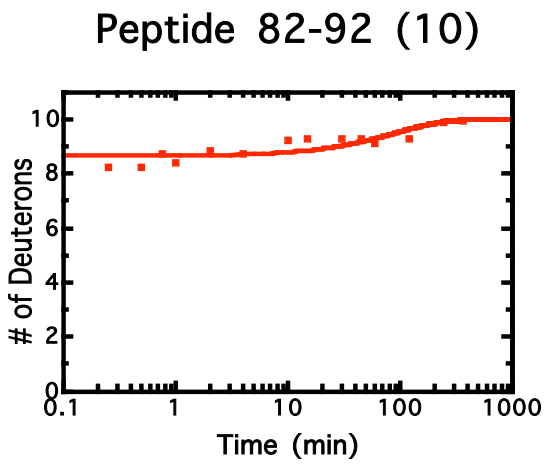

	82-92 (10)
single exponential	
Best-fit values	
A1	3.195
K1	0.006939
Std. Error	
A1	0.1319
K1	0.001321
95% Confidence Intervals	
A1	2.907 to 3.4
K1	0.004060 to
Goodness of Fit	
Degrees of Freedom	12
R squared	0.8710
Absolute Sum of Squares	1.569
Sy.x	0.3616
Constraints	
A1	A1 > 0.0
K1	K1 > 0.0
Data	
Number of X values	14
Number of Y replicates	1

	82-92 (10)
single exponential	
Best-fit values	
A1	1.352
K1	0.01079
Std. Error	
A1	0.1161
K1	0.004012
95% Confidence Intervals	
A1	1.099 to 1.6
K1	0.002047 to
Goodness of Fit	
Degrees of Freedom	12
R squared	0.7104
Absolute Sum of Squares	1.084
Sy.x	0.3005
Constraints	
A1	A1 > 0.0
K1	K1 > 0.0
Data	
Number of X values	14
Number of Y replicates	1

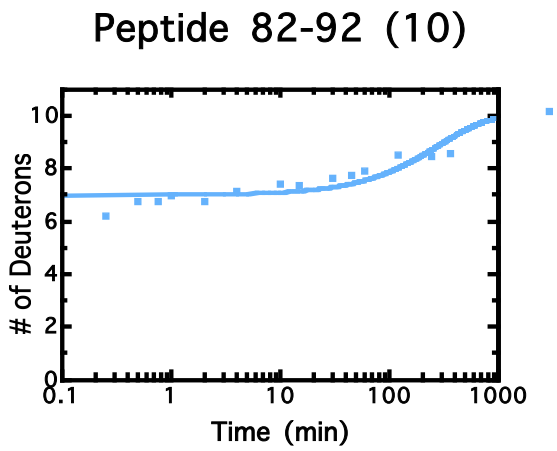

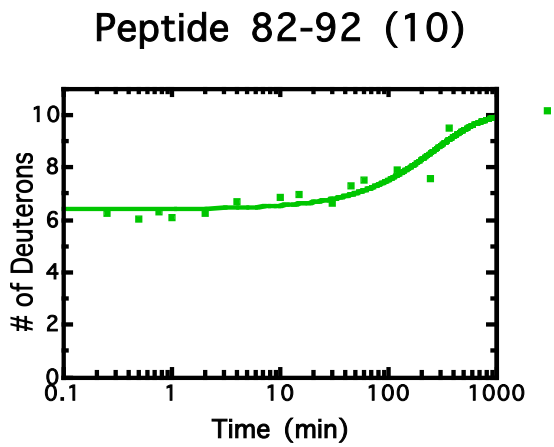

	82-92 (10)
single exponential	
Best-fit values	
A1	3.009
K1	0.003435
Std. Error	
A1	0.1347
K1	0.0008030
95% Confidence Intervals	
A1	2.716 to 3.3
K1	0.001685 to
Goodness of Fit	
Degrees of Freedom	12
R squared	0.7276
Absolute Sum of Squares	1.897
Sy.x	0.3976
Constraints	
A1	A1 > 0.0
K1	K1 > 0.0
Data	
Number of X values	14
Number of Y replicates	1

	82-92 (10)
single exponential	
Best-fit values	
A1	3.585
K1	0.003686
Std. Error	
A1	0.1416
K1	0.0007457
95% Confidence Intervals	
A1	3.276 to 3.8
K1	0.002061 to
Goodness of Fit	
Degrees of Freedom	12
R squared	0.8167
Absolute Sum of Squares	2.072
Sy.x	0.4156
Constraints	
A1	A1 > 0.0
K1	K1 > 0.0
Data	
Number of X values	14
Number of Y replicates	1

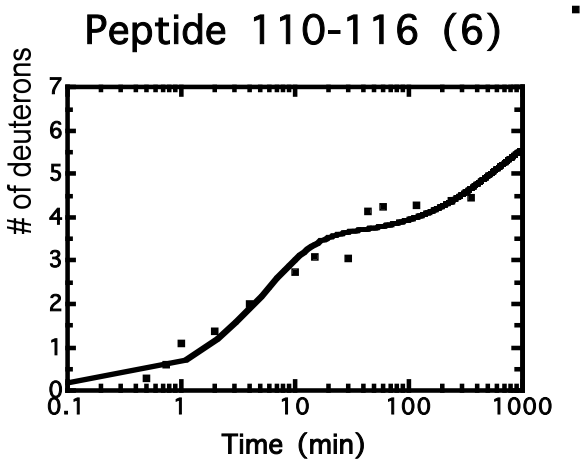

	110-116 (6)
double exponential	
Best-fit values	
A1	3.447
K1	0.1745
A2	2.441
K2	0.001683
Std. Error	
A1	0.3327
K1	0.05388
A2	0.2741
K2	0.0008132
95% Confidence Intervals	
A1	2.705 to 4.188
K1	0.05447 to 0.2946
A2	1.830 to 3.052
K2	0.0 to 0.003495
Goodness of Fit	
Degrees of Freedom	10
R squared	0.9580
Absolute Sum of Squares	1.524
Sy.x	0.3904

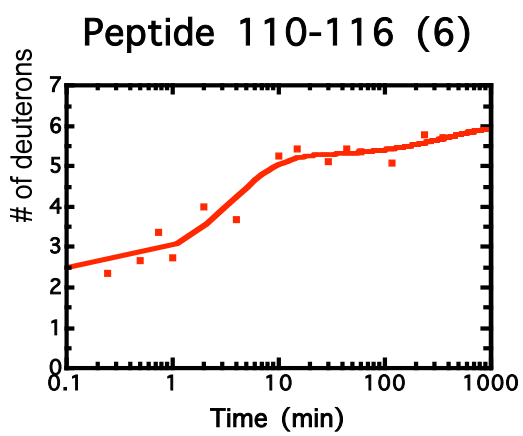

	110-116 (6)
double exponential	
Best-fit values	
A1	2.830
K1	0.2519
A2	0.7559
K2	0.002474
Std. Error	
A1	0.3091
K1	0.08700
A2	0.2275
K2	0.002698
95% Confidence Intervals	
A1	2.141 to 3.519
K1	0.05805 to 0.4457
A2	0.2489 to 1.263
K2	0.0 to 0.008485
Goodness of Fit	
Degrees of Freedom	10
R squared	0.9401
Absolute Sum of Squares	1.188
Sy.x	0.3446

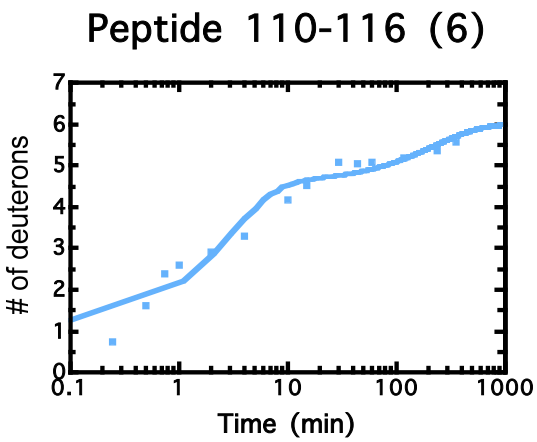

	110-116 (6)
double exponential	
Best-fit values	
A1	3.444
K1	0.3295
A2	1.414
K2	0.004386
Std. Error	
A1	0.3792
K1	0.1064
A2	0.2662
K2	0.002463
95% Confidence Intervals	
A1	2.599 to 4.289
K1	0.09237 to 0.5667
A2	0.8210 to 2.007
K2	0.0 to 0.009874
Goodness of Fit	
Degrees of Freedom	10
R squared	0.9538
Absolute Sum of Squares	1.462
Sy.x	0.3824

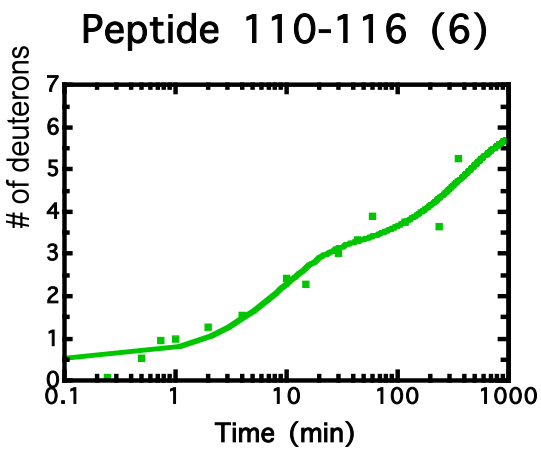

	110-116 (6)
double exponential	
Best-fit values	
A1	2.983
K1	0.002393
A2	2.516
K2	0.1135
Std. Error	
A1	0.3475
K1	0.0008602
A2	0.3737
K2	0.04792
95% Confidence Intervals	
A1	2.209 to 3.757
K1	0.0004760 to 0.004
A2	1.683 to 3.349
K2	0.006758 to 0.2203
Goodness of Fit	
Degrees of Freedom	10
R squared	0.9480
Absolute Sum of Squares	1.557
Sy.x	0.3946

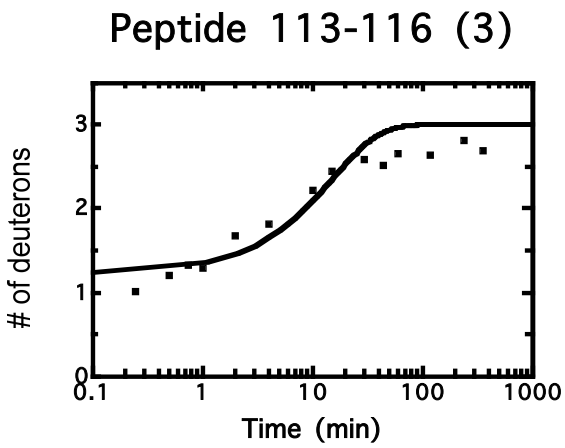

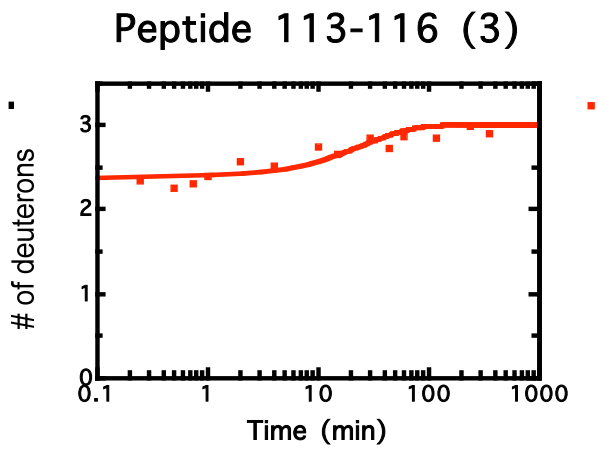

	113-116 (3)
single exponential	
Best-fit values	
A1	1.767
K1	0.06578
Std. Error	
A1	0.1213
K1	0.01633
95% Confidence Intervals	
A1	1.503 to 2.(
K1	0.03021 to
Goodness of Fit	
Degrees of Freedom	12
R squared	0.8695
Absolute Sum of Squares	0.7187
Sy.x	0.2447
Constraints	
A1	A1 > 0.0
K1	K1 > 0.0
Data	
Number of X values	14
Number of Y replicates	1

	113-116 (3)
single exponential	
Best-fit values	
A1	0.6210
K1	0.03705
Std. Error	
A1	0.05047
K1	0.01090
95% Confidence Intervals	
A1	0.5110 to 0
K1	0.01329 to
Goodness of Fit	
Degrees of Freedom	12
R squared	0.8048
Absolute Sum of Squares	0.1522
Sy.x	0.1126
Constraints	
A1	A1 > 0.0
K1	K1 > 0.0
Data	
Number of X values	14
Number of Y replicates	1

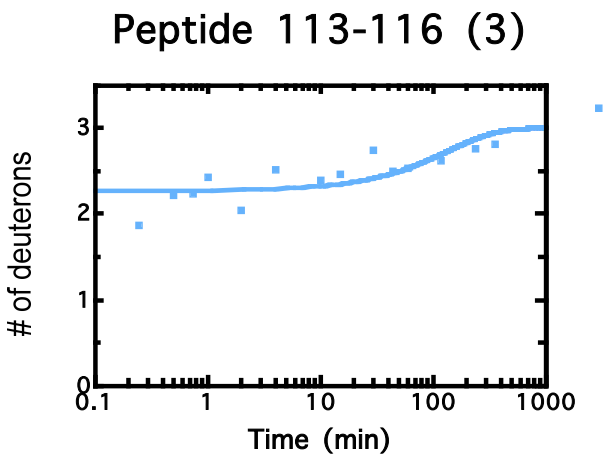

	113-116 (3)
single exponential	
Best-fit values	
A1	0.7288
K1	0.007294
Std. Error	
A1	0.07206
K1	0.003322
95% Confidence Intervals	
A1	0.5718 to 0
K1	5.6509e-00
Goodness of Fit	
Degrees of Freedom	12
R squared	0.5298
Absolute Sum of Squares	0.4614
Sy.x	0.1961
Constraints	
A1	A1 > 0.0
K1	K1 > 0.0
Data	
Number of X values	14
Number of Y replicates	1

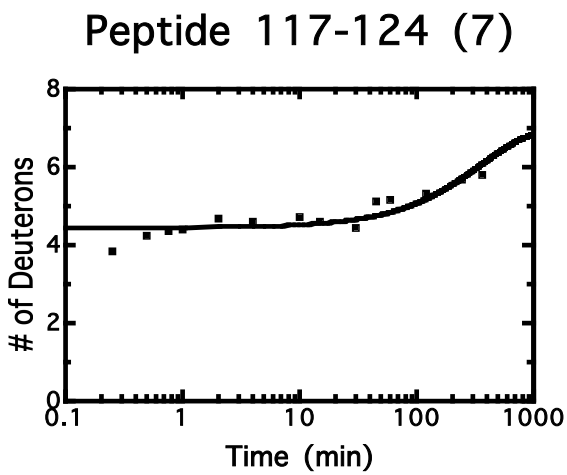

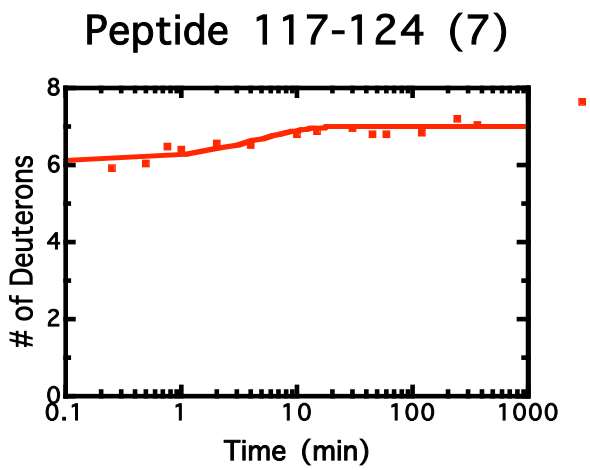

	117-124 (7)
single exponential	
Best-fit values	
A1	2.552
K1	0.002803
Std. Error	
A1	0.09298
K1	0.0005723
95% Confidence Intervals	
A1	2.349 to 2.7
K1	0.001556 to
Goodness of Fit	
Degrees of Freedom	12
R squared	0.7705
Absolute Sum of Squares	0.9297
Sy.x	0.2784
Constraints	
A1	A1 > 0.0
K1	K1 > 0.0
Data	
Number of X values	14
Number of Y replicates	1

	117-124 (7)
single exponential	
Best-fit values	
A1	0.8951
K1	0.2114
Std. Error	
A1	0.1147
K1	0.08808
95% Confidence Intervals	
A1	0.6452 to 1
K1	0.01950 to
Goodness of Fit	
Degrees of Freedom	12
R squared	0.8078
Absolute Sum of Squares	0.3277
Sy.x	0.1653
Constraints	
A1	A1 > 0.0
K1	K1 > 0.0
Data	
Number of X values	14
Number of Y replicates	1

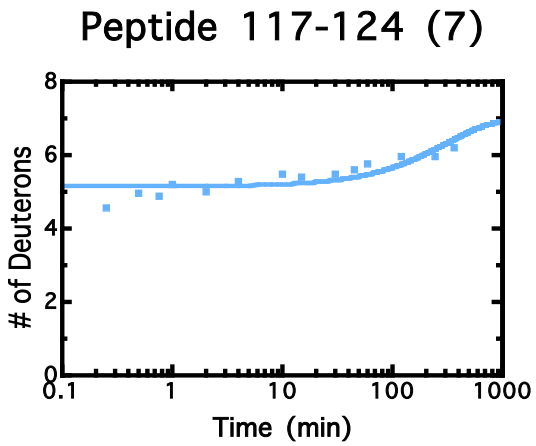

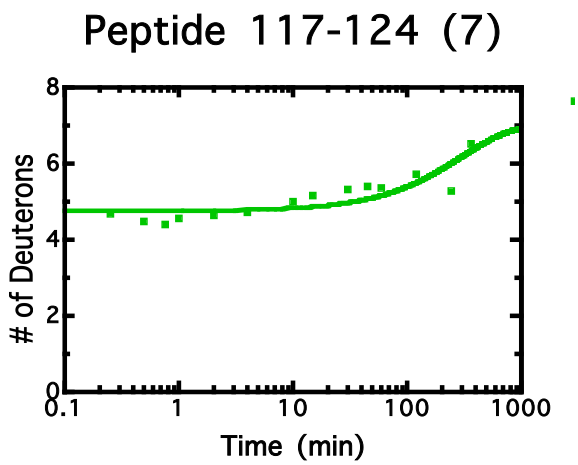

	117-124 (7)
single exponential	
Best-fit values	
A1	1.854
K1	0.003233
Std. Error	
A1	0.09196
K1	0.0008528
95% Confidence Intervals	
A1	1.654 to 2.(
K1	0.001375 tc
Goodness of Fit	
Degrees of Freedom	12
R squared	0.6753
Absolute Sum of Squares	0.8920
Sy.x	0.2726
Constraints	
A1	A1 > 0.0
K1	K1 > 0.0
Data	
Number of X values	14
Number of Y replicates	1

	117-124 (7)
single exponential	
Best-fit values	
A1	2.247
K1	0.003333
Std. Error	
A1	0.1075
K1	0.0008410
95% Confidence Intervals	
A1	2.013 to 2.4
K1	0.001501 tc
Goodness of Fit	
Degrees of Freedom	12
R squared	0.7184
Absolute Sum of Squares	1.214
Sy.x	0.3181
Constraints	
A1	A1 > 0.0
K1	K1 > 0.0
Data	
Number of X values	14
Number of Y replicates	1

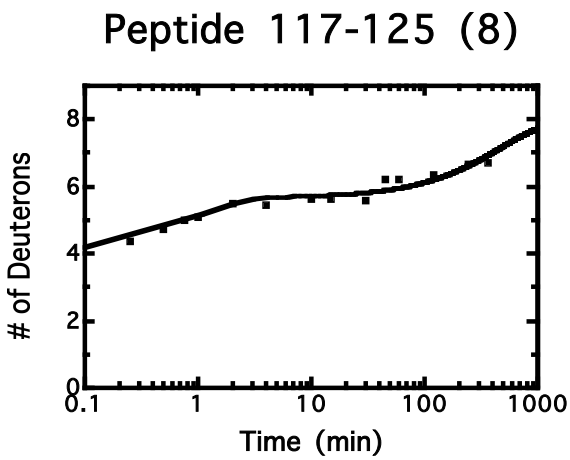

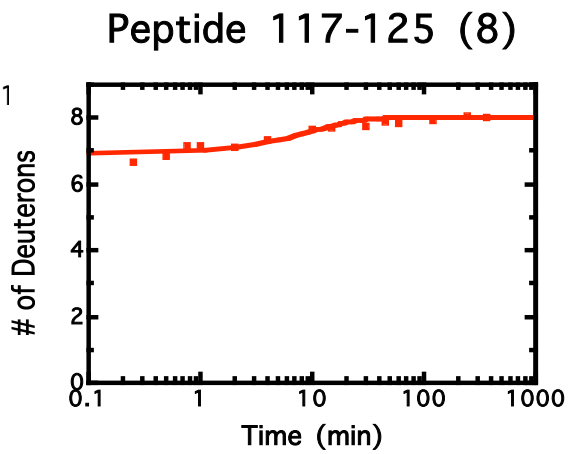

	117-125 (8)
double exponential	
Best-fit values	
A1	1.644
K1	1.064
A2	2.336
K2	0.002142
Std. Error	
A1	0.3381
K1	0.3998
A2	0.09738
K2	0.0004201
95% Confidence Intervals	
A1	0.8904 to 2.397
K1	0.1732 to 1.954
A2	2.119 to 2.553
K2	0.001206 to 0.00307
Goodness of Fit	
Degrees of Freedom	10
R squared	0.9400
Absolute Sum of Squares	0.3926
Sy.x	0.1981

	117-125 (8)
single exponential	
Best-fit values	
A1	1.103
K1	0.1001
Std. Error	
A1	0.07826
K1	0.02505
95% Confidence Intervals	
A1	0.9329 to 1.274
K1	0.04551 to 0.1547
Goodness of Fit	
Degrees of Freedom	12
R squared	0.9052
Absolute Sum of Squares	0.2501
Sy.x	0.1444
Constraints	
A1	A1 > 0.0
K1	K1 > 0.0
Data	
Number of X values	14
Number of Y replicates	1

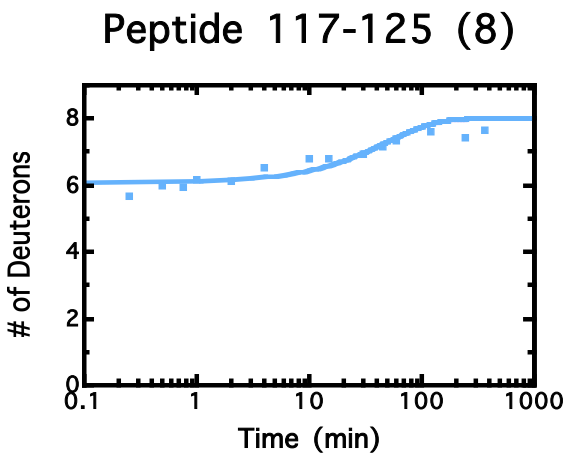

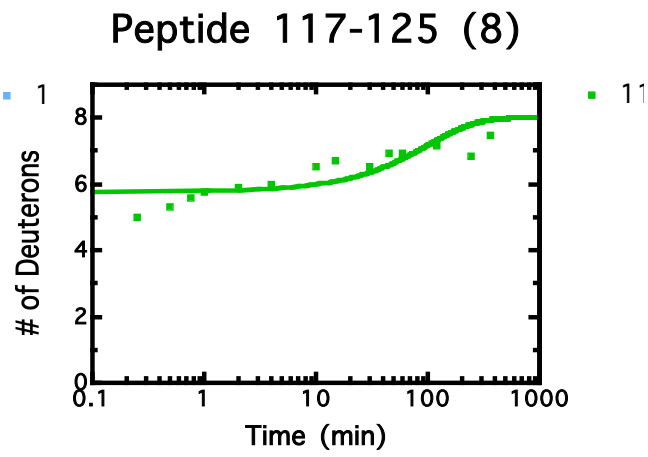

	117-125 (8)
single exponential	
Best-fit values	
A1	1.919
K1	0.02010
Std. Error	
A1	0.1203
K1	0.004831
95% Confidence Intervals	
A1	1.657 to 2.181
K1	0.009577 to 0.03063
Goodness of Fit	
Degrees of Freedom	12
R squared	0.8233
Absolute Sum of Squares	1.010
Sy.x	0.2901
Constraints	
A1	A1 > 0.0
K1	K1 > 0.0
Data	
Number of X values	14
Number of Y replicates	1

	117-125 (8)
single exponential	
Best-fit values	
A1	2.222
K1	0.009844
Std. Error	
A1	0.1877
K1	0.003657
95% Confidence Intervals	
A1	1.813 to 2.631
K1	0.001875 to 0.01781
Goodness of Fit	
Degrees of Freedom	12
R squared	0.5963
Absolute Sum of Squares	2.901
Sy.x	0.4916
Constraints	
A1	A1 > 0.0
K1	K1 > 0.0
Data	
Number of X values	14
Number of Y replicates	1

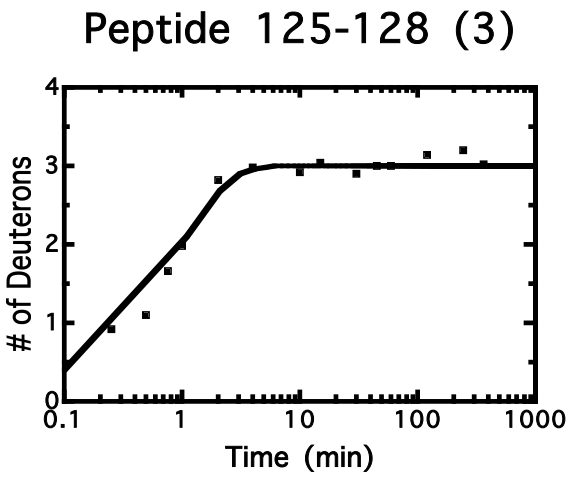

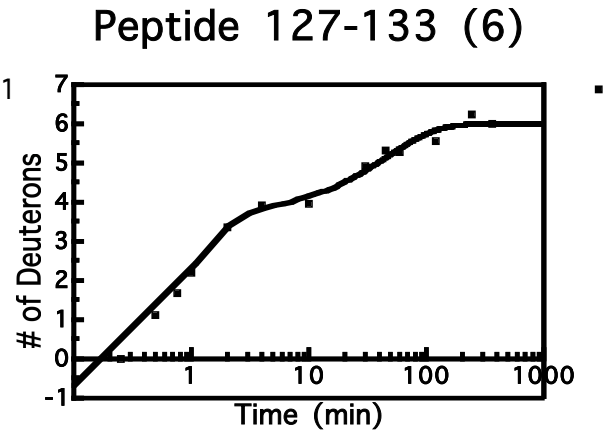

single exponential	
Best-fit values	
A1	2.893
K1	1.057
Std. Error	
A1	0.2018
K1	0.1214
95% Confidence Intervals	
A1	2.453 to 3.332
K1	0.7923 to 1.321
Goodness of Fit	
Degrees of Freedom	12
R squared	0.9789
Absolute Sum of Squares	0.1704
Sy.x	0.1192
Data	
Number of X values	14
Number of Y replicates	1
Total number of values	14
Number of missing values	0

	127-133 (6)
double exponential	
Best-fit values	
A1	4.948
K1	1.207
A2	2.313
K2	0.02180
Std. Error	
A1	0.3161
K1	0.1571
A2	0.1622
K2	0.003190
95% Confidence Intervals	
A1	4.233 to 5.663
K1	0.8513 to 1.562
A2	1.946 to 2.680
K2	0.01458 to 0.02901
Goodness of Fit	
Degrees of Freedom	9
R squared	0.9948
Absolute Sum of Squares	0.2514
Sy.x	0.1671
Constraints	
A1	A1 > 0.0

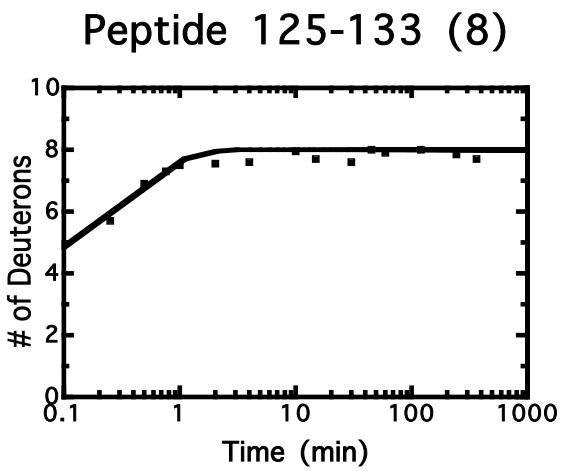

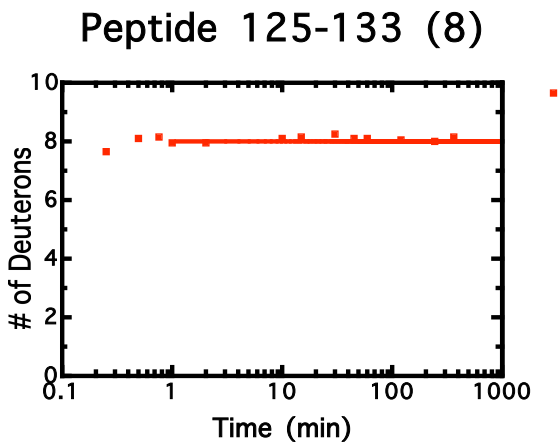

	125-133 (8)
single exponential	
Best-fit values	
A1	3.967
K1	2.283
Std. Error	
A1	0.7966
K1	0.5013
95% Confidence Intervals	
A1	2.231 to 5.702
K1	1.191 to 3.375
Goodness of Fit	
Degrees of Freedom	12
R squared	0.8471
Absolute Sum of Squares	0.7301
Sy.x	0.2467
Constraints	
A1	A1 > 0.0
K1	K1 > 0.0
Data	
Number of X values	14
Number of Y replicates	1

	125-133 (8)
single exponential	
Best-fit values	
A1	2.6550e+006
K1	63.46
Std. Error	
A1	7.4717e+012
K1	1.1278e+007
95% Confidence Intervals	
A1	0.0 to 1.6445e+013
K1	0.0 to 2.4823e+007
Goodness of Fit	
Degrees of Freedom	11
R squared	0.3291
Absolute Sum of Squares	0.1699
Sy.x	0.1243
Constraints	
A1	A1 > 0.0
K1	K1 > 0.0
Data	
Number of X values	14
Number of Y replicates	1

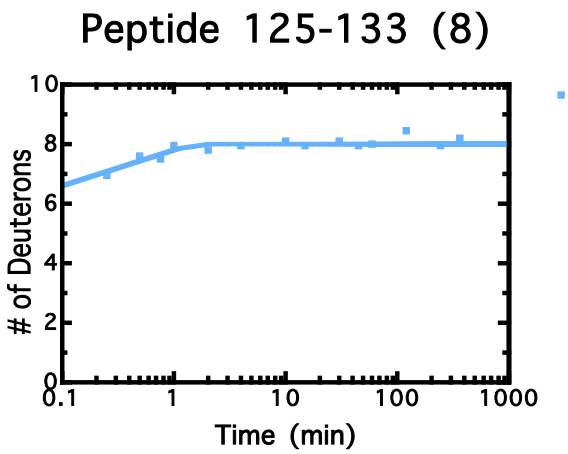

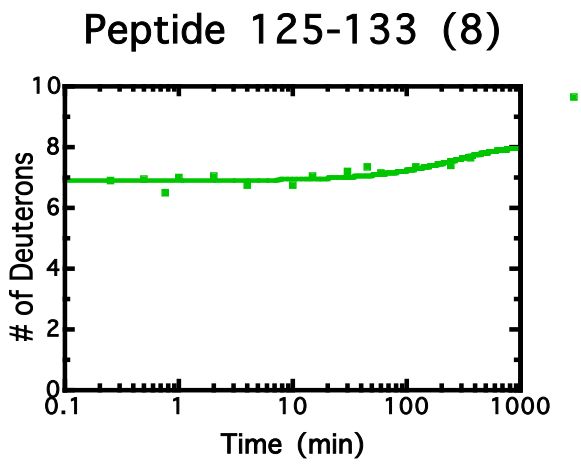

	125-133 (8)
single exponential	
Best-fit values	
A1	1.745
K1	2.226
Std. Error	
A1	0.5709
K1	0.8065
95% Confidence Intervals	
A1	0.5011 to 2.989
K1	0.4685 to 3.983
Goodness of Fit	
Degrees of Freedom	12
R squared	0.7637
Absolute Sum of Squares	0.3962
Sy.x	0.1817
Constraints	
A1	A1 > 0.0
K1	K1 > 0.0
Data	
Number of X values	14
Number of Y replicates	1

	125-133 (8)
single exponential	
Best-fit values	
A1	1.103
K1	0.003555
Std. Error	
A1	0.06354
K1	0.001059
95% Confidence Intervals	
A1	0.9643 to 1.241
K1	0.001248 to 0.0058
Goodness of Fit	
Degrees of Freedom	12
R squared	0.6471
Absolute Sum of Squares	0.4197
Sy.x	0.1870
Constraints	
A1	A1 > 0.0
K1	K1 > 0.0
Data	
Number of X values	14
Number of Y replicates	1

Subtracted Peptide 31-40(9)

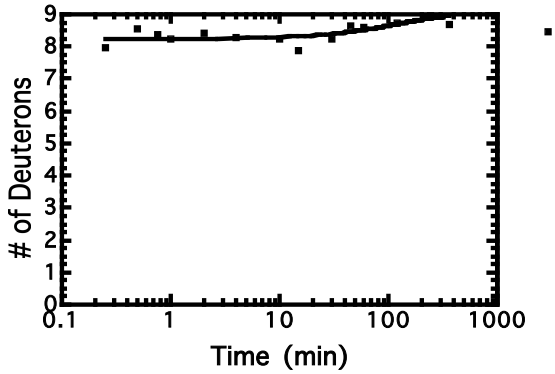

single exponential	
Best-fit values	
A1	0.7606
K1	0.007639
Std. Error	
A1	0.07822
K1	0.003581
95% Confidence Intervals	
A1	0.5902 to 0.9
K1	0.0 to 0.0154
Goodness of Fit	
Degrees of Freedom	12
R squared	0.5442
Absolute Sum of Squares	0.5380
Sy.x	0.2117
Constraints	
A1	A1 > 0.0
K1	K1 > 0.0
Data	
Number of X values	14
Number of Y replicates	1
Total number of values	14
Number of missing values	0

Subtracted Peptide 31-40(9)

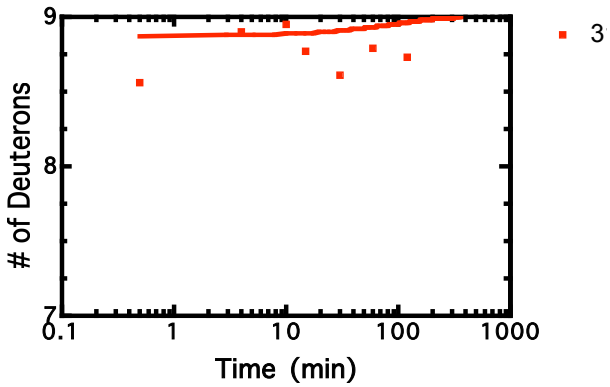

single exponential	
Best-fit values	
A1	0.1268
K1	0.01040
Std. Error	
A1	0.1282
K1	0.04307
95% Confidence Intervals	
A1	0.0 to 0.4089
K1	0.0 to 0.1052
Goodness of Fit	
Degrees of Freedom	11
R squared	0.08937
Absolute Sum of Squares	1.045
Sy.x	0.3082
Constraints	
A1	A1 > 0.0
K1	K1 > 0.0
Data	
Number of X values	14
Number of Y replicates	1
Total number of values	13
Number of missing values	1

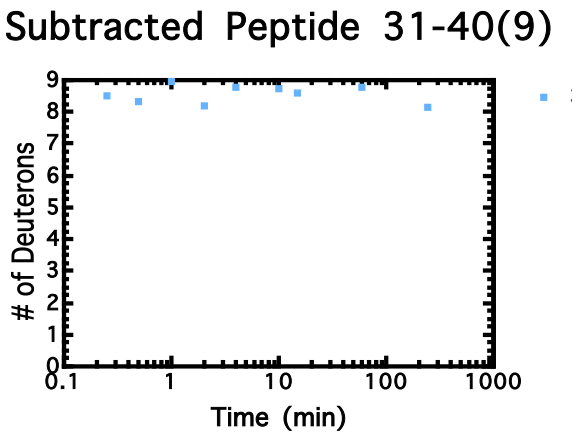

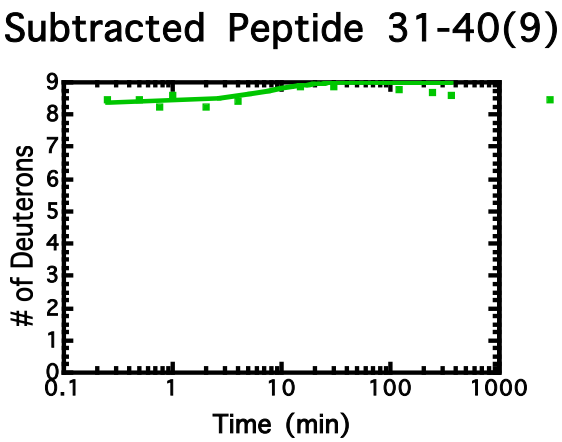

single exponential	
Best-fit values	
A1	0.6716
K1	0.1278
Std. Error	
A1	0.1615
K1	0.1052
95% Confidence Intervals	
A1	0.3198 to 1.0
K1	0.0 to 0.3571
Goodness of Fit	
Degrees of Freedom	12
R squared	0.5055
Absolute Sum of Squares	0.9446
Sy.x	0.2806
Constraints	
A1	A1 > 0.0
K1	K1 > 0.0
Data	
Number of X values	14
Number of Y replicates	1
Total number of values	14
Number of missing values	0

LISTERIA MONOCYTOGENES COMPARISON OF PERCENT FAST EXCHANGE WITH CRYSTALLOGRAPHIC DISTANCE FROM AMIDE N TO MN^{2+} CENTER

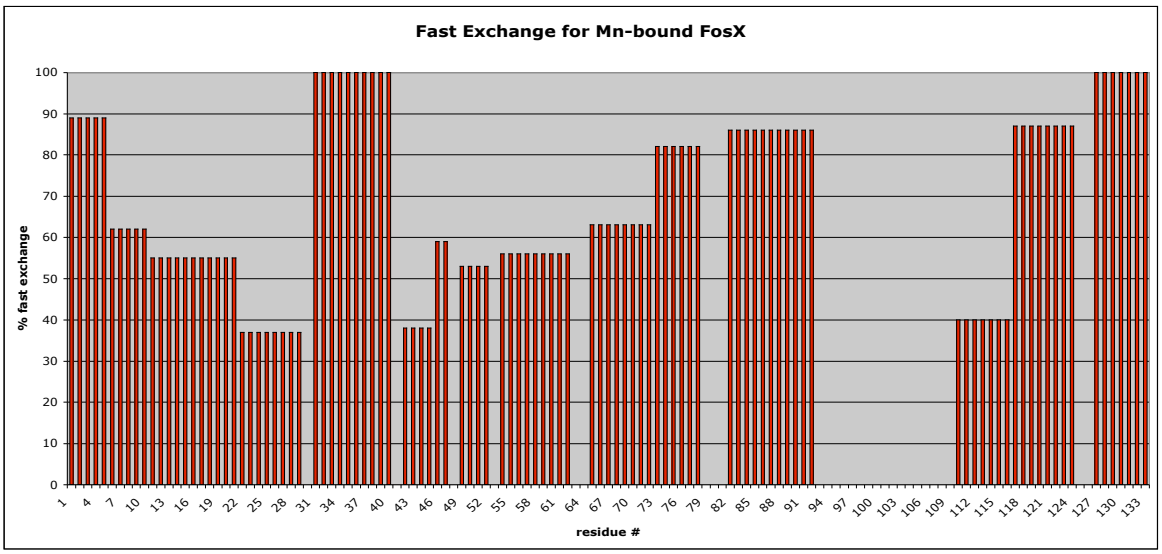

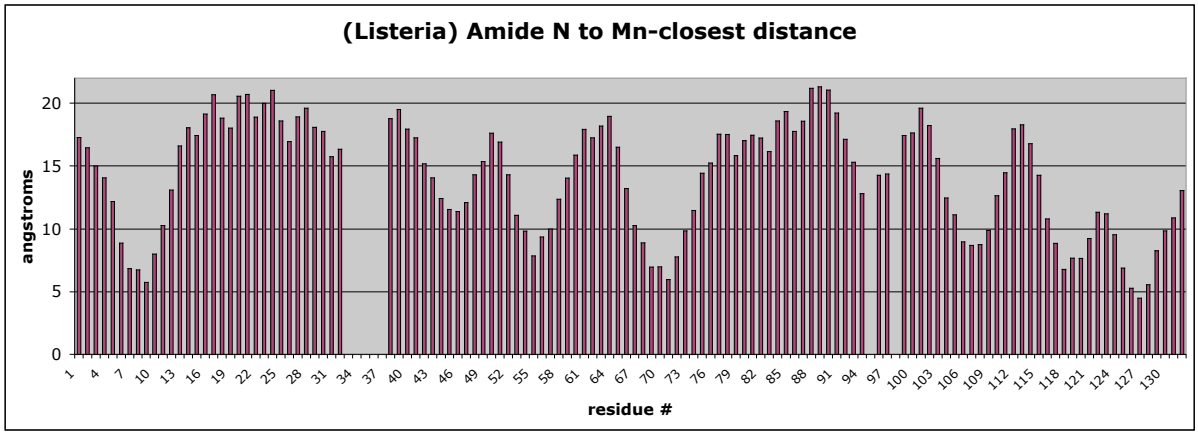

REFERENCES

1. Yoneyama, H.; Katsumata, R. (2006) Antibiotic resistance in bacteria and its future for novel antibiotic development. *Biosci. Biotechnol. Biochem.*, 70, 1060-1075.

2. Alanis, A.J. (2005) Resistance to antibiotics: are we in the post-antibiotic era? *Arch. Med. Res.*, 36, 697-705.

3. Hendlin, D., Stapley, E.O., Jackson, M., Wallick, H., Miller, A.K., Wolf, F.J., Miller, T.W., Chaiet, L., Kahan, F.M., Flotz, E.L., Woodruff, J.H., Mata, J.M., Hernandez, S., Mochales, S. (1969) Phosphonomycin, a new antibiotic produced by strains of *Streptomyces*. *Science,* 166, 122-123.

4. Christensen, B.G., Leanza, W.J., Beattie, T.R., Patchett, A.A., Arison, B.H., Ormond, R.E., Kuehl, F.A., Albers-Schonberg, G., Jardetzky, O. (1969) Phosphonomycin: structure and synthesis. *Science,* 166, 123-125.

5. Kahan, F.M., Kahan, J.S., Cassidy, P.J., Kroop, H. (1974) The mechanism of action of fosfomycin (phosphonomycin). *Ann. N.Y. Acad. Sci.,* 235, 364-385.

6. Marquardt, J.L., Brown, E.D., Lane, W.S., Haley, T.M., Ichskawa, Y., Wong, C-H., Walsh, C.T. (1994) Kinetics, stoichiometry, and identification of the reactive thiolate in the inactivation of UDP-GIc*N*Ac enolpyruvyl transferase by the antibiotic fosfomycin. *Biochemistry,* 33, 10646-10651.

7. Skarzynski, T., Mistry, A., Wonacott, A., Hutchinson, S.E., Kelly, V.A., Duncan, K. (1996) Structure of UDP-*N*-acetylglucosamine enolpyruvyl transferase, an enzyme essential for the synthesis of bacterial peptidoglycan, complexed with substrate UDP-*N*-acetylglucosamine and the drug fosfomycin. *Structure,* 4, 1465-1474.

8. Patel, S.S., Balfour, J.A., Bryson, H.M. (1997) Fosfomycin tromethamin. A review of its antibacterial activity, pharmacokinetic properties and therapeutic efficacy as a single-dose oral treatment for acute uncomplicated lower urinary tract infections. *Drugs,* 53, 637-656.

9. Krcmery, S., Hromec, J., Demesova, D. (2001) Treatment of lower urinary tract infection in pregnancy. *Int. J. Antimicrob. Agents,* 17, 279-282.

10. Allerberger, F., Klare, I. (1999) In-vitro activity of fosfomycin against vancomycin-resistant enterococci. *J. Antimicrob. Chemother.,* 43, 211-217.

11. Ungheri, C., Albini, E., Belluco, G. (2002) In-vitro susceptibility of quinolone-resistant clinical isolates of *Escherichia coli* to fosfomycin trometamol. *J. Chemother.*, 14, 237-240.

12. Kadner, R.J., Winkler, H.H. (1973) Isolation and characterization of mutations affecting the transport of hexose phosphates in *Escherichia coli*. *J. Bacteriol.*, 113, 895-900.

13. Tsuruoka, T., Yamada, Y. (1975) Characterization of spontaneous fosfomycin (phosphonomycin)-resistant cells of *Escherichia coli* B in vitro. *J. Antibiot.,* 28, 906-911.

14. Mendoza, M.C., Garcia, J.M., Llaneza, J., Mendez, F.J., Hardisson, C., Ortiz, J.M. (1980) Plasmid-determined resistance to fosfomycin in *Serratia marcescens*. *Antimicrob. Agents Chemother.,* 18, 215-219.

15. Llaneza, J., Villar, C.J., Salas, J.A., Suarez, J.E., Mendoza, M.C., Hardisson, C. (1985) Plasmid-mediated fosfomycin resistance is due to enzymatic modification of the antibiotic. *Antimicrob. Agents Chemother.,* 28, 163-164.

16. Arca, P., Rico, M., Brana, A.F., Villar, C.J., Hardisson, C., Suarez, J.E. (1988) Formation of an adduct between fosfomycin and glutathione: a new mechanism of antibiotic resistance in bacteria. *Antimicrob. Agents Chemother.,* 32, 1552-1556.

17. Arca, P., Hardisson, C., Suarez, J.E. (1990) Purification of a glutathione S-transferase that mediates fosfomycin resistance in bacteria. *Antimicrob. Agents Chemother.,* 34, 844-848.

18. Armstrong, R.N. (2000) Mechanistic diversity in a metalloenzyme superfamily. *Biochemistry*, 39, 13625-13632.

19. Bergdoll, M., Eltis,, L.D., Cameron, A.D., Dumas, P., Bolin, J.T. (1988) All in the family: structural and evolutionary relationships among three modular proteins with divese functions and variable assembly. *Protein Sci.,* 7, 1661-1670.

20. Rife, C.L., Pharris, R.E., Newcomer, M.E., Armstrong, R.N. (2002) Crystal structure of a genomically encoded fosfomycin resistance protein (FosA) at 1.19 Å resolution by MAD phasing off the L-III edge of Tl^+. *J. Am. Chem. Soc.,* 124, 11001-11003.

21. Bernat, B.A., Laughlin, L.T., Armstrong, R.N. (1997) Fosfomycin resistance protein (FosA) is a manganese metalloglutathione transferase related to glyoxalase I and the extradiol dioxygenases. *Biochemistry*, 36, 3050-3055.

22. Bernat, B.A., Laughlin, L.T., Armstrong, R.N. (1999) Elucidation of a monovalent cation dependence and characterization of the divalent cation binding site of the fosfomycin resistance protein, FosA. *Biochemistry,* 38, 7462-7469.

23. Cao, M., Bernat, B.A., Wang, Z., Armstrong, R.N., Helmann, J.D. (2001) FosB, a cysteine-dependent fosfomycin resistance protein under the control of _W, an extracytoplasmic function _ factor in *Bacillus subtilis. J. Bacteriol.,* 183, 2380-2383.

24. Fillgrove, K.L., Pakhomova, S., Newcomer, M.E., Armstrong, R.N. (2003) Mechanistic diversity of fosfomycin resistance in pathogenic microorganisms. *J. Am. Chem. Soc.,* 125, 15730-15731.

25. U.S. Food and Drug Administration: Center for Food Safety & Applied Nutrition. (2006, Jun. 14-last update). Bad Bug Book: *Listeria monocytogenes.* Retrieved Sept. 11, 2006 from http://www.cfsan.fda.gov/~mow/chap6.html.

26. Microbiology @ Leicester. (2002-last update). *Pseudomonas putida.* Retrieved Sept. 11, 2006 from http://www-micro.msb.le.ac.uk/video/Pputida.html.

27. Partridge, S.R., Hall, R.M. (2005) Gene cassettes potentially encoding fosfomycin resistance determinants. *Antimicrob. Agents Chemother.,* 49, 860-861.

28. Lee, K., Lim, J.B., Yum, J.H., Yong, D., Chong, Y., Kim, J.M., Livermore, D.M. (2002) *bla*$_{VIM-2}$ cassette-containing novel integrons in metallo-β-lactamase-producing *Pseudomonas aeruginosa* and *Pseudomonas putida* isolates disseminated in a Korean hospital. *Antimicrob. Agents Chemother.,* 46, 1053-1058.

29. Engen, J.R. (2006, Aug. 6 – last update). HXMS.com. Retrieved Sept. 11, 2006 from www.hxms.com/hxms.htm.

30. Hoofnagle, A.N., Resing, K.A., Ahn, N.G. (2003) Protein analysis by hydrogen exchange mass spectrometry. *Annu. Rev. Biophys. Biomol. Struct.,* 32, 1-25.

31. Busenlehner, L.S., Armstrong, R.N. (2005) Insights into enzyme structure and dynamics elucidated by amide H/D exchange mass spectrometry. *Arch. Biochem. Biophys.,* 433, 34-46.

32. Rigsby, R.E., Fillgrove, K.L., Beihoffer, L.A., Armstrong, R.N. (2005) Fosfomycin resistance proteins: a nexus of glutathione transferases and epoxide hydrolases in a metalloenzyme superfamily. *Meth. Enz.,* 401, 367-379.

33. Busenlehner, L.S., Codreanu, S.G., Holm, P.J., Bhakat, P., Hebert, H., Morgenstern, R., Armstrong, R.N. (2004) Stress sensor triggers conformational response of the integral membrane protein microsomal glutathione transferase 1. *Biochemistry,* 43, 11145-11152.

34. Codreanu, S.G., Thompson, L.C., Hachey, D.L., Dirr, H.W., Armstrong, R.N. (2005) Influence of the dimer interface on glutathione transferase structure and dynamics revealed by amide H/D exchange mass spectrometry. *Biochemistry,* 44, 10605-10612.

35. Wilkins, M. R., Lindskog, I., Gasteiger, E., Bairoch, A., Sanchez, J. C., Hochstrasser, D. F., Appel, R. D. (1997) Detailed peptide characterization using PEPTIDEMASS- -a World-Wide-Web-accessible tool. *Electrophoresis,* 18, 403-408.

36. Clauser K. R., Baker, P. R., Burlingame, A. L. (1999) Role of accurate mass measurement (±10 ppm) in protein identification strategies employing MS or MS/MS and database searching. *Anal. Chem.,* 71, 2871-2882.

37. Cravello, L., Lascoux, D., Forest, E. (2003) Use of different proteases working in acidic conditions to improve sequence coverage and resolution in hydrogen/deuterium exchange of large proteins. *Rapid Commun. Mass Spectrom*., 17, 2387-2393.

38. Zhang, Z., Marshall, A. G. (1998) A universal algorithm for fast and automated charge state deconvolution of electrospray mass-to-charge ratio spectra. *J. Am. Soc. Mass. Spectrom.,* 9, 225-233.

39. Guo, J., Giedroc, D.P. (1997) Zinc site redesign in T4 Gene 32 Protein: Structure and stability of cobalt(II) complexes formed by wild-type and metal ligand substitution mutants. *Biochemistry,* 36, 730-742.

40. VanZile, M.L., Cosper, N.J., Scott, R.A., Giedroc, D.P. (2000) The zinc metalloregulatory protein *Synechococcus* PCC7942 SmtB binds a single zinc ion per monomer with high affinity in a tetrahedral coordination geometry. *Biochemistry,* 39, 11818-11829.

41. Wang, F., Li, W., Emmett, M.R., Marshall, A.G. (1999) Fourier transform ion cyclotron resonance mass spectrometric detection of small Ca^{2+}-induced conformational changes in the regulatory domain of human cardiac Troponin C. *Am. Soc. Mass Spectrom.,* 10, 703-710.

42. Villanueva, J., Hoshino, M., Katou, H., Kardos, J., Hasegawa, K., Naiki, H., Goto, Y. (2004) Increase in the conformational flexibility of β_2-microglobulin upon copper binding: a possible role for copper in dialysis-related amyloidosis. *Prot. Sci.,* 13, 797-809.

43. Dill, K.A., Chan, H.S. (1997) From Levinthal pathways to funnels. *Nat. Struct. Biol.,* 4, 10-19.

44. Zidek, L., Novotny, M.V., Stone, M.J. (1999) Increased protein backbone conformational entropy upon hydrophobic ligand binding. *Nat. Struct. Biol.,* 6, 1118-1121.

45. Yang, H., Smith, D.L. (1997) Kinetics of Cytochrome *c* folding examined by hydrogen exchange and mass spectrometry. *Biochemistry,* 36, 14992-14999.

46. Kulakova, A.N., Kulakov, L.A., Akulenko, N.V., Ksenzenko, V.N., Hamilton, J.T.G., Quinn, J.P. (2001) Structural and functional analysis of the phosphonoacetate hydrolase (*phnA*) gene region in *Pseudomonas fluorescens* 23F. *J. Bacteriol.,* 183, 3268-3275.

47. Cook, A.M., Daughton, C.G., Alexander, M. (1978) Phosphate utilization by bacteria. *J. Bacteriol.,* 133, 85-90.

48. McGrath, J.W., Ternan, N.G., Quinn, J.P. (1997) Utilization of organophosphonates by environmental microorganisms. *Lett. Appl. Microbiol.,* 24, 69-73.

49. Rigsby, R.E., Rife, C.L., Fillgrove, K.L., Newcomer, M.E., Armstrong, R.N. (2004) Phosphonoformate: A minimal transition state analogue inhibitor of the fosfomycin resistance protein, FosA. *Biochemistry,* 43, 13666-13673.